

**A FAULT DETECTION AND DIAGNOSIS STRATEGY FOR
PERMANENT MAGNET BRUSHLESS DC MOTOR**

**A FAULT DETECTION AND DIAGNOSIS STRATEGY FOR
PERMANENT MAGNET BRUSHLESS DC MOTOR**

By

Wanlin Zhang, B.Eng

A Thesis Submitted to the School of Graduate Studies in
Partial Fulfilment of the Requirements for the
Degree of Master of Applied Science

McMaster University

© Copyright by Wanlin Zhang, November 2012. All rights reserved.

Master of Applied Science (2012)

McMaster University

Mechanical Engineering

Hamilton, Ontario, Canada

TITLE: A FAULT DETECTION AND DIAGNOSIS
STRATEGY FOR PERMANENT MAGNET
BRUSHLESS DC MOTOR

AUTHOR: Wanlin Zhang, B.Eng in Mechanical Engineering
(University of Science and Technology Beijing)

SUPERVISOR: Dr. Saeid Habibi

NUMBER OF PAGES xv, 166

To My Parents
For Their Unconditional Love, Support and Patience

Abstract

Unexpected failures in rotating machinery can result in production downtime, costly repairs and safety concerns. Electric motors are commonly used in rotating machinery and are critical to their operation. Therefore, fault detection and diagnosis of electric motors can play a very important role in increasing their reliability and operational safety. This is especially true for safety critical applications.

This research aims to develop a Fault Detection and Diagnosis (FDD) strategy for detecting motor faults at their inception. Two FDD strategies were considered involving wavelets and state estimation. Bearing faults and stator winding faults, which are responsible for the majority of motor failures, are considered. These faults were physically simulated on a Permanent Magnet Brushless DC Motor (PMBLDC). Experimental results demonstrated that the proposed fault detection and diagnosis schemes were very effective in detecting bearing and winding faults in electric motors.

Acknowledgement

I would like to express my gratitude to my supervisor, Dr. Saeid R. Habibi, for his guidance, advice, and support during the course of this research and the writing of this dissertation. Special thanks are also due to my colleagues Dr. Andrew Gadsden, Yu Song and Reza Haqshenas for their kind assistance, technical expertise, and support during this research.

Most important of all, I would also like to express my deepest gratitude and appreciation to my parents, for their unconditional love, unflinching sacrifice and endless encouragement.

Table of Contents

Abstract	ii
Acknowledgement	iv
Table of Contents	v
List of Figures	vii
List of Tables	xi
List of Nomenclature.....	xii
Chapter 1 Introduction	1
1.1 Overview	1
1.2 Permanent Magnet Brushless DC Motor	2
1.3 Bearing Fundamentals	4
1.4 Objectives of Research	11
1.5 Outline of Thesis.....	12
Chapter 2 Literature Review.....	14
2.1 Overview	14
2.2 Mechanical Faults.....	15
2.3 Electrical Faults	24
2.4 Summary	29
Chapter 3 Bearing Fault Diagnosis Using Wavelet Transforms.....	31
3.1 Kurtosis	32
3.2 Envelope Analysis	33
3.3 Dual-Tree Complex Wavelet Transform (DTCWT)	40
3.4 Application of Wavelet Transform in Signal Denoising	44
3.4.1 Shrinkage-based Wavelet Denoising	44
3.4.2 Bivariate Shrinkage	46
3.5 The Proposed Denoising Scheme	49
3.6 Summary	52
Chapter 4 Experimental Results of Bearing Fault Diagnosis	54
4.1 Outer Race Fault	55

4.2	Inner Race Fault	68
4.3	Multiple Faults	78
4.4	Summary	89
Chapter 5	Estimation Theory	90
5.1	The Kalman Filter	90
5.2	The Extended Kalman Filter (EKF)	94
5.3	The Smooth Variable Structure Filter (SVSF)	96
5.4	The EK-SVSF	101
5.5	Summary	106
Chapter 6	Experimental Results of Stator Winding Fault Diagnosis	107
6.1	Normal Condition	115
6.2	Winding Resistance Fault	117
6.3	Modeling Uncertainty	119
6.4	Winding Resistance Fault and Modeling Uncertainty	123
6.5	Summary	126
Chapter 7	Concluding Remarks	128
7.1	Summary of Research	128
7.2	Recommendations and Future Work	130
Appendix	131
1.	Experimental Setup	131
2.	The Kalman Filter without Artificial Measurements	138
3.	Matlab Code	141
Bibliography	154

List of Figures

Figure 1	Simplified equivalent circuit of the BLDC motor [3].....	3
Figure 2	A single-row deep-groove radial ball bearing [8].....	6
Figure 3	Fretting [10]	8
Figure 4	Wear [10].....	8
Figure 5	Flaking [10].....	9
Figure 6	Pitting [10]	9
Figure 7	Brinelling [10].....	10
Figure 8	Smearing [10]	10
Figure 9	Rust [10]	10
Figure 10	Corrosion [10]	10
Figure 11	The proposed fault detection and diagnosis scheme for BLDC motor	11
Figure 12	Fault diagnosis scheme	31
Figure 13	Typical vibration signal measured from a normal bearing	32
Figure 14	Typical vibration signal measured from a faulty bearing	33
Figure 15	A simulated signal with amplitude modulation phenomenon	34
Figure 16	Frequency spectrum of the simulated signal	35
Figure 17	Diagram of signal processing steps in envelope analysis.....	36
Figure 18	Bode plot of the digital IIR filter.....	36
Figure 19	A simulated signal with modulating frequency at 200 Hz and carrier frequency at 2000 Hz	38
Figure 20	Frequency spectrum of simulated signal without any processing.....	39
Figure 21	Frequency spectrum of simulated signal after amplitude demodulation	39
Figure 22	Scaling function and wavelet function of the 14-tap Q-shift filters	42
Figure 23	The dual-tree filter banks for decomposition and reconstruction [44].	43
Figure 24	The Wavelet Shrinkage Procedures	45
Figure 25	Hard and Soft Thresholding (x – input coefficient, y – thresholded coefficient)	46
Figure 26	The proposed signal denoising scheme	49
Figure 27	(a) Simulated vibration signal from a faulty bearing; (b) Denoised signal using DTCWT; (c) Denoised signal using digital IIR filter	52
Figure 28	The proposed signal denoising scheme (same as Figure 26)	55
Figure 29	Inventor model of the test bearing with an outer race defect	55
Figure 30	Raw vibration signal from the faulty bearing at 1200 RPM	56
Figure 31	Partial enlarged signal from the faulty bearing at 1200 RPM.....	57
Figure 32	DTCWT-denoised signal from the faulty bearing at 1200 RPM	58
Figure 33	DTCWT-denoised signal from the normal bearing at 1200 RPM.....	58

Figure 34	Frequency spectrum of raw signal from the faulty bearing at 1200 RPM	59
Figure 35	Frequency spectrum of denoised signal from the faulty bearing at 1200 RPM.....	59
Figure 36	Frequency spectrum of denoised signal from the normal bearing at 1200 RPM.....	60
Figure 37	Scalogram of denoised signal from the faulty bearing at 1200 RPM	61
Figure 38	Partial enlarged vibration signal from the faulty bearing at 2100 RPM	62
Figure 39	DTCWT-denoised signal from the faulty bearing at 2100 RPM.....	63
Figure 40	Frequency spectrum of denoised signal from the faulty bearing at 2100 RPM.....	63
Figure 41	Scalogram of denoised signal from the faulty bearing at 2100 RPM	65
Figure 42	Measured motor speed in the Extra Urban Driving Cycle test	66
Figure 43	Ball Passing Frequency Outer Race (BPFO) in EUDC test.....	67
Figure 44	Scalogram of denoised signal from the faulty bearing in EUDC test	67
Figure 45	Inventor model of the test bearing with an inner race defect	68
Figure 46	Raw vibration signal from the faulty bearing at 1000 RPM	69
Figure 47	Frequency spectrum of raw signal from the faulty bearing at 1000 RPM	70
Figure 48	Frequency spectrum of denoised signal from the faulty bearing at 1000 RPM.....	70
Figure 49	Frequency spectrum of raw signal from the normal bearing at 1000 RPM	71
Figure 50	Scalogram of denoised signal from the faulty bearing at 1000 RPM	72
Figure 51	Partial enlarged signal from the faulty bearing at 2800 RPM.....	73
Figure 52	DTCWT-denoised signal from the faulty bearing at 1200 RPM.....	74
Figure 53	Frequency spectrum of denoised signal from the faulty bearing at 2800 RPM.....	74
Figure 54	Scalogram of denoised signal from the faulty bearing at 2800 RPM	75
Figure 55	Measured motor speed in the Extra Urban Driving Cycle test (same as Figure 40)	76
Figure 56	Ball Passing Frequency Inner Race (BPFI) in EUDC test	77
Figure 57	Scalogram of denoised signal from the faulty bearing in EUDC test	77
Figure 58	Inventor model of the test bearing with multiple defects: (a) Outer race defect; (b) Inner race defect.....	78
Figure 59	Raw vibration signal from the bearing with multiple faults at 1500 RPM	79
Figure 60	Partial enlarged signal from the bearing with multiple faults at 1500 RPM	80
Figure 61	DTCWT-denoised signal from the bearing with multiple faults at 1500 RPM	80
Figure 62	Frequency spectrum of raw signal from the bearing with multiple faults at 1500 RPM.....	81

Figure 63	Frequency spectrum of denoised signal from the bearing with multiple faults at 1500 RPM	82
Figure 64	Scalogram of denoised signal from the bearing with multiple faults at 1500 RPM.....	82
Figure 65	Partial enlarged vibration signal from the bearing with multiple faults at 2500 RPM.....	84
Figure 66	DTCWT-denoised signal from the bearing with multiple faults at 2500 RPM.....	84
Figure 67	Frequency spectrum of denoised signal from the bearing with multiple faults at 2500 RPM	85
Figure 68	Scalogram of denoised signal from the bearing with multiple faults at 2500 RPM.....	85
Figure 69	Measured motor speed in the Extra Urban Driving Cycle test (same as Figure 40)	87
Figure 70	Ball Passing Frequencies (BPFO and BPFI) in EUDC test	87
Figure 71	Scalogram of denoised signal from the faulty bearing in EUDC test	88
Figure 72	The discrete Kalman Filter cycle.....	91
Figure 73	SVSF state estimation concept.....	97
Figure 74	The concept of EK-SVSF strategy [117].....	102
Figure 75	Methodology of combining nonlinear filtering strategies [117].	103
Figure 76	Typical voltage measurements	108
Figure 77	Typical current measurements	108
Figure 78	Simplified equivalent circuit of the BLDC motor (same as Figure 1) [3].	109
Figure 79	Artificial measurements of phase resistance	111
Figure 80	Estimation of phase resistance using EK-SVSF	115
Figure 81	Estimation of phase resistance using Extended Kalman Filter (EKF)	116
Figure 82	Estimation of phase resistance using Extended Kalman Filter (EKF)	117
Figure 83	Estimation of phase resistance using EK-SVSF	118
Figure 84	Estimation of phase resistance using Extended Kalman Filter (EKF)	120
Figure 85	Estimation of phase resistance using EK-SVSF	121
Figure 86	The VBL trajectory of the three-phase currents in EK-SVSF	122
Figure 87	Estimation of phase resistance using Extended Kalman Filter (EKF)	124
Figure 88	Estimation of phase resistance using EK-SVSF	124
Figure 89	The VBL trajectory of the three-phase currents in EK-SVSF	125
Figure 90	The Permanent Magnet Brushless DC Motor	131
Figure 91	Architecture of fault diagnosis scheme	132
Figure 92	(a) Inventor model of the test motor; (b) Inventor model of the test bearing.....	132
Figure 93	Dimensions of a ball bearing	133

Figure 94	Mounting technique [127]	134
Figure 95	Simplified stator circuit model with faulty resistance in one phase .	137
Figure 96	Estimation of phase resistance using Extended Kalman Filter (EKF)	138
Figure 97	Estimation of phase resistance using Extended Kalman Filter (EKF)	139

List of Tables

Table 1	Parameters of the designed Butterworth digital IIR filter	37
Table 2	Design parameters of the digital IIR filter	51
Table 3	DTCWT parameters.....	51
Table 4	Kurtosis of signals from faulty and normal bearings at 1200 RPM.....	61
Table 5	Kurtosis of signals from faulty and normal bearings at 2100 RPM.....	64
Table 6	Kurtosis of signals from faulty and normal bearings at 1000 RPM.....	72
Table 7	Kurtosis of signals from faulty and normal bearings at 2800 RPM.....	75
Table 8	Kurtosis of signals from faulty and normal bearings at 1500 RPM.....	83
Table 9	Kurtosis of signals from faulty and normal bearings at 2500 RPM.....	86
Table 10	Summary of EKF equations [116]	96
Table 11	Summary of SVSF estimation steps	100
Table 12	Summary of EK-SVSF (Predictor)	104
Table 13	Summary of EK-SVSF (Corrector).....	105
Table 14	Faulty conditions of the motor in the sencond case of experimental tests	113
Table 15	Modeling uncertainties in the third case of experimental tests.....	114
Table 16	Fault conditions and modeling uncertainties in the fourth case of experimental tests	114
Table 17	Root Mean Square Error of estimated parameters (Normal Case) ..	116
Table 18	Root Mean Square Error of estimated parameters (Winding Resistance Fault).....	119
Table 19	Root Mean Square Error of estimated parameters (Modeling Uncertainty)	122
Table 20	Root Mean Square Error of estimated parameters	126
Table 21	Motor construction parameters	131
Table 22	Bearing Parameters.....	133
Table 23	Accelerometer specification.....	134
Table 24	Specifications of data acquisition card.....	136
Table 25	Root Mean Square Error of estimated parameters (Winding Resistance Fault).....	139
Table 26	Root Mean Square Error of estimated parameters (Modeling Uncertainties)	140

List of Nomenclature

A	Linear system matrix
B	Input gain matrix
C	Linear measurement matrix
d	Inner diameter of the bearing
$d_l^{\Re}(k)$	Wavelet coefficients of the real tree in DTCWT
$c_j^{\Re}(k)$	Scaling coefficients of the real tree in DTCWT
$d_l^{\Im}(k)$	Wavelet coefficients of the imaginary tree in DTCWT
$c_j^{\Im}(k)$	Scaling coefficients of the imaginary tree in DTCWT
$d_l^C(k)$	Complex-valued wavelet coefficients
$c_j^C(k)$	Complex-valued scaling coefficients
D	Outer diameter of the bearing
e_k	State error vector (unless otherwise stated)
$e_{z,k}$	Measurement (or innovation) error vector
E_s	Back-EMF induced in the stator winding
F	Linearized system function
r_{MN}	Artificial measurement
h	Nonlinear measurement function
$h(m)$	A filter for the real tree of DTCWT
$\tilde{h}(m)$	An inversed version of the filter $h(m)$
$g(n)$	A filter for the imaginary tree of DTCWT
$\tilde{g}(n)$	An inversed version of the filter $g(m)$
H	Linearized measurement function
i	Index value
I_a, I_b, I_c, I_s	Phase current of the stator winding

I	Identity matrix
J	Maximum scale of a wavelet transform
k	Step value (for recursive process)
K	Gain value (used by filter)
K_e	Back-EMF constant
K_T	Torque constant
K_{vis}	Viscous friction coefficient
l	Scale of the wavelet transform
L_s	Phase inductance of the stator winding of the motor
m	Number of measurements
n	Number of states
N	Number of samples
N_b	Number of rolling balls in a bearing
P	State error covariance matrix or number of pole pairs
Q	System noise covariance matrix
R	Measurement noise covariance matrix
R_a, R_b, R_c, R_s	Phase resistance of the stator winding of the motor
S	Innovation covariance matrix
T_L	Load torque
u	Input to the system (scalar or vector)
u_a, u_b, u_c, u_s	Phase voltage of the stator winding
v	Measurement noise (scalar or vector)
V_t	Terminal voltage of the simplified winding circuit
ω	System noise (scalar or vector)
ω_r	Angular velocity of the motor
x	States or parameters (scalar or vector)
y	Artificial measurement (scalar or vector)

$y_{i,j}$	A wavelet coefficient at position i and scale j
z	Measurements (scalar or vector)
\bar{A} or $diag(A)$	Creation of a vector with diagonal elements of some matrix A
A^+	Pseudoinverse of some matrix A
A^T	Transpose of some matrix A
A^{-1}	Transpose of some matrix A
$k + 1 k$	Subscript, a priori (before the fact) value
$k + 1 k + 1$	Subscript, a posteriori (after the fact) value
$N(\mu, \sigma^2)$	Normal distribution with mean μ and variance σ^2
$p(a)$	Probability of some value a
\Re^n	n-dimensional vector space over the field of the real numbers
$sign(a)$	Saturation of some value a (such that $-1 \leq a \leq 1$)
β	Existence subspace value (SVSF)
$\beta_{i,j}$	Bivariate shrinkage factor
ε	Additive noise
γ	'Memory' or convergence rate (SVSF)
θ	Angle of load from radial plane
θ_e	Electrical angle of the motor
μ	Mean of the samples
σ	Variance of the samples
$\hat{\sigma}_{Y_{i,j}}^2$	Estimated variance of noisy wavelet coefficients
ψ	Smoothing boundary layer value (SVSF)
ψ_{lim}	Limits for the smoothing boundary layer width
$\hat{\cdot}$	Estimated value of some state or parameter
\sim	Error of some state or parameter
$\phi_h(t)$	Lowpass filter for the real part of a complex wavelet
$\phi_g(t)$	Lowpass filter for the imaginary part of a complex wavelet

$\psi_h(t)$	Highpass filter for the real part of a complex wavelet
$\psi_g(t)$	Highpass filter for the imaginary part of a complex wavelet
$\psi^c(t)$	Complex-valued wavelet function
$d_l^{\Re}(k)$	Wavelet coefficients of the real tree in DTCWT
$c_j^{\Re}(k)$	Scaling coefficients of the real tree in DTCWT
$d_l^{\Im}(k)$	Wavelet coefficients of the imaginary tree in DTCWT
$c_j^{\Im}(k)$	Scaling coefficients of the imaginary tree in DTCWT

Chapter 1 Introduction

1.1 Overview

Electric motors have become essential elements of modern production and manufacturing lines. In many applications, the motors are operated in unfavorable environments involving high temperature and overloading. These stresses together with the aging of parts may lead to motor faults. Once a failure occurs, it usually results in loss of productivity, downtime, and costly repairs. Condition monitoring leading to fault detection and diagnosis in electric motors is therefore of great value and has received much attention in the past few years.

Fault Detection and Diagnosis (FDD) is a process where the condition of equipment is monitored for signs of faults or deterioration, so that the maintenance or repair can be performed to prevent system failures. Instrumentation is an important consideration in FDD. Ideally, the scheme should minimize the requirement of additional sensors and use existing signals. Furthermore, it needs to avoid false positive, be reliable and provide a clear indication of incipient faults in a timely manner. In this study, two FDD approaches were developed and implemented on a permanent magnet synchronous motor. To demonstrate their effectiveness, the FDD methods were validated by physically simulating fault conditions on a Permanent Magnet Brushless DC Motor.

1.2 Permanent Magnet Brushless DC Motor

Permanent Magnet Brushless DC Motors (BLDC) are widely used in industrial applications. The BLDC motor usually consists of a stator with three-phase armature windings and a rotor with permanent magnets. In BLDC motors, commutation is achieved by using power electronics coupled to feedback of rotor position from hall sensors. Compared with conventional brushed DC motors, the BLDC does not have a mechanical commutator which suffers from surface wear and electric arcing. The rare earth magnets on the rotor of the BLDC motor produce a constant magnetic field which lead to high efficiency and high power factor [1]. Particularly, the high torque-weight ratio of BLDC motors makes it very suitable for applications such as electric vehicles. The BLDC motors have many benefits over DC motors and induction motors, such as [2]:

- better speed versus torque characteristics;
- high dynamic response;
- high efficiency;
- long operating life; and
- noiseless operation;

However, it also suffers a few disadvantages, such as:

- high cost due to rare-earth magnets;
- limited constant power range;
- demagnetization;
- limited high-speed capability; and
- risks of inverter failures

BLDC motors can be categorized as surface mounted or interior mounted, according to the position and orientation of rotor permanent magnets [3]. In the case of the stator windings, BLDCs can be categorized as trapezoidal or sinusoidal, based on the shapes of their back-Electromotive-Force (back-EMF) waveforms. In addition to the back-EMF, the phase current also has corresponding trapezoidal or sinusoidal variations. The one with sinusoidal back-EMF is also called Permanent Magnet Synchronous Motor (PMSM). For PMSM, the back-EMF generated in each phase winding by the rotation of the magnet is also sinusoidal.

In BLDCs, the magnetic fields generated in the stator and in the rotor are rotating synchronously. The stator of a BLDC motor consists of stacked steel laminations with windings kept in the slots that are axially cut along the inner periphery [2]. Most BLDCs have three stator star-connected windings [2].

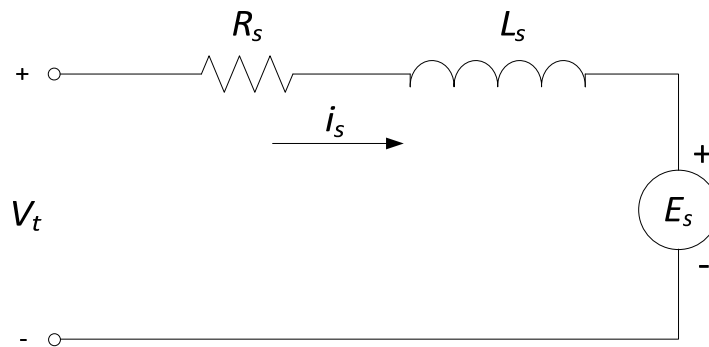


Figure 1 Simplified equivalent circuit of the BLDC motor [3].

In terms of modeling, a simplified equivalent circuit of one phase is given in Figure 1, where V_t is the voltage of the power supply, R_s is the resistance of

the winding, L_s is the leakage inductance ($L_s = L - M$, where L is the self-inductance of the winding and M is the mutual inductance), and E_s is the back-EMF induced in the winding by the rotating PM field.

Based on the equivalent circuit, the performance of the BLDC motor can be described by the following equations [3]:

$$V_t = R_s I_s + L_s \frac{dI_s}{dt} + E_s \quad \text{Equation 1.2.1}$$

$$E_s = K_e \omega_r \quad \text{Equation 1.2.2}$$

$$T_e = K_T I_s \quad \text{Equation 1.2.3}$$

$$T_e = T_L + J \frac{d\omega_r}{dt} + K_{vis} \omega_r \quad \text{Equation 1.2.4}$$

where K_e is the back-EMF constant, ω_r is the angular velocity of the rotor, K_T is the torque constant, T_L is the load torque, and K_{vis} is viscous friction coefficient.

1.3 Bearing Fundamentals

A. Generals

Rolling bearings of various kinds are widely used in industrial machines. They provide fundamental mechanical support for rotating parts. Most rotating shafts use a rolling element bearing. In order to ensure the effectiveness and

robustness of these bearings, their performance under various and extremely demanding conditions have been extensively studied [4, 5].

While there are various kinds of rolling bearings in the market, their associated fault detection approaches are analogous. Therefore, one of the most commonly used type of bearings, the single-row deep-groove radial ball bearing, is selected in this research. These bearings have one row of balls (referred to as a single row), that revolves around the ball path [6], as shown in Figure 2. These bearings consist of an inner ring, an outer ring, rolling elements (balls) and a cage (retainer). The inner ring has a groove on its outside diameter with a smooth finishing surface and extremely tight tolerances to form a path for the balls [7]. The inner ring is mounted on the shaft of the motor and rotates with the shaft at the same speed. The outer ring is the counterpart of the inner ring and has a groove on its inside diameter with high precision finish [7]. The outer ring is placed into the housing on motor case and thus held stationary with respect to the motor. The rolling balls locate between the inner ring and outer ring. These balls have slightly smaller diameters than the grooved ball track which allows them to contact the rings at a single point [7]. This point contact enables the bearing to rotate with minimal friction. In order to achieve point contact, the tolerances are strictly controlled to a micro inch level, as well as the dimensions of the balls and rings [7].

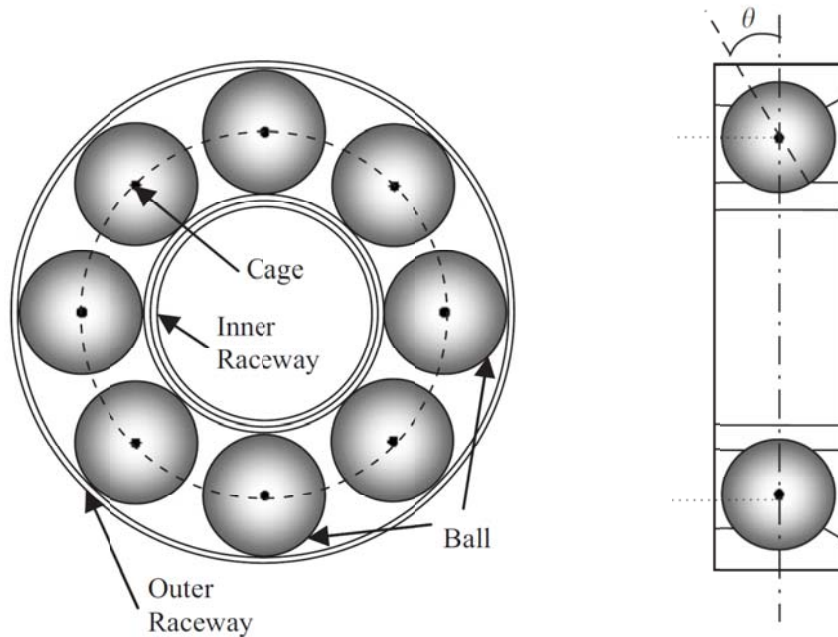


Figure 2 A single-row deep-groove radial ball bearing [8].

The cage on the other hand keeps an even and consistent spacing between the balls and prevents internal strikes [7]. It separates and guides the balls in the raceway during rotation and prevents the balls from falling out [7]. Finally, the lubricant (bearing grease) is also a fundamental component of a bearing, which can avoid or reduce metal-to-metal contact between the rolling balls and sliding contact surfaces, thus reduce friction and wear of those components [7].

Under normal running conditions, critical surface of a bearing refers to those which were designed to support and carry a load and reduce friction [6]. The critical surfaces include the surfaces of the balls, the cage, and the raceway (on the inner and outer rings). When a bearing is supporting a radial load, the

load is distributed on about one third of the whole area, which is called bearing load zone [6]. Accordingly, the performance of a bearing is closely related to the critical surfaces, particularly those entering the load zone at a given time.

B. Bearing Faults Categorization

Many factors can influence the life of the bearing, including loading, temperature, and lubrication. The typical fatigue life of a bearing can be significantly shortened by manufacturing defects, faulty mountings, improper lubrication, contamination, improper handling, improper maintenance, and by applying loads or speeds that exceed their maximum carrying capacity. These conditions can result in localized and distributed defects of the bearing components, thus very quickly cause permanent damage and even premature bearing failure. As a result of these factors, an estimated 95% of all bearing failures are classified as premature bearing failures [6].

The reason for bearing failure is often due to a combination of causes instead of just a single cause. Bearing defects may be categorized as localized or distributed. The localized defects include cracks, pits and spalls, while the distributed defects include surface roughness, waviness, misaligned races and off-size rolling elements [9]. Typical bearing faults and their causes are briefly summarized as follows.

- wear and fretting



Figure 3 Fretting [10]



Figure 4 Wear [10]

Wear is caused mainly by sliding abrasion on parts including the balls and raceways. Major causes include improper lubrication, contamination by foreign matter and corrosion. It occurs not only to the sliding surface but also to the rolling surface. Fretting is a phenomena which occurs when slight sliding is repeatedly caused on the contact surface by vibration load [4]. In the early stages, wear is usually a localized fault but can quickly spread throughout other components.

- flaking and pitting

Flaking is the phenomenon in which the bearing surface turns scaly and peels off due to contact load repeatedly received on the raceway and rolling surface [4]. Pitting refers to the small holes that occur on the raceway surface caused by rolling fatigue.



Figure 5 Flaking [10]

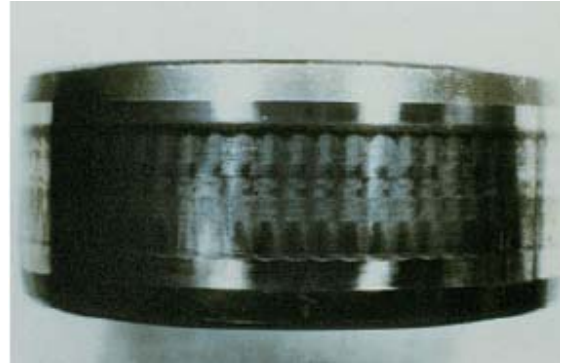


Figure 6 Pitting [10]

Electric pitting happens when the bearing surface is partially melted by electric current passing through the bearing at the contact point [4]. Significant electric pitting causes flaking. Flaking and pitting are often found at an early stage as localized faults.

- brinelling and smearing

Brinelling indentation often appears in the raceways which come into contact with the rolling elements, and is due to plastic deformation. The external cause can be extremely heavy loads, vibrations, faulty mounts and solid foreign matters [4]. Another possible cause is the electric current due to leakage [4]. Smearing is caused by sliding or spinning of balls, often happen when the balls enter the load zone. Brinelling damage often starts as a localized fault and develops into a distributed one.



Figure 7 Brinelling [10]

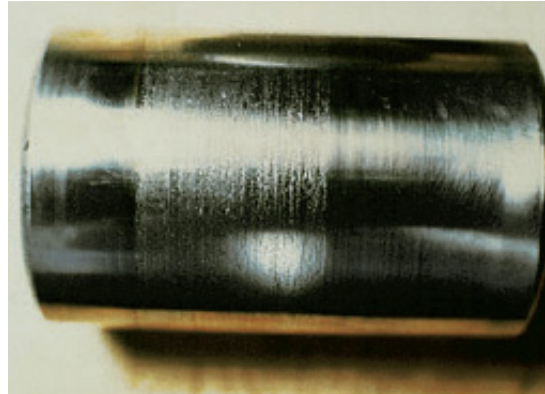


Figure 8 Smearing [10]

- rust and corrosion

Corrosion is the phenomena of oxidation or dissolution occurring on the contacting surfaces of a bearing. Sealing failure and decomposition of lubricant additives under high temperature are two primary reasons of corrosion damage [4]. The corrosion of bearing can result in the rust particles wearing off from the balls and raceways, which will further aggravate mechanical abrasion. This type of defect is commonly found as distributed faults.



Figure 9 Rust [10]



Figure 10 Corrosion [10]

In general, rolling bearings produce very little vibration when they are free of faults and have distinctive characteristic frequencies under faulty conditions [11]. Typical bearing faults usually begin as single defects, such as a spall on a raceway, and are normally dominated by impulsive events at the raceway pass frequency, resulting in a narrow band frequency spectrum, which can be captured by vibration sensor. As the damage increases, the characteristic defect frequencies and sidebands tend to spread over wider ranges, followed by a drop in these amplitudes and an increase in the broadband noise with considerable vibration at shaft rotational frequency [11].

1.4 Objectives of Research

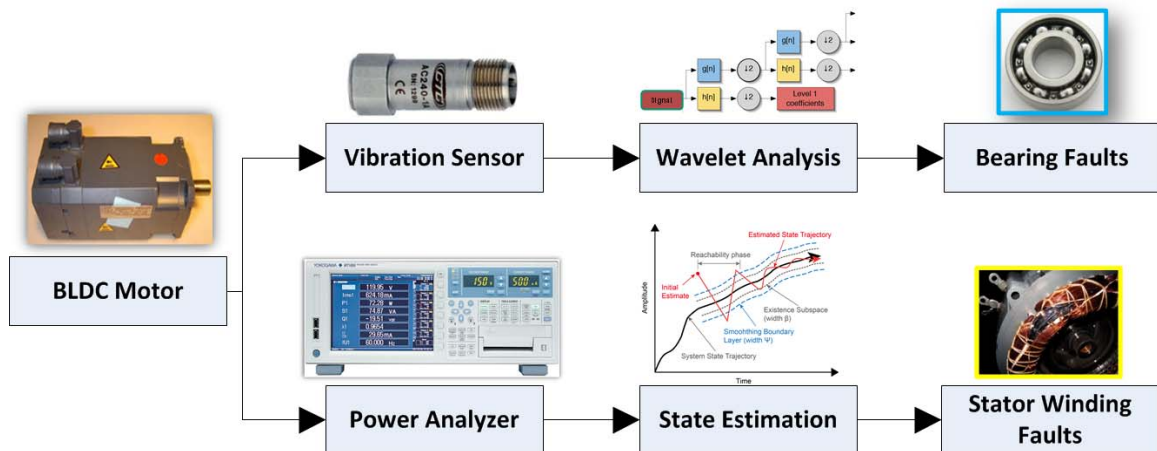


Figure 11 The proposed fault detection and diagnosis scheme for BLDC motor

This objective of this research has been to develop a Fault Detection and Diagnosis (FDD) strategy for detecting motor faults at their inception. Bearing

faults and stator winding faults, which are responsible for the majority of motor failures, were considered. These faults were physically simulated on a Permanent Magnet Brushless DC Motor (BLDC). The vibration and power measurements were then obtained for analysis, as shown in Figure 11. Two FDD strategies involving wavelets and state estimation were successfully implemented on the BLDC motor. Experimental results demonstrated that the proposed fault detection and diagnosis schemes were very effective in detecting bearing and winding faults in BLDC motors.

1.5 Outline of Thesis

This thesis is organized as follows. Chapter 2 reviews the main literature on the fault diagnosis of electric motors, including mechanical and electrical faults. In Chapter 3, the concepts of wavelet-based signal processing and feature extraction approach are described in detail. A proposed signal processing scheme based on wavelet denoising is also provided. Chapter 4 introduces the popular Kalman Filter and the Smooth Variable Structure Filter with varying boundary layer (EK-SVSF). It is also shown how these filters can be implemented on a BLDC motor for state and parameter estimation. In Chapter 5, experimental results are presented with comparisons and discussions on the performance of the proposed methods. It is shown that all simulated fault conditions were

successfully detected, which demonstrates the effectiveness of the proposed methods in motor fault detection and diagnosis. Recommendations for future research and concluding remarks are provided in Chapter 6.

Chapter 2 Literature Review

2.1 Overview

This section focuses on the literature of fault detection and diagnosis and their application to motors, particularly in BLDC motors. Although the vast majority of past research has been focused on induction machines, diagnostic approaches can be easily extended to other type of motors, such as PMSMs and BLDCs. Motors in many applications are operated under environmental stresses that often include high ambient temperature. As a key component, their malfunction can do harm to the production line, or even have severe consequences and cause heavy financial losses. For that reason, the development of fault detection and diagnosis tools for electric motors has received much attention since the 1920s [12]. A number of survey papers have been published and can be found in [13-16].

The major faults of electric motors can be broadly classified into two groups: mechanical faults such as the bearing faults, broken rotor bar and bent shaft; and electrical faults such as opening and shorting of a stator phase winding. A recent study revealed that the main causes of failure in electric motors are: bearing (69%), stator windings (21%), rotor bar (7%) and shaft/coupling (3%) [17].

2.2 Mechanical Faults

Mechanical faults in motors can be broadly classified into two groups: bearing faults and rotor faults. The rotor fault typically is a broken rotor bar or an eccentricity fault [18-23]. The bearing fault, according to industrial surveys [17], has caused far more motor failures than any other kind. Thus, the detection and diagnosis of bearing faults is chosen to be a primary focus of this study.

The bearing failure mechanism has been studied for almost four decades [24, 25]. As such, the theoretical foundation of bearing failure modes has been considered comprehensively [26]. While there are monitoring techniques based on different measurement sources, such as acoustic emission (AE) and motor current signature analysis (MCSA), vibration monitoring is probably the most widely used approach.

Vibration in an electric motor can come from many sources including bearings, electromagnetic forces, unbalanced rotors, etc. Each will have its own signature in the frequency domain that can manifest itself as discrete frequency bands. In order to extract fault signatures buried in vibration signals from the machine, advanced signal processing techniques are commonly used. These include filtering and feature extraction of the vibration data.

In terms of bearings, previous studies show that 90% of faults that occur in rolling bearings are due to cracks in inner and outer races, and the rest are

cracks in the balls and the cage [8]. In a defective bearing, a shock is generated when a rolling element passes over the defective surface of an inner race or an outer race. The frequency of these shocks is referred to as characteristic defect frequency or Ball Passing Frequency (BPF), and can be calculated using the parameters of the bearing. Meanwhile, these shocks can also be captured by vibration sensors. Thus, the bearing faults can be detected and diagnosed by matching the measured vibration spectrum with the calculated BPFs. The BPFs are computed based on the construction parameters of the bearing and the rotating speed of the shaft. The calculation of BPFI (Ball Passing Frequency Inner Race) and BPFO (Ball Passing Frequency Outer Race) are provided in Equation 2.2.1 and Equation 2.2.2 respectively.

$$\text{BPFI} = \frac{N_b \left(1 + \frac{d}{D} \cos\theta\right)}{2} \cdot \omega_r \quad \text{Equation 2.2.1}$$

$$\text{BPFO} = \frac{N_b \left(1 - \frac{d}{D} \cos\theta\right)}{2} \cdot \omega_r \quad \text{Equation 2.2.2}$$

where N_b is the number of rolling balls, θ is angle of load from the radial plane, d is the inner diameter of the bearing, D is the outer diameter of the bearing, and ω is the rotating speed. The parameters of the test bearing used in this research are provided in Appendix 1.

In the analysis of vibration measurement, signal modulation effect and noise are two major barriers in detecting the presence of bearing faults at early

stages. Due to the amplitude-modulated effect, the BPFs usually appear as sidebands of resonance frequency in the spectrum. This makes identifying the specific frequency components difficult. Thus, an effective signal demodulation technique should be used. Meanwhile, weak signatures produced by incipient bearing faults can easily be masked by noise in a real environment, making the fault detection even more difficult. Hence, a denoising algorithm is also necessary in order to enhance the extraction of characteristic features of bearing faults. To overcome these barriers, numerous studies have been conducted on signal processing techniques for bearing diagnosis.

In [27], an improved Hilbert-Huang transform (HHT) was combined with wavelet packet transform (WPT). The WPT was used as a preprocessor to decompose the signal into a set of narrow band signals, and then the decomposed signals were generated and selected by using empirical mode decomposition (EMD) on the signals. The EMD is a time adaptive decomposition operation developed to decompose a signal into some individual signals with 'Hilbert-friendly' waveforms [28]. The performance of the improved HHT was compared to wavelet-based scalograms. Experimental results showed that the proposed method had better resolution in time and frequency domain, as well as better computing efficiency. However, this approach had a distinct drawback, which was the ripple in the estimated frequency. That means the estimated frequency reflected the true frequency component only in the mean sense, and this could mislead the analysis.

In [8], the wavelet analysis was used to decompose the vibration signal, and a support vector machine (SVM) was utilized as a classifier for the multi-fault diagnosis of bearings in an electric motor. Results showed that all simulated bearing faults were successfully detected. A similar combination of methods was provided in [29], where the DWT was applied together with hidden Markov Models (HMMs) for pattern recognition.

In [30], an Improved Wavelet Packet Decomposition (IWPDP) was proposed and combined with Support Vector Data Description (SVDD) in order to detect bearing faults. Essentially, the measured signal was decomposed using the IWPDP. The energy of each element in these decomposed signals was computed to form the feature vectors. The feature vectors were then fitted into a hyper-sphere to train the SVDD, and used to create a health index for fault diagnosis.

In [31], spectral kurtosis (SK) was combined with autoregressive linear prediction filtering and minimum entropy deconvolution (MED), to extract transients buried in noisy measurements. MED was utilized to deconvolve the effect of transmission paths and obtain characteristic impulses, in order to achieve a high value of SK. The results indicated that this method was capable of effectively sharpening impulses, thus making fault features more evident.

With the occurrence and deterioration of a fault in a bearing, the number of frequency peaks contained in a measured vibration signal will increase [32]. This

can be quantified by approximate entropy (ApEn). In [32], the ApEn was used as a statistical criteria to measure the degradation of the health condition of bearings. The results showed that the proposed method can robustly characterise the severity of structural defects.

In [33], the intrinsic mode function (IMF) envelope spectrum is proposed to overcome the limitations of conventional envelope analysis such as the choice of filter central frequency. The approach utilized the empirical mode decomposition (EMD) to create the IMFs. Then, the fault features at the envelope spectra of the IMFs were marked, which were finally ported into a support vector machine for fault pattern recognition.

In [34], a denoising scheme was proposed to enhance weak signature of faults in bearing vibration signals. The denoising scheme utilized the Gabor wavelet transform to filter the measured signal, which was pre-processed by the spectral subtraction method. Spectral subtraction is a method for restoration of the spectrum of a signal observed in additive noise, where an average signal spectrum and average noise spectrum are estimated independently from the measurements, and are subtracted from each other to obtain an improvement in average signal-to-noise ratio [35]. The parameters of the wavelet function, such as scale and shape factors were selected based on a resonance estimation algorithm and a smoothness index respectively. The various cases of bearing

faults simulated in that study showed that the detectability of bearing faults were evidently improved.

The main advantage of envelope analysis is its ability to extract the weak periodic impacts which are modulated by structural resonance in machine, especially when the signal from the defective part is relatively low in energy. In [36], a multi-scale enveloping spectrogram was proposed as an improvement of conventional enveloping spectral analysis. In the conventional method, the signal bandwidth of interest must be known for consistent results. In this improved approach, different frequencies can be simultaneously extracted and separated. The complex wavelet transform was used to combine bandpass filtering and enveloping into one operation. The experimental results on bearings with localized defects showed the effectiveness of this technique.

In [37], The Morlet wavelets were investigated for the envelope detection and demodulation of vibration signals. A key contribution in the study was the systematic description of selection criteria for automated selection of wavelet parameters, which could have great influence on the performance of wavelet transforms.

The denoising approach based on wavelet shrinkage was also shown to be effective in many papers. Meanwhile, the selection of thresholding function attracted lots of interest. Since the quasi-optimal value of threshold was often unknown, in [38], a recursive algorithm was proposed to estimate the variance of

the noise with proved convergence. It was claimed that given the wavelet representation of the signal was sufficiently sparse (means a signal is efficiently encoded in only relatively few wavelet coefficients), the calculated limit threshold based on probability density function (PDF) of noisy signal equaled the theoretical value. Numerical comparison between the proposed method and Median Absolute Deviation (MAD) method was provided to demonstrate the effectiveness of the given approach. The MAD is a standard method that estimates the level of the noise in a signal by taking the median of the modulus of the finest-scale wavelet coefficients [39].

In [40], a customized wavelet denoising method that exploited intra-scale (neighbouring coefficients within one scale) and inter-scale (coefficients between different scales) dependency of wavelet coefficients was proposed. Similarly, a denoising scheme which takes into account the statistical dependencies among wavelet coefficients was proposed in [41]. Numerical simulation showed the Bivariate method had significant improvement over traditional methods such hard and soft thresholding in increasing the signal-to-noise ratio (detailed descriptions of Bivariate shrinkage method are provided in Chapter 3). The improvement was shown through simulated bearing vibration signals. The results of the proposed approach and conventional soft-thresholding and hard-thresholding were then compared. Similarly, in [42], a kurtosis-based hybrid thresholding method was proposed to dynamically adjust the thresholding values, and was shown to be effective in increasing signal-to-noise ratio. In [43], the kurtosis was used as an

optimization and evaluation criteria for the selection of parameters of wavelet transforms. The experimental results presented in the form of envelope spectra clearly indicated the bearing faults.

In [44], a denoising scheme based on dual-tree complex wavelet transform (DTCWT) was proposed for the feature enhancement of vibration signal from faulty bearing. The DTCWT was a complex-valued extension of the standard discrete wavelet transform (DWT), and was proved to have better shift invariance and reduced spectral aliasing than the DWT and the second-generation wavelet transform (SGWT) [45, 46]. A detailed description of DTCWT can be found in Chapter 3. After the decomposition of signal, a wavelet coefficient shrinkage approach was adopted to remove noise while retain important fault features. It was shown that the method was capable of detecting multiple faults simultaneously, with good robustness and computational efficiency. The experimental results based on a crack gear demonstrated the superiority of this method over SGWT and DWT for online surveillance and diagnosis.

Besides vibration-based techniques, fault detection methods based on Motor current signature analysis (MCSA) were also shown to be effective in bearing diagnosis. It is advantageous in the sense that they are readily available in the power converter and for signal processing, which means they are intrinsically non-invasive. There are a number of papers dealing with the detection and diagnosis of bearing faults based on current analysis [5, 47-52].

The approach relies on interpretation of the frequency components in the current spectrum that are related to bearing vibration. In [53], wavelet packet analysis was applied to the motor stator current to identify the modulation of stator current caused by bearing defects induced vibration. It was also shown that frequency bands can accommodate the rotational speed dependence providing a useful diagnostic for incipient bearing fault detection. In [54], an online diagnosis system using MCSA is proposed, with the ability of optimal-slip-estimation and frequency-auto-search. In [55], it was shown that mechanical imbalances caused harmonics in currents and voltages. It was also shown that mechanically induced speed oscillations give rise to sidebands components of the fundamental stator current frequency, and shaft misalignment causes modulation of the current by the shaft rotational frequency [16]. However, the current spectrum is influenced by many factors, such as electrical supply, static, and dynamic load conditions, noise, and motor geometry, all of which may lead to errors in fault detection [22]. Meanwhile, the majority of these papers consider steady-state machine operation at a constant supply frequency [50]. It should also be noted that internal vibrations caused by faults when coupled with external load vibrations can produce new harmonic components in the stator current, hence potentially leading to misdiagnosis.

Methods based on Acoustic Emission (AE) have also been extensively researched for bearing fault detection. The AE can be defined as the generation of transient elastic waves produced by a sudden redistribution of energy from

localized sources within a material [56-59]. One of the advantages of AE technology over the well-established vibration analysis is that it can detect the growth of sub-surface cracks before they appear in the vibration measurements [57], and at low speeds [11]. Some research claims that AE offers earlier fault detection than vibration analysis [60]. However, as a complementary diagnostic tool, the AE still has limitations due to the difficulty in processing, interpreting and classifying the acquired data. Furthermore, AE may detect a change in condition but has limited diagnostic capability [11].

2.3 Electrical Faults

For BLDC motors, the permanent magnets replace the rotor windings, thus the electrical faults are mostly stator-related. Two main classes of stator winding fault are: (i) the open-phase fault; and (ii) the shorted turns or the turn-to-turn insulation fault [50]. The former may allow the machine to operate with a reduced torque, while the latter one can quickly develop into an insulation failure and the complete breakdown of the machine. An insulation failure normally starts with an interturn short-circuit, which induces high current and much heat that burns the insulation. If left undetected, turn-to-turn faults will propagate to stator core, and lead to phase-phase or phase-ground failure [13]. This failure can occur within 60 seconds for small low-voltage motors, and usually lead to irreversible damage to the machine [61].

Model-based approaches are among the most commonly used techniques for the studying of short-circuit faults in electric motors. In [62], a parametric model was developed to simulate the operating conditions of a PMSM. As a novelty, the variation of spatial harmonics in back-EMFs due to the PM flux distribution was taken into account by the model. A similar approach was also used in [63].

In [64], a model-reference based method was proposed for the estimation of phase resistance and inductance in a PMSM. It was claimed that the performance of that approach was comparable to that of the Extended Kalman Filter [65], but was less computationally expensive. The method was applied with a decoupling control technique to improve convergence rate and overall stability. The implementation of EKF on PMSM was also found in [66], where the speed and position of the rotor were estimated using EKF. In that research, a self-tuning procedure was also proposed.

In [67], a fault diagnosis algorithm was proposed which considered modeling errors caused by process uncertainties, which were reflected by a time-varying stator resistance and inductance. The approach utilized the “adaptive residual generators” to improve the robustness of the algorithm. This was achieved by applying a decoupling block in feedback loop. However, the assumption that the stator winding resistance of all three phases are equal to each other is not practical under faulty winding conditions.

In [68], an online monitoring method was formulated for a PMSM in closed-loop drive system. The method combined a multi-model approach with the recursive least squares algorithm (RLS). The machine parameters estimated by the RLS were compared with the ones in a healthy condition. The interturn fault was detected when a residual exceeded a certain threshold. The challenge of model-based methods is the modeling uncertainties that might lead to incorrect detection of fault, as well as the nonlinearities that may be taken into account in the mathematical model [15].

In [69], the parameters of a brushless DC motor was estimated through a model-based approach. The faults in the stator winding resistance and the friction coefficient of the rotor were physically simulated. The results demonstrated that the increase of averaged winding resistance by 10% was successfully tracked.

Among various signal processing techniques, the motor current signature analysis (MCSA) has also drawn much interest. One of the reasons is that the current measurement is readily available in the drive, making this method non-invasive and not requiring any additional sensors. In [70], the MCSA was successfully applied to the motor current, by analyzing the spectrogram using the short-time Fourier transform (STFT) and a combined wavelet and power-spectral-density (PSD) approach. The method was shown to be able to effectively extract the frequencies produced by inter-turn shorts in the stator current. Yet, a good a

priori knowledge of the signals is needed in order to find the proper sampling frequency and wavelet basis.

The harmonics contained in the stator currents were also explored for the inter-turn fault detection [71]. It was proposed that search coils be installed on the motor rotor to improve accuracy. The advantage of this method is that only one signal needs to be monitored. Similar approaches were shown in [72-74].

In [75], positive and negative sequence third harmonics of line currents are used to find the signatures of interturn faults. It was shown that by utilizing the predefined information on sequence components, the influence of voltage unbalance and inherent asymmetries could be largely removed, thus providing more reliable fault signals.

A multiple reference frames theory was proposed in [76], which was shown to be immune to voltage unbalances. In this approach, the positive sequence of the stator currents was assumed to be the superposition of healthy machine currents and faulty machine currents. The healthy part of the signal was estimated using motor parameters and was removed from the measurements. The negative-sequence currents were also removed. The remaining faulty currents were then used for fault identification.

In [77], a fault diagnosis approach based on the variation of impedance Z_{np} was proposed, with special focus on closed-loop inverter drive that was

connected to multiple motors. The approach slightly differed from most methods in the sense that it took advantage of the current regulating effect of the motor controller. It was claimed that the robust and fast detection of turn-to-turn faults can be detected. However, the interaction of parallel motors in the presence of faults needed the independent measurement of each motor, and it didn't consider nonlinearities associated with the inverter.

High frequency (HF) signal injection has also been applied in fault detection of stator windings [78-83]. In [78], fault diagnosis was achieved by injecting a high frequency carrier signal to the motor, and measuring the resulting high frequency negative sequence current. The imbalance in the windings caused by faulty turns would lead to different direct and quadrature axis leakage inductances, and then the dc component was used as the fault indicator. This approach was shown to be advantageous in the sense that the results were almost independent of the excitation frequency, thus less sensitive to the variation of operating conditions. Similarly in [83], the negative-sequence currents induced from the high-frequency voltages were used to investigate the asymmetry fault in the machine. In [81], the HF injection and the space-modulation profiling (SMP) technique were used to monitor the phase inductance of the motor, which was believed to be related to electrical faults. The residual between a healthy inductance signature and faulty one was investigated to identify the faults. In [82], a similar approach was taken on a PMSM. The SMP technique was used to obtain the magnetic signature of healthy operating

scenario and stored in a look-up table. Then this pre-stored signature was utilized as a comparison for online measurements to identify faults.

In [84], a method was proposed based on the three-phase stator current envelopes through reconstructed phase-space transforms. A Gaussian mixture model and a Bayesian maximum likelihood classifier were used for the extraction and diagnosis of the short-circuit turns and broken rotor bar. It was shown that the approach had high accuracy in detecting a signal shorted turn under 50% rated load.

Meanwhile, the artificial neural network (ANN) has also proved to be effective in motor fault detection according to numerous studies. ANN strategies include supervised [85-88] and unsupervised methods [89-91]. In [91], an unsupervised ANN algorithm was proposed, together with principal component analysis (PCA), to extract the principal components of the $\alpha\beta$ stator currents. The results were then used to classify the faults as well as their severity. The merit of this method was that it did not require a priori system identification procedures.

2.4 Summary

Condition monitoring and fault diagnosis of electric motors are important features that can improve the reliability of industrial machinery. This chapter provided an overview of the mechanical faults and the electrical faults of electric

motors, with a special focus on bearing and stator winding faults. In terms of bearing faults, vibration-based techniques have been found to be most reliable. In order to enhance the characteristic features of a fault, a number of signal processing techniques have been proposed. Among them, the wavelet analysis has shown its superiority in signal denoising and feature extraction. In terms of stator winding faults, the model-based parameter estimation techniques were found to be most promising. These methods are non-intrusive and have the ability of tracking the variation of actual physical parameters.

Most of the reviewed literature, however, only considers the bearing faults or the stator winding faults exclusively. A combined strategy that can handle both of these faults would be more capable for practical use. Besides, for the wavelet-based methods applied on bearing diagnosis, the merits of complex wavelet transform in improving the signal denoising performance are not fully exploited. Moreover, the influence of modeling uncertainties on the parameter estimation of electric motors should be considered in order to provide a robust fault diagnosis scheme. Accordingly, a fault detection and diagnosis strategy based on wavelet analysis and robust state estimation techniques was proposed in this research; the implementation of the proposed methods on a BLDC motor was also investigated. Details of the proposed strategy and its implementation will be discussed in the following chapters.

Chapter 3 Bearing Fault Diagnosis Using Wavelet Transforms

In this study, bearing faults were detected by using wavelet-based signal processing techniques as shown in Figure 12. Signal denoising methods based on wavelet shrinkage and Dual-Tree Complex Wavelet Transform (DTCWT) are described. Some comparisons are provided to demonstrate the effectiveness of DTCWT in feature extraction and vibration signal denoising. Moreover, the kurtosis and the envelope analysis are introduced, both of which are essential tools in bearing fault diagnosis. The implementation of these tools on the fault diagnosis of bearings is discussed.

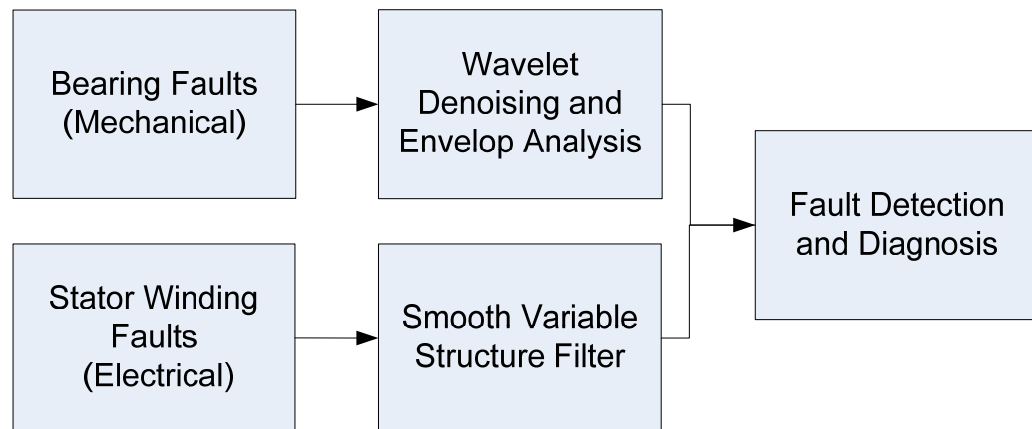


Figure 12 Fault diagnosis scheme

3.1 Kurtosis

Kurtosis is a mathematical representation that describes the impulsive features of time domain signals. It is defined as the fourth standardized moment:

$$Kurtosis = \frac{1}{N} \sum_{i=1}^N \left(\frac{x_i - \mu}{\sigma} \right)^4 \quad \text{Equation 3.1.1}$$

where x_i is the measured acceleration in time domain, μ and σ are mean and variance respectively, and N is the number of samples. Although kurtosis does not give any direct indication of the fault type, it provides a quantitative measurement of the degradation in health of a machine. As an example, a measured vibration signal from a healthy bearing is given in Figure 13.

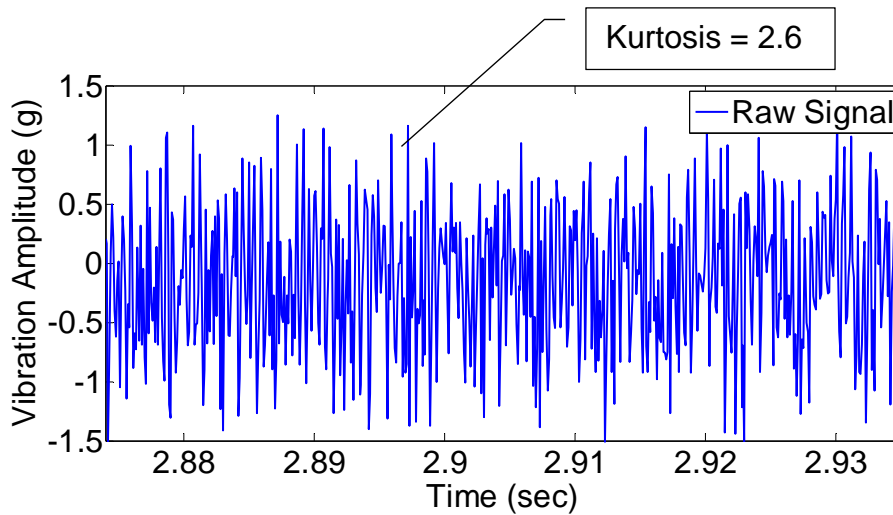


Figure 13 Typical vibration signal measured from a normal bearing

In contrast, Figure 14 shows the vibration signal of a motor with a defective bearing. The increase of kurtosis from 2.6 to 8.1 detects the bearing fault.

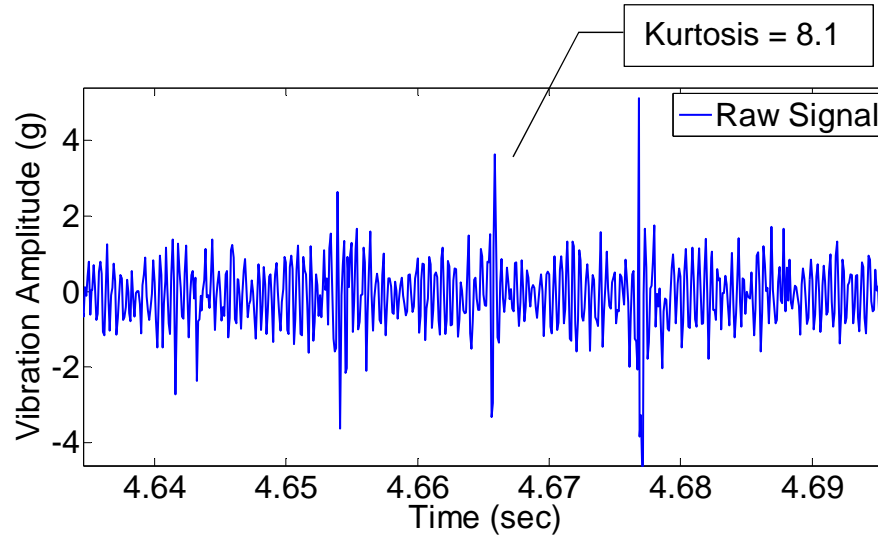


Figure 14 Typical vibration signal measured from a faulty bearing

3.2 Envelope Analysis

A. Amplitude Modulation

The concept of envelope analysis relates to amplitude modulation. Amplitude modulation is defined as the multiplication of one signal by another in time-domain. Either of the signals may contain harmonics, and since the modulation is inherently a non-linear process, it always gives rise to new frequency components that do not exist in the original signals. For example, the signal created according to Equation 3.2.1 have a time domain waveform shown in Figure 15.

$$f(t) = (\sin(0.04\pi \cdot t) + 1) \cdot \sin(0.4\pi \cdot t) \quad \text{Equation 3.2.1}$$

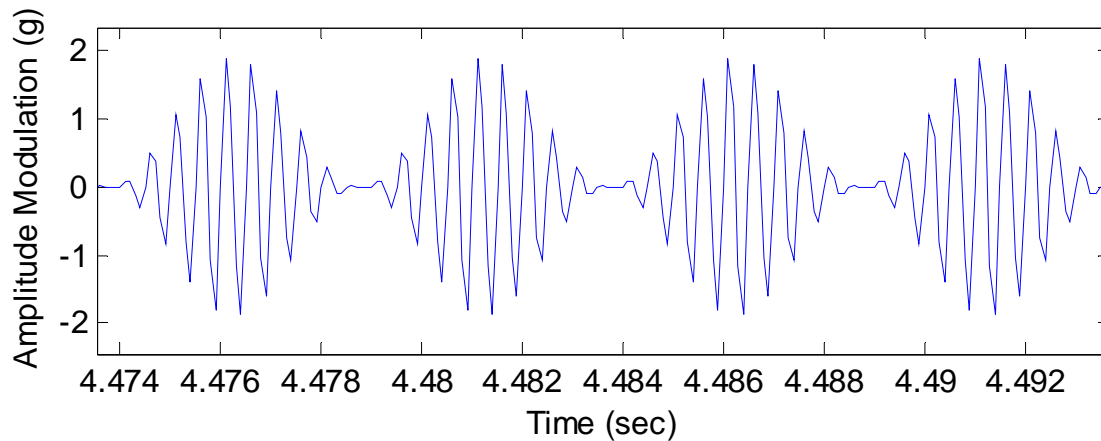


Figure 15 A simulated signal with amplitude modulation phenomenon

The signal shown in Figure 15 is amplitude modulated and is the multiplication of two sinusoidal waves with frequencies of 200 Hz and 2000 Hz. The higher frequency component is called the carrier frequency, and the lower one is the modulating frequency. The corresponding frequency spectrum is given in Figure 16. Ideally, two peaks should appear in the spectrum at 200 Hz and 2000 Hz. However, the spectrum only shows the carrier frequency at 2000 Hz with two symmetrical sidebands at 1800 Hz and 2200 Hz, and the 200 Hz component is not found.

This is analogous to the circumstances in bearing fault detection. A rolling element bearing with a defect on the outer race will produce a series of impacts occurring at the rate of ball passing. This is called Ball Passing Frequencies (BPF) or bearing defective frequency. These impacts, which are used as indicators of bearing faults, are amplitude modulated. The BPF is the modulating frequency and the structural resonance of the motor is the carrier frequency. Due to the

amplitude modulation effect, the he BPFs are usually not found in the spectrum of raw vibration measurement.

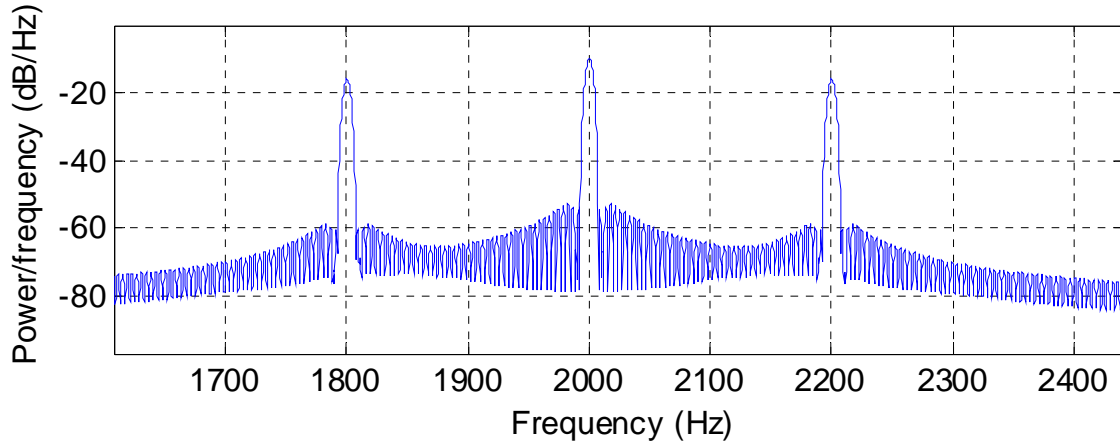


Figure 16 Frequency spectrum of the simulated signal

Meanwhile, the presence of sidebands can also mislead our analysis since these frequencies are not actually contained in the signal. Accordingly, the amplitude demodulation or envelope analysis is necessary for the extraction of BPFs in bearing fault detection.

B. Envelope Analysis Steps

Envelope analysis, also known as High Frequency Resonance Technique (HFRT), is an amplitude demodulation technique used to obtain the bearing defect harmonics from the spectrum for fault diagnosis purposes [92]. One of the most widely used methods to perform envelope analysis is to pass the signal through a band-pass filter to remove low-frequency components. Then perform rectification so that the defect frequency components can be determined in the

envelope spectrum [92]. The rectification here means to take the absolute value of a signal. The procedure of envelope analysis is given in Figure 17.



Figure 17 Diagram of signal processing steps in envelope analysis

As shown in Figure 17, the vibration signal is firstly passed through a band-pass filter around the resonance frequency in order to increase the signal-to-noise ratio (SNR). In this research, the band-pass filter used was a digital IIR filter of Butterworth type, with parameters given in Table 1 and bode plot shown in Figure 18. The filter was implemented in forward and reverse manner to remove the phase shift.

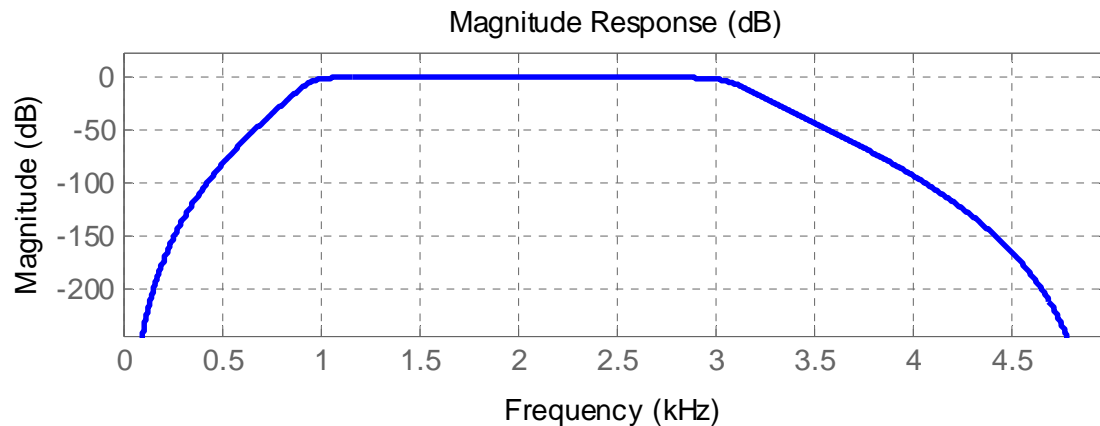


Figure 18 Bode plot of the digital IIR filter

The next step is rectification, which turns negative parts of the signal to positive. In traditional envelope analysis, the rectified signal is then processed

using low-pass filter to enhance the low-frequency features and leave out high-frequency noise. In this study, the low-pass filter is replaced by a wavelet denoising method based on Dual-Tree Complex Wavelet Transform (as described later in Section 3.3). The reason is that the DTCWT showed excellent performance in preserving the impulsive features at low frequency while filtering out noise [44-46]. Finally, the frequency spectrum of the denoised signal is created. The frequency components of periodic impulses that characterize the bearing faults (BPFs) can be found in the frequency spectrum, along with higher harmonics of it. As described in Section 2.2, the BPFs are calculated based on the speed of the motor and the construction parameters of the bearing.

Table 1 Parameters of the designed Butterworth digital IIR filter

Filter Parameter	Values
First Stopband Frequency	500 [Hz]
First Passband Frequency	1000 [Hz]
Second Passband Frequency	3000 [Hz]
Second Stopband Frequency	3500 [Hz]
First Stopband Attenuation	30 [dB]
Passband Ripple	1 [dB]
Second Stopband Attenuation	40 [dB]

C. An Example of Envelope Analysis

To show the effectiveness of envelope analysis, a simulated signal is created using Equation 3.2.2 as shown in Figure 19.

$$f(t) = (\sin(0.04\pi \cdot t) + 1) \cdot \sin(0.4\pi \cdot t) + \varepsilon(t) \quad \text{Equation 3.2.2}$$

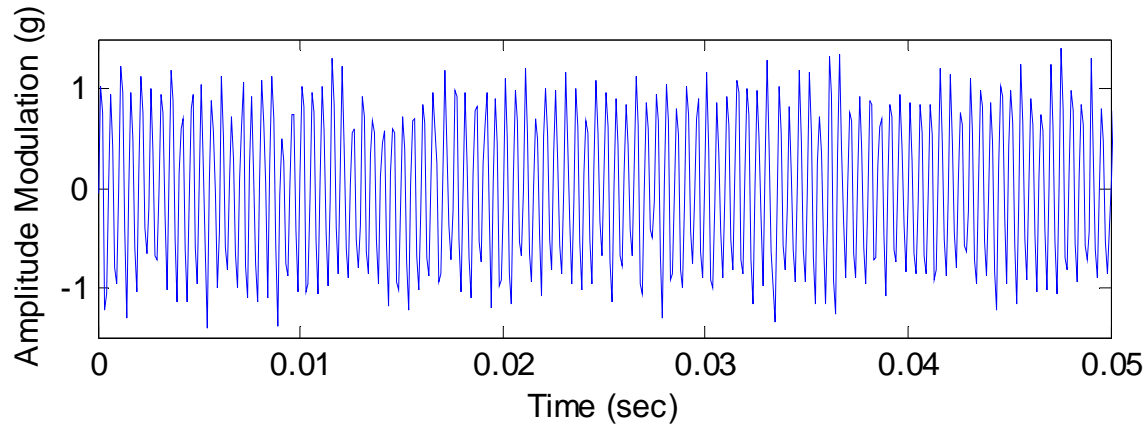


Figure 19 A simulated signal with modulating frequency at 200 Hz and carrier frequency at 2000 Hz

The signal is sampled at 10 kHz and is the multiplication of two sinusoidal waves at frequencies 2000 Hz and 200 Hz respectively. The 2000 Hz wave is the carrier frequency representing the natural resonance frequency of the motor, and the 200 Hz wave is a modulating frequency, representing the BPFO. A small amount of noise $\varepsilon(t)$ is added to the wave to better imitate practical conditions.

Figure 20 shows the spectrum of the simulated signal. It is very clear that the major component in the spectrum is the carrier frequency at 2000 Hz. As expected, the modulating frequency of 200 Hz cannot be found in the spectrum. Instead, it appears as two small sidebands spaced apart from the carrier frequency by 200 Hz. This is very confusing in practical situations and may result in overlooking of the bearing faults.

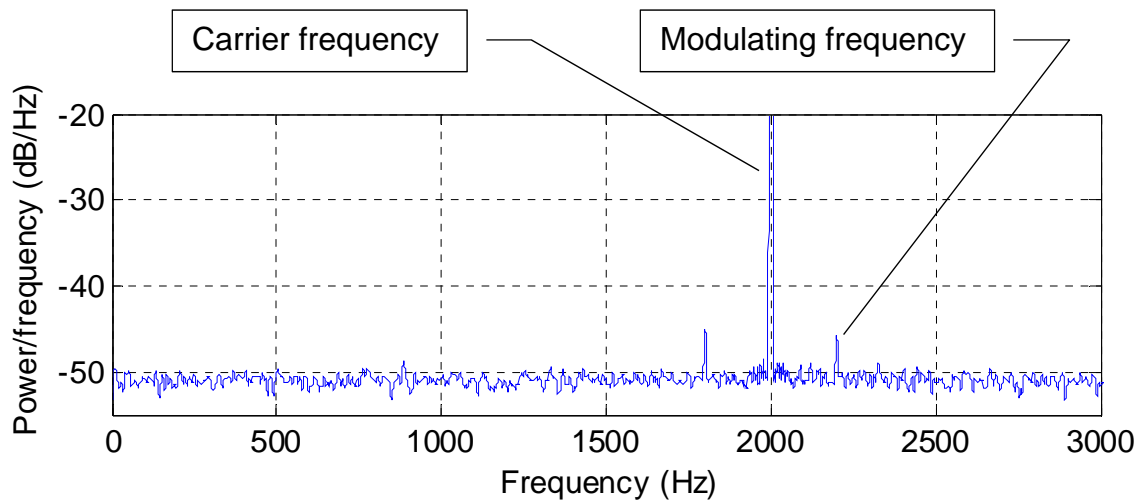


Figure 20 Frequency spectrum of simulated signal without any processing

Figure 21 shows the spectrum after applying envelope analysis. A frequency component of exactly 200 Hz appears, and the sidebands disappear. As we can see from the results, envelope analysis is very effective in discovering hidden frequency components, which is particularly suitable for bearing fault diagnosis.

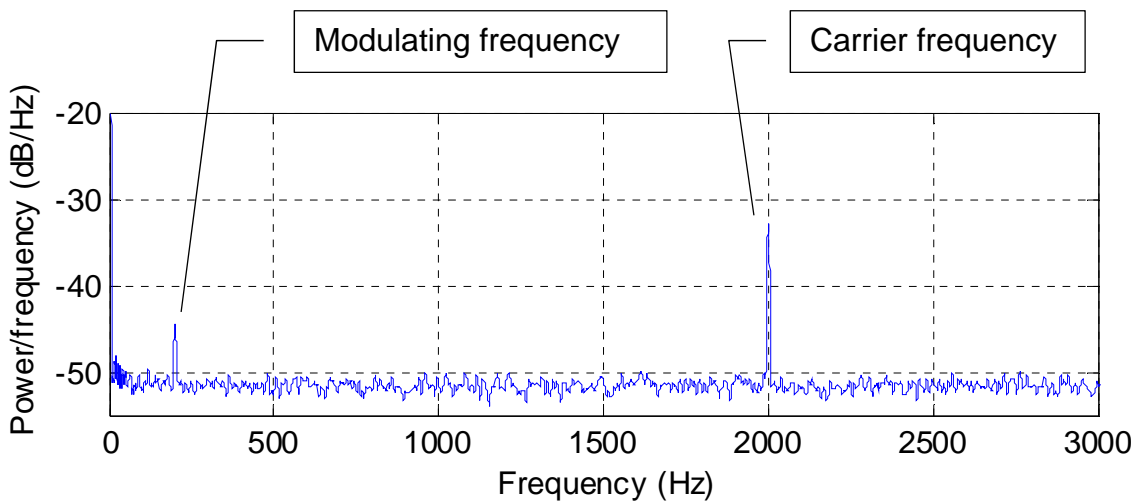


Figure 21 Frequency spectrum of simulated signal after amplitude demodulation

3.3 Dual-Tree Complex Wavelet Transform (DTCWT)

As discussed in Chapter 2, the discrete wavelet transform (DWT) has been widely used in signal processing applications due to its favorable time-frequency resolution. The DWT however suffers a few limitations, and one of them is the lack of shift-invariance property. The Dual-Tree Complex Wavelet Transform (DTCWT) is a relatively new enhancement to the DWT with a nearly shift-invariant property [45], which makes DTCWT particularly suitable for signal denoising.

The lack of shift invariance in conventional DWT means that a small shift in the input signal causes large changes in the wavelet coefficients, large variations in the distribution of energy at different scales, and possibly large changes in reconstructed signal. In the wavelet denoising process, the thresholding operation alters the value of wavelet coefficients. Thus, when the signal reconstruction is performed using the altered wavelet coefficients, the lack of shift invariance will lead to unfavorable artifacts in the reconstructed signal, and degrade the signal denoising performance. Accordingly, wavelet-based signal denoising methods will perform better when implemented with a shift-invariant transform. Since the DTCWT has approximate shift-invariance property, it is very suitable for wavelet denoising applications.

In DTCWT, the signal $x(t)$ is decomposed and reconstructed by two sets of filter banks, namely the real tree and imaginary tree. Both of the real and

imaginary trees consist of low-pass scaling functions $\phi(t)$ and high-pass wavelets $\psi(t)$ at each scale.

Let $\psi_h(t)$ and $\psi_g(t)$ denote two real wavelets used in the DTCWT. The complex-valued wavelet $\psi^C(t)$ is defined as:

$$\psi^C(t) = \psi_h(t) + j\psi_g(t) \quad \text{Equation 3.3.1}$$

The wavelet coefficients $d_l^{\Re}(k)$ and the scaling coefficients $c_J^{\Re}(k)$ (for the real tree) are computed via inner products:

$$d_l^{\Re}(k) = 2^{l/2} \int_{-\infty}^{+\infty} x(t) \psi_h(2^l t - k) dt, \quad l = 1, \dots, J \quad \text{Equation 3.3.2}$$

$$c_J^{\Re}(k) = 2^{J/2} \int_{-\infty}^{+\infty} x(t) \phi_h(2^J t - k) dt \quad \text{Equation 3.3.3}$$

where l denotes the scale of decomposition, and J is the maximum scale. Similarly, the corresponding wavelet coefficients $d_l^{\Im}(k)$ and $c_J^{\Im}(k)$ (for imaginary tree) can be computed by replacing the $\psi_h(t)$ and $\phi_h(t)$ with $\psi_g(t)$ and $\phi_g(t)$ respectively, as given below:

$$d_l^{\Im}(k) = 2^{l/2} \int_{-\infty}^{+\infty} x(t) \psi_g(2^l t - k) dt, \quad l = 1, \dots, J \quad \text{Equation 3.3.4}$$

$$c_J^{\Im}(k) = 2^{J/2} \int_{-\infty}^{+\infty} x(t) \phi_g(2^J t - k) dt \quad \text{Equation 3.3.5}$$

A detailed description of the selection of wavelet functions for DTCWT is provided in [93]. It was also claimed in [44] that similar results can be achieved

using different wavelet basis provided in [93]. In this research, the 14-tap Q-shift filters provided in [94] were used, as shown in Figure 22.

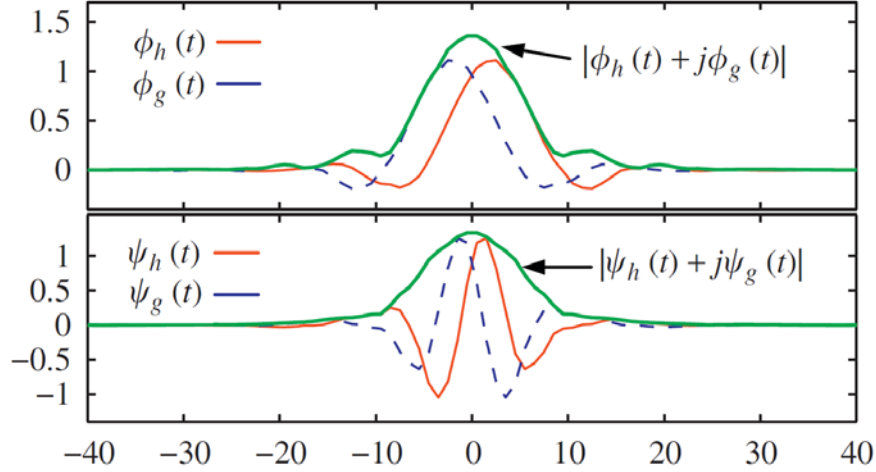


Figure 22 Scaling function and wavelet function of the 14-tap Q-shift filters

The wavelet coefficients $d_l^C(k)$ and scaling coefficients $c_j^C(k)$ of DTCWT are then obtained by combining the output of the dual trees:

$$d_l^C(k) = d_l^{\Re}(k) + jd_l^{\Im}(k), \quad l = 1, \dots, J \quad \text{Equation 3.3.6}$$

$$c_j^C(k) = c_j^{\Re}(k) + jc_j^{\Im}(k) \quad \text{Equation 3.3.7}$$

Figure 23 illustrates a two-stage decomposition and reconstruction process. The $h(m)$ and $g(n)$ represent the real and imaginary filters respectively, where m and n denote the length of the filter. The subscript “1” denotes a high-pass filter, and the subscript “0” denotes a lowpass filter. As shown in Figure 23, the decomposition and reconstruction of DTCWT is an iterative process similar to that of the DWT [95], except for the fact that two sets of filter banks (real and imaginary) are used simultaneously.

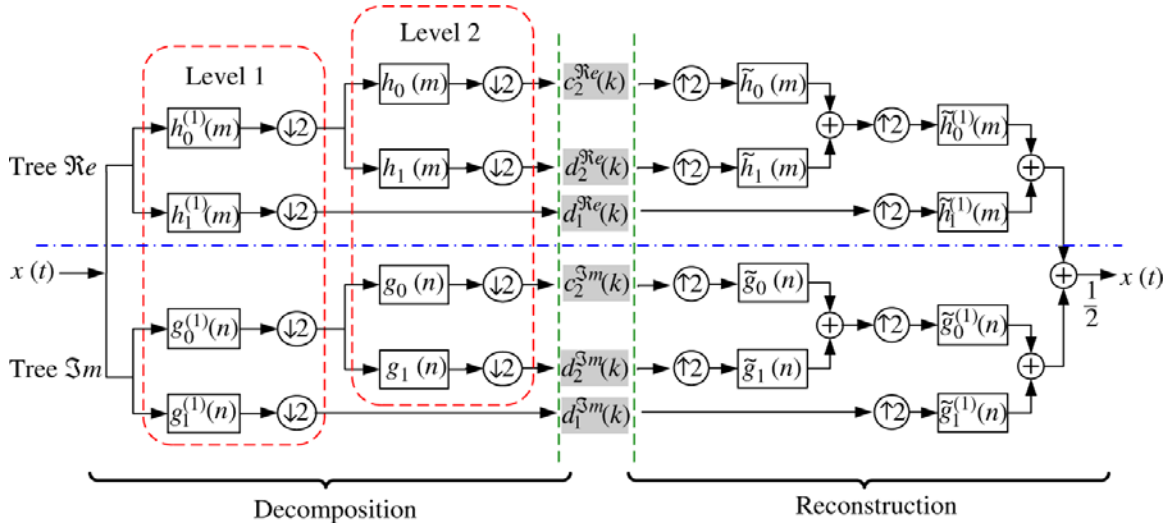


Figure 23 The dual-tree filter banks for decomposition and reconstruction [44].

The reconstruction of the signal $x(k)$ can be obtained from the wavelet coefficients and the scaling coefficients by following equations:

$$c_{l+1}^{\Re}(k) = \sum_m h_0(m - 2k) c_l^{\Re}(m) \quad \text{Equation 3.3.8}$$

$$d_{l+1}^{\Re}(k) = \sum_m h_1(m - 2k) c_l^{\Re}(m) \quad \text{Equation 3.3.9}$$

$$c_l^{\Re}(k) = \sum_m \tilde{h}_0(k - 2m) c_{l+1}^{\Re}(m) + \sum_m \tilde{h}_1(k - 2m) d_{l+1}^{\Re}(m) \quad \text{Equation 3.3.10}$$

Similarly, the reconstruction of the imaginary part is given as:

$$c_{l+1}^{\Im}(k) = \sum_n g_0(n - 2k) c_l^{\Im}(n) \quad \text{Equation 3.3.11}$$

$$d_{l+1}^{\Im}(k) = \sum_n g_1(n - 2k) c_l^{\Im}(n) \quad \text{Equation 3.3.12}$$

$$c_l^{\Im}(k) = \sum_n \tilde{g}_0(k - 2n) c_{l+1}^{\Im}(n) + \sum_n \tilde{g}_1(k - 2n) d_{l+1}^{\Im}(n) \quad \text{Equation 3.3.13}$$

In addition, if necessary, the scaling and wavelet coefficients can be reconstructed independently using following equations:

$$d_l(t) = 2^{\left(\frac{l-1}{2}\right)} \left[\sum_n d_l^{\Re}(k) \psi_h(2^l t - n) + \sum_m d_l^{\Im}(k) \psi_g(2^l t - m) \right] \quad \text{Equation 3.3.14}$$

$$c_j(t) = 2^{\left(\frac{j-1}{2}\right)} \left[\sum_n c_j^{\Re}(k) \phi_h(2^j t - n) + \sum_m c_j^{\Im}(k) \phi_g(2^j t - m) \right] \quad \text{Equation 3.3.15}$$

The $d_l(t)$ and $c_j(t)$ are real and have the same length as the signal $x(t)$.

3.4 Application of Wavelet Transform in Signal Denoising

3.4.1 Shrinkage-based Wavelet Denoising

The wavelet shrinkage [96] is a signal denoising technique based on the operation of thresholding the wavelet coefficients. During the shrinkage process, the wavelet coefficients having small absolute value are considered to encode mostly noise, while the wavelet coefficients having large absolute value are believed to encode important information. The denoising is thus achieved by setting the small absolute value coefficients to zero, and then reconstructing the signal with thresholded coefficients. As such, a higher signal-to-noise ratio can be achieved in the reconstructed signal.

The general steps followed in a wavelet denoising process are illustrated in Figure 24, and are summarized as follows [97]:

- (1). Obtain the wavelet coefficients by applying the wavelet transform to the noisy signal.
- (2). Estimate a threshold value and apply the threshold function to remove (zero out) the coefficients that are smaller than the threshold.
- (3). Reconstruct the signal by applying the inverse wavelet transform.

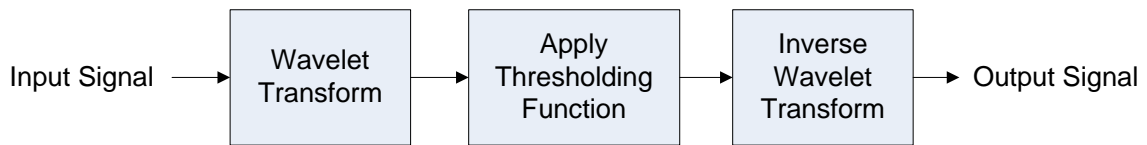


Figure 24 The Wavelet Shrinkage Procedures

Finding an appropriate threshold value and threshold function are the keys to wavelet shrinkage. Lots of studies have been conducted on these aspects [98]. Some of the classical threshold functions are hard thresholding and soft thresholding [96]. The idea of hard thresholding and soft thresholding are illustrated by Figure 25. Basically, the hard thresholding function sets the input coefficients smaller than the threshold to zero, and leave the input coefficients larger than the threshold unchanged. In contrast, the soft thresholding function not only sets the small coefficients to zero, but also scales the large ones.

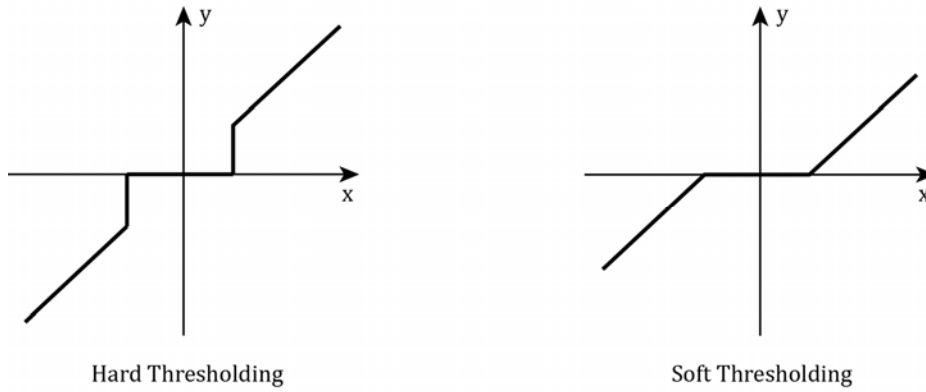


Figure 25 Hard and Soft Thresholding (x – input coefficient, y – thresholded coefficient)

3.4.2 Bivariate Shrinkage

In [41], a wavelet shrinkage method named Bivariate shrinkage was proposed. It was shown that the Bivariate shrinkage offered significant improvements in denoising performance over the conventional thresholding functions such as hard thresholding and soft thresholding. In traditional thresholding functions, a fixed threshold is applied to wavelet coefficients in a term-by-term fashion. In Bivariate shrinkage, however, the threshold is dynamically adjusted for each wavelet coefficient by taking into account the statistical dependencies among wavelet coefficients of different scales.

Let $y_{i,j}$ represent a wavelet coefficient at position i and scale j . Then, $y_{i-1,j}$ and $y_{i+1,j}$ are neighbouring coefficients in the same scale as $y_{i,j}$, while $y_{i,j-1}$ and $y_{i,j+1}$ are at the same position as $y_{i,j}$ but in neighbouring scales. The core concept of Bivariate shrinkage is that, if the neighbouring coefficients, such

as $y_{i-1,j}$ and $y_{i+1,j}$, contain much information (coefficients with large absolute value), then it is likely that $y_{i,j}$ will also do, thus a small threshold should be used for shrinking $y_{i,j}$. Similarly, if $y_{i,j-1}$ and $y_{i,j+1}$ contain much information, then it is likely that $y_{i,j}$ will also do, thus a small threshold should be used for shrinking $y_{i,j}$. By incorporating the intra- scale and inter-scale dependency information, a locally adaptive shrinkage function can be realized which achieves better denoising performance [41].

The procedures of Bivariate Shrinkage are summarized as follows. More details on the derivation and theoretical proof can be found in [41].

- (1). Transform the noisy signal vector $\mathbf{X} = [x_k]_{k \in [1,K]}$ into a matrix of wavelet coefficients \mathbf{Y} using DTCWT (as described in Section 3.3), where $\mathbf{Y} = [y_{i,j}]_{i \in [1,I], j \in [1,J]}$. The $y_{i,j}$ is individual wavelet coefficient at position i and scale j .
- (2). Estimate the variance of the noise contained in the wavelet coefficients $y_{i,j}$ based on coefficients of the finest scale $y_{i,J}$, using a robust median estimator [99],

$$\hat{\sigma}_{Nj}^2 = \frac{\text{median}(|y_{i,j}|)}{0.6745} \quad \text{Equation 3.4.1}$$

and the variance of noisy coefficients $\hat{\sigma}_{Y_{i,j}}^2$ is calculated as,

$$\hat{\sigma}_{Y_{i,j}}^2 = \frac{1}{L} \cdot \sum_{i \in [i-L/2, i+L/2]} y_{i,j}^2 \quad \text{Equation 3.4.2}$$

The variance $\hat{\sigma}_{Y_{i,j}}^2$ is calculated using the coefficients within a square-shaped window centered at the i th coefficient, where L is the size of the window. Then, the estimated variance $\hat{\sigma}_{W_{i,j}}^2$ of the wavelet coefficients can be obtained as

$$\hat{\sigma}_{W_{i,j}}^2 = \max(\hat{\sigma}_{Y_{i,j}}^2 - \hat{\sigma}_{N_j}^2, 0) \quad \text{Equation 3.4.3}$$

(3). The Bivariate Shrinkage factor $\beta_{i,j}$ is obtained as:

$$\beta_{i,j} = \frac{\max\left(\sqrt{y_{i,j}^2 + y_{i,j-1}^2} - \frac{\sqrt{3} \cdot \hat{\sigma}_{N_j}^2}{\hat{\sigma}_{W_{i,j}}}, 0\right)}{\sqrt{y_{i,j}^2 + y_{i,j-1}^2}} \quad \text{Equation 3.4.4}$$

(4). For each noisy wavelet coefficient $y_{i,j}$, the estimated wavelet coefficient $w_{i,j}$ is obtained using the Bivariate Shrinkage factor:

$$\hat{w}_{i,j} = \beta_{i,j} \cdot y_{i,j} \quad \text{Equation 3.4.5}$$

(5). Finally, the denoised signal vector \hat{X} is obtained from the estimated wavelet coefficients $\hat{w}_{i,j}$ via the inverse DTCWT transform (as described in Section 3.3).

3.5 The Proposed Denoising Scheme

The proposed signal denoising scheme is shown in Figure 26. The raw vibration signal is firstly processed by the envelop analysis method (bandpass filtering and rectification). Then, the resulting signal is transformed into wavelet coefficients using DTCWT. Next, the noisy wavelets coefficients are filtered via Bivariate shrinkage method, as described in Section 3.4.2. The denoised wavelet coefficients are then inversely transformed back to time domain to obtain the denoised signal. After the denoised signal is obtained, the frequency spectrum and wavelet scalogram of the denoised signal are produced, where the Ball-passing Frequencies present as the signatures of bearing faults.

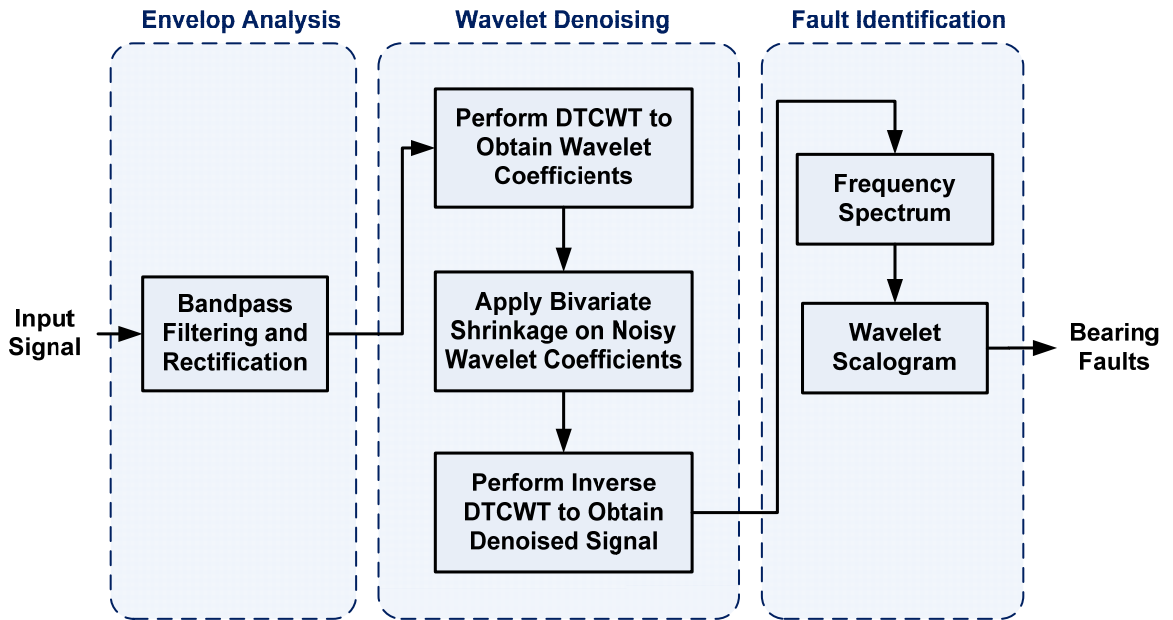


Figure 26 The proposed signal denoising scheme

The Matlab Code of the denoising scheme is provided in the Appendix 3.

An Example of DTCWT-based Signal Denoising

The DTCWT has better performance over conventional DWT in terms of better shift invariance property and reduced aliasing effect [44-46, 93], which make it very effective for extracting periodic shocks and enhancing harmonic features [44]. An example of DTCWT-based signal denoising is provided as follows, where a digital filter is used as a comparison to the DTCWT-based denoising method.

In this example, a signal was created to simulate the impulses generated by the defective part of a bearing. The signal contained a sinusoidal component that was attenuated by an exponential function, with additive Gaussian noise. The simulated signal $f(t)$ can be expressed as:

$$f(t) = 0.006 \cdot e^{D(t)} \cdot \sin(1000 \cdot 2\pi \cdot t) + \varepsilon(t) \quad \text{Equation 3.5.1}$$

$$\text{where } D(t) = 1000 \cdot \text{Max}(0, 0.01 - \text{Mod}(t, 0.02)) - 1;$$

The *Mod* was a function that takes the modulus after division, and the *Max* was to compare a given number with 0 and take the larger one. The $\varepsilon(t)$ was additive noise. The sampling frequency was 10 kHz. The periodic impacts generated by the faulty bearing had a frequency of 200 Hz. The designed low-pass digital filter had a cut-off frequency of 200 Hz, with detailed parameters listed in Table 2. The phase delay of the digital filter had been removed. The DTCWT denoising parameters were kept the same as those used in the processing of experimental

results in Chapter 4. As listed in Table 5, the number of scales (J) is 5, and the window size (L in Equation 3.4.2) is set as 200.

Table 2 Design parameters of the digital IIR filter

Filter Type	Passband	Stopband	Passband ripple	Stopband attenuation	Order
Butterworth (IIR), Direct-Form II	200 [Hz]	250 [Hz]	1 [dB]	80 [dB]	45

Table 3 DTCWT parameters

Number of Scales (J)	Window Size (L)
5	200 [samples]

The signal displayed in Figure 27 (a) was the simulated vibration signal, and was input into the DTCWT and the digital filter for denoising respectively. The four impulses shown in Figure 27 (a) are caused by bearing faults. An ideal denoising approach would preserve these impulses while filtering out noise.

The denoising results are given in Figure 27 (b) and (c). Apparently, the DTCWT successfully filtered out the noise while keeping the impulsive features to a great extent. The IIR filter, however, produced an over-smoothed signal where the peaks could hardly be distinguished. This example demonstrates the advantages of DTCWT in signal denoising and feature extraction, particularly for bearing fault diagnosis.

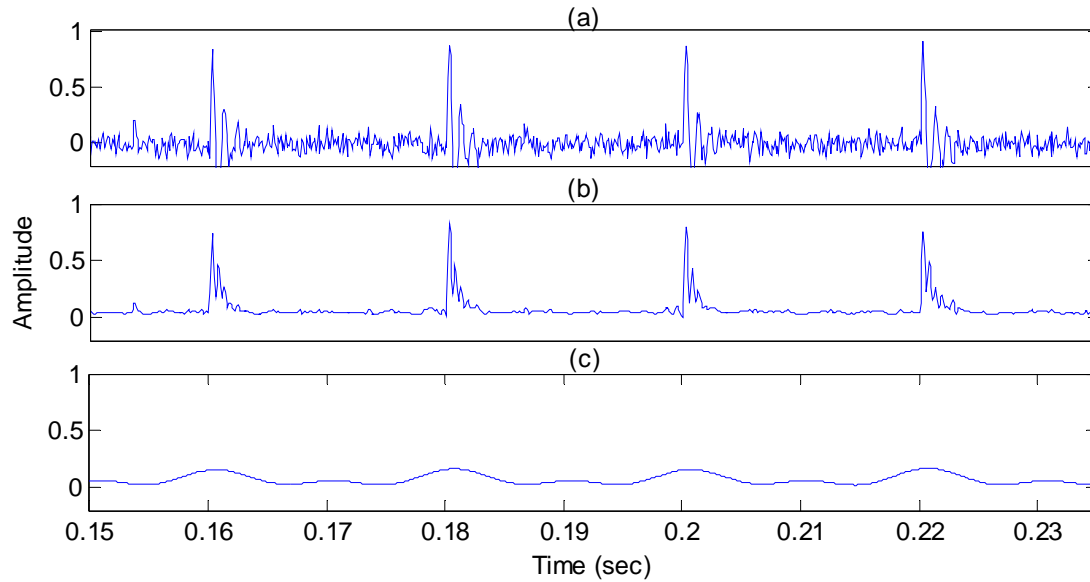


Figure 27 (a) Simulated vibration signal from a faulty bearing; (b) Denoised signal using DTCWT; (c) Denoised signal using digital IIR filter

It is worth pointing out that the sparseness of wavelet representation is one of the most important reasons for using wavelet transform for bearing fault diagnosis. Wavelet transforms have an energy compaction property. That means the transforms of the signal consists of a few large coefficients representing primary signal features, and many small coefficients that are considered to be noise. By keeping the large coefficients and suppressing the small coefficients, the noise can be filtered out without losing the important features of the signal.

3.6 Summary

The signal-based denoising techniques are important tools in fault detection and diagnosis. This chapter provided some of the most effective signal

processing tools for the bearing fault diagnosis. The Dual-Tree Complex Wavelet Transform was introduced and its appealing properties over conventional DWT were discussed. The shrinkage-based wavelet denoising method that utilized the DTCWT was then explained. Meanwhile, the envelope analysis was introduced with examples that demonstrated its effectiveness in extracting the bearing characteristic frequencies. Furthermore, the implementation steps of this denoising approach were summarized. The corresponding experimental results of this approach on the test motor are provided in the following chapters.

Chapter 4 Experimental Results of Bearing Fault Diagnosis

This chapter provides experimental results of the fault detection and diagnosis (FDD) methods applied to a test motor, for the bearing faults and the stator winding faults. In terms of bearings, previous studies show that 90% of faults that occur in rolling bearings are due to cracks in the inner and the outer races [8]. Accordingly, four bearing conditions were considered in this study, namely the normal condition, the outer race fault, the inner race fault and the presence of both the inner and outer race faults. The vibration of the machine was measured, and the DTCWT-based signal processing techniques were applied for the diagnosis of these faults.

The FDD results were obtained using the proposed signal denoising scheme described in Section 3.5. The flowchart of this denoising scheme is shown in Figure 28. The denoising scheme consists of three processes, namely envelop analysis, wavelet denoising and fault identification. The core of this scheme is the wavelet denoising process, where the input signal is firstly transformed into wavelet coefficients via DTCWT. Then, the wavelet coefficients are thresholded using Bivariate Shrinkage in order to denoise the coefficients. Finally, the denoised coefficients are inversely transformed back to time domain to obtain the denoised signal. In following part of this chapter, the FDD results obtained using the aforementioned methods will be presented.

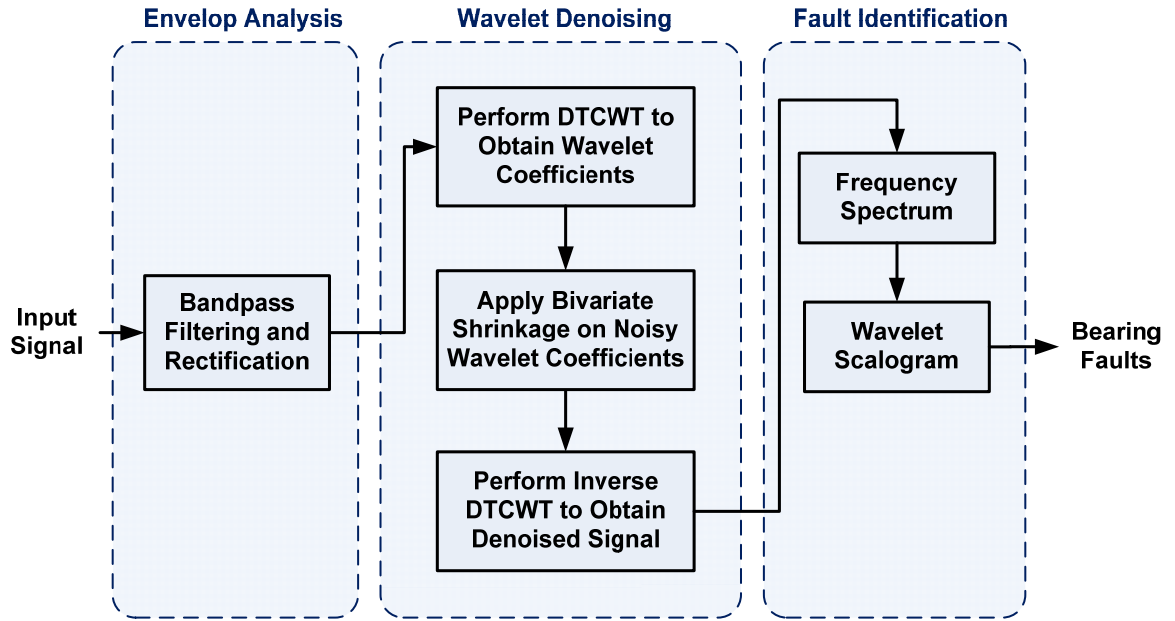


Figure 28 The proposed signal denoising scheme (same as Figure 26)

4.1 Outer Race Fault

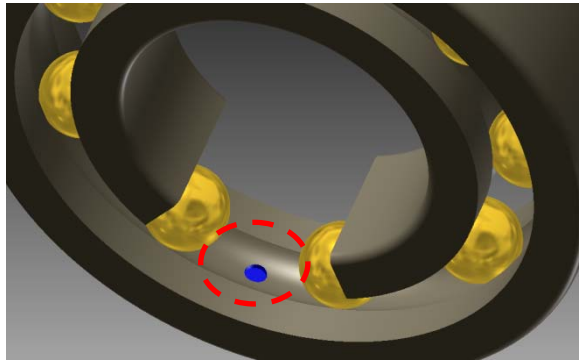


Figure 29 Inventor model of the test bearing with an outer race defect

In an attempt to physically simulate the outer race fault, a small dent was created on the outer race of the bearing using electro-chemical etching method,

as highlighted in Figure 29. As described in Section 2.2, when the rolling balls passed over the defective area, periodic shocks were produced. These shocks were captured by vibration sensors for fault diagnosis. Details of the experimental setup are provided in Appendix 1.

4.1.1 Case 1: 1200 RPM

During this test, the motor was running at 1200 RPM, and the data collection lasted for 10 seconds each time. The corresponding Ball Passing Frequency Outer Race (BPFO) at 1200 RPM was calculated according to Equation 2.2.2 as $f_o = 71.28$ Hz .

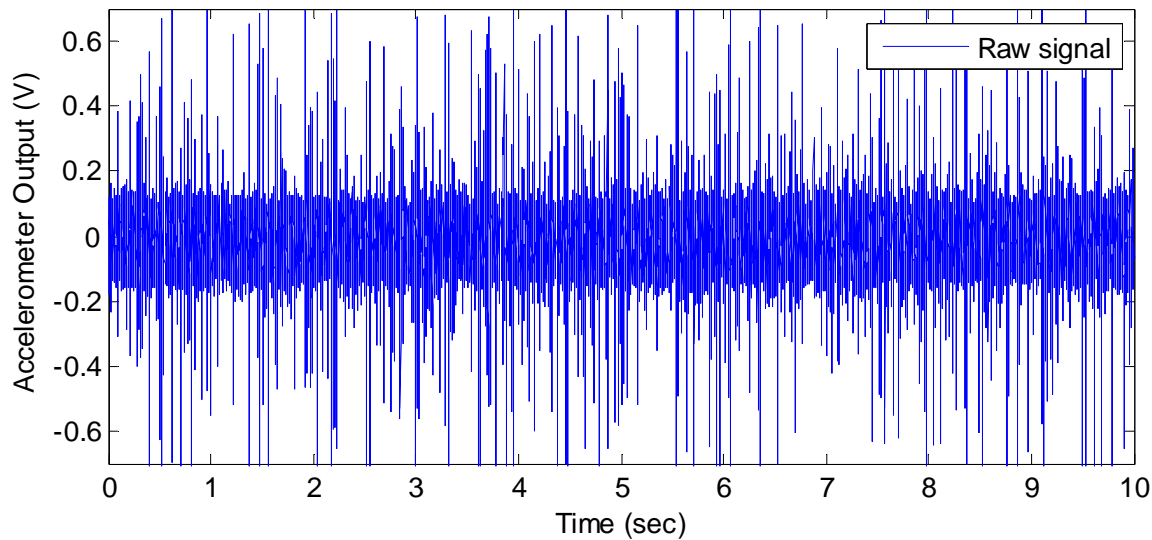


Figure 30 Raw vibration signal from the faulty bearing at 1200 RPM

The measured vibration signal is shown in Figure 30. As described in Section 2.2, the BPFO was calculated based on the motor speed and the parameters of the bearing, and was used as an indicator of bearing faults.

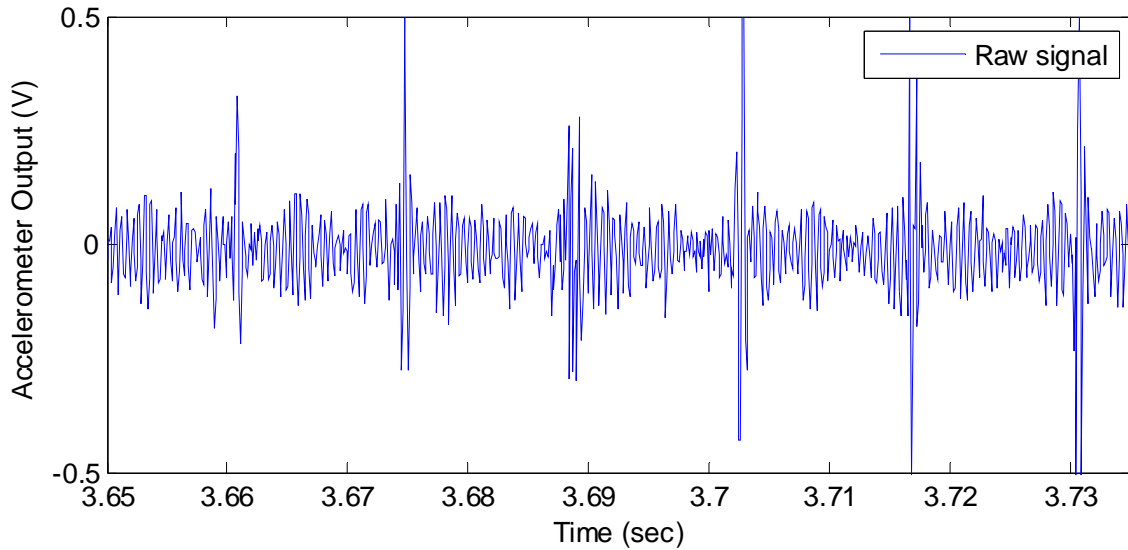


Figure 31 Partial enlarged signal from the faulty bearing at 1200 RPM

In Figure 31, the vibration signal in time-domain is partially enlarged. Figure 32 is the demodulated and denoised signal after applying the DTCWT-based processing algorithm. It is clear that the noise has been greatly reduced compared to Figure 31. The periodic impulses can be easily identified on this plot. The time period of them is 14.03 ms, corresponding to 71.3 Hz, which correctly matches with the calculated BPFO at 71.28 Hz.

Figure 33 is the denoised signal from the normal bearing. Compared with Figure 32, the denoised signal from a healthy bearing is usually a smooth one with much smaller amplitude and minor fluctuations, and most important of all,

shows no sharp impulse. By comparing the time domain signals such as Figure 32 and Figure 33, it is very easy to distinguish a faulty bearing and a normal one.

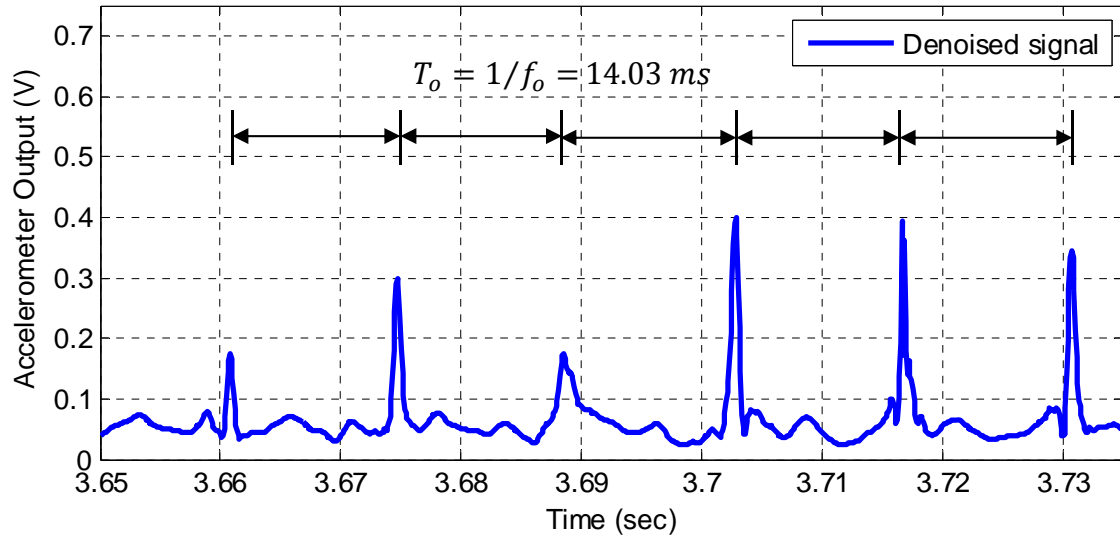


Figure 32 DTCWT-denoised signal from the faulty bearing at 1200 RPM

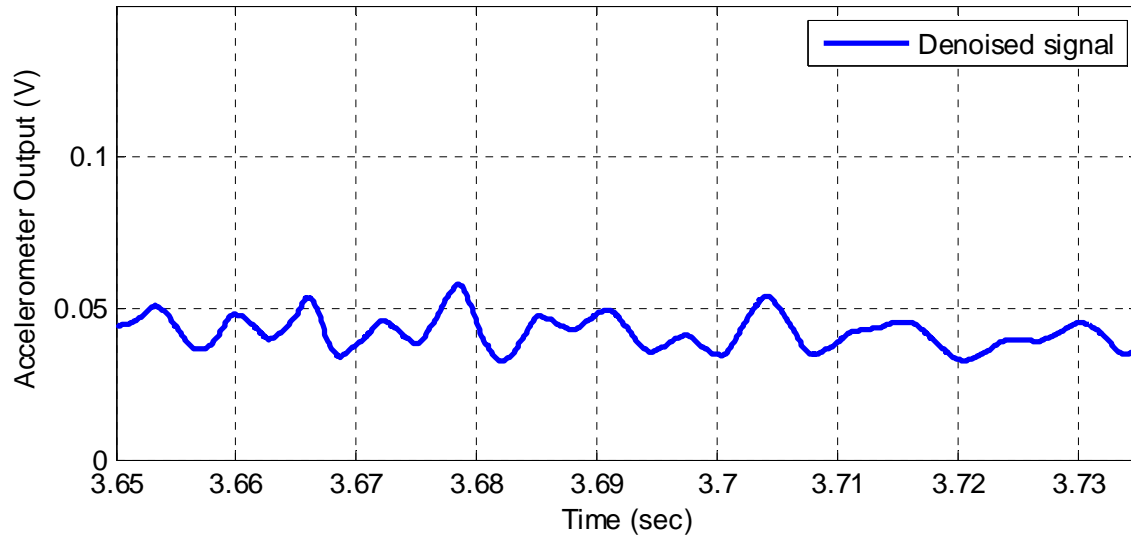


Figure 33 DTCWT-denoised signal from the normal bearing at 1200 RPM

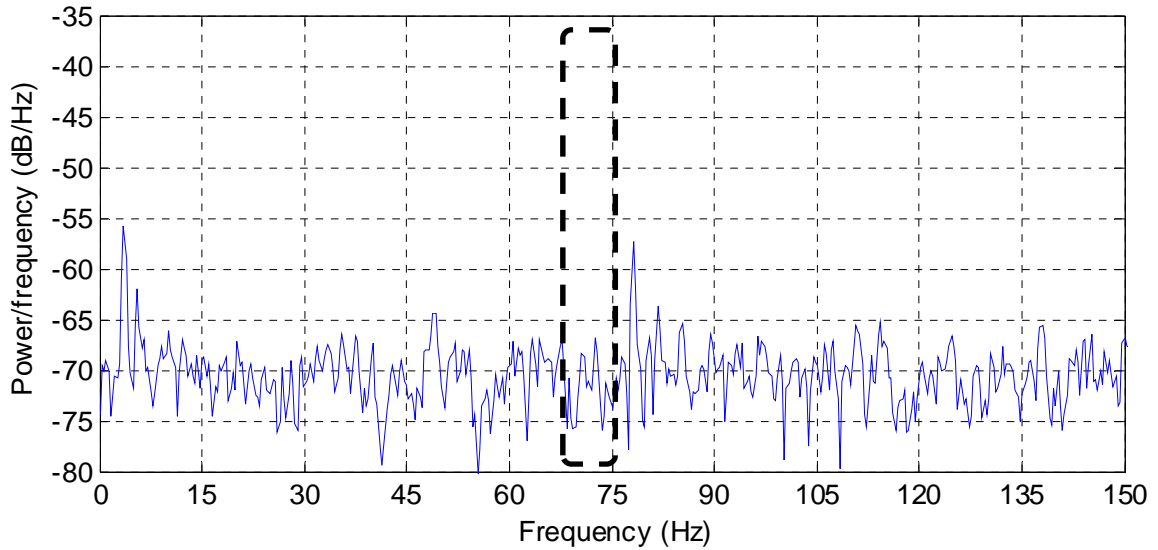


Figure 34 Frequency spectrum of raw signal from the faulty bearing at 1200 RPM

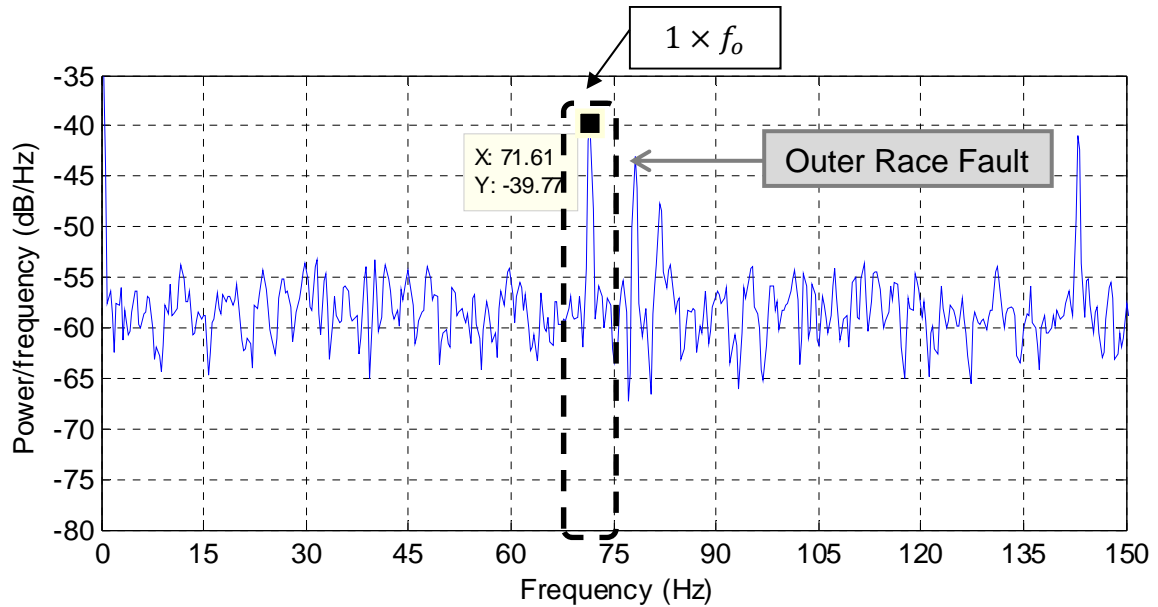


Figure 35 Frequency spectrum of denoised signal from the faulty bearing at 1200 RPM

The Figure 34 and Figure 35 are the frequency spectrum of the raw vibration signal and the denoised one, respectively. Dashed boxes are used to highlight the areas where BPFs may be present. It may look counter-intuitive to

find that no peaks appear in the highlighted area in Figure 34, which means the BPFO is not found in the spectrum of the raw signal. This is due to the amplitude modulation effect that covers the actual characteristic frequencies. After applying the envelope analysis and DTCWT-based denoising algorithm, we can see the BPFO appears on the spectrum of denoised signal in Figure 35.

As a comparison, the spectrum of the denoised signal from the normal bearing is also given in Figure 36. As expected, no peak appears near the highlighted area, which means no fault exists in the outer race of the bearing.

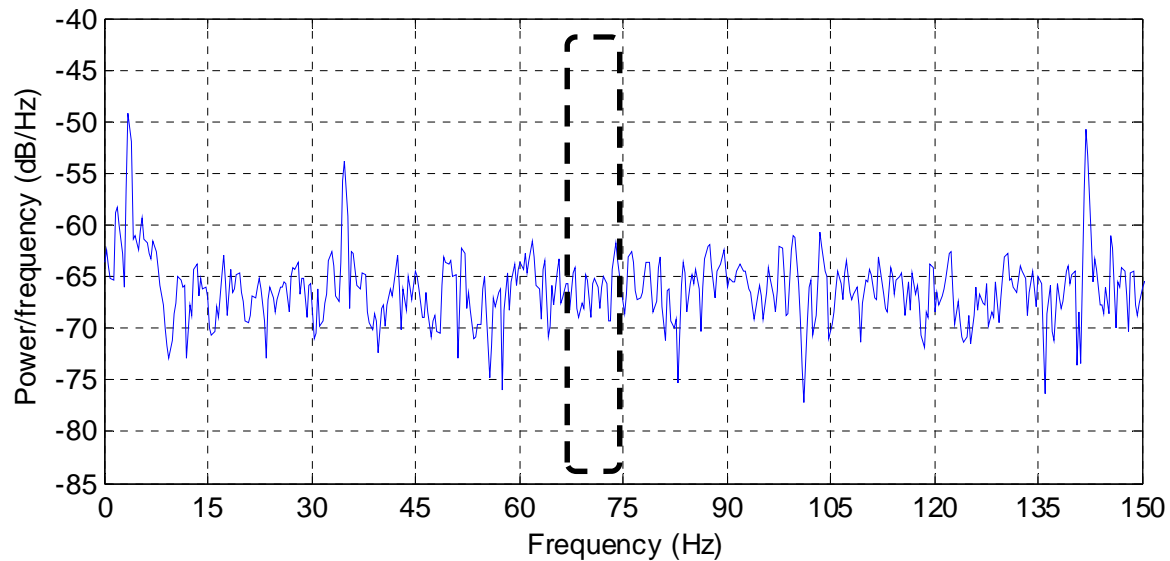


Figure 36 Frequency spectrum of denoised signal from the normal bearing at 1200 RPM

Table 4 compares the raw signal and the denoised signal using the kurtosis as a quantitative criterion. The kurtosis depicts how spiky the signal is. The kurtosis values listed in the table are the averaged kurtosis of ten repeated tests. As we can see, the kurtosis of the raw signal from the faulty bearing is

much larger than that from the normal bearing. The signal denoising further amplifies the kurtosis of the faulty bearing by about 8 times. The kurtosis of the denoised signal from the faulty bearing is about 50 times larger than that from the normal bearing, which clearly indicates the presence of machine fault.

Table 4 Kurtosis of signals from faulty and normal bearings at 1200 RPM

Signal source	Raw faulty	Raw normal	Denoised faulty	Denoised normal
Kurtosis Mean	23.12	2.63	176.46	3.31

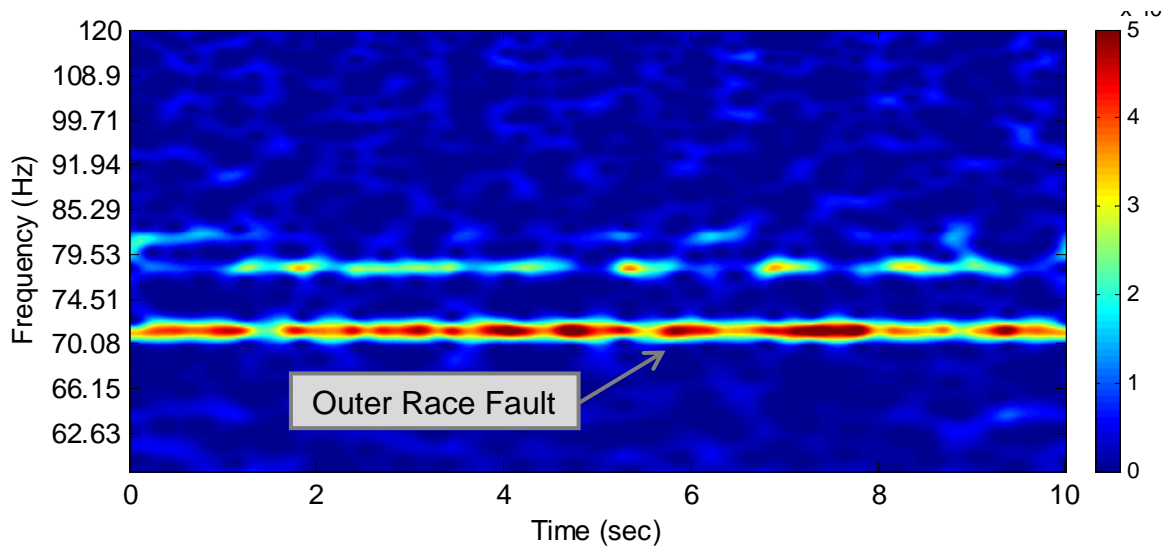


Figure 37 Scalogram of denoised signal from the faulty bearing at 1200 RPM

Another useful tool in visualizing bearing faults is the wavelet scalogram. A scalogram is the continuous time-frequency representation of the signal using colour to differentiate the magnitude of energy. In the presence of bearing faults, the corresponding high energy curves can be observed at BPFs in the scalogram.

In Figure 37, the marked horizontal line appears around 71.6 Hz, which perfectly matches the calculated BPFO. This clearly indicates the presence of faults in the outer race of the bearing.

4.1.2 Case 2: 2100 RPM

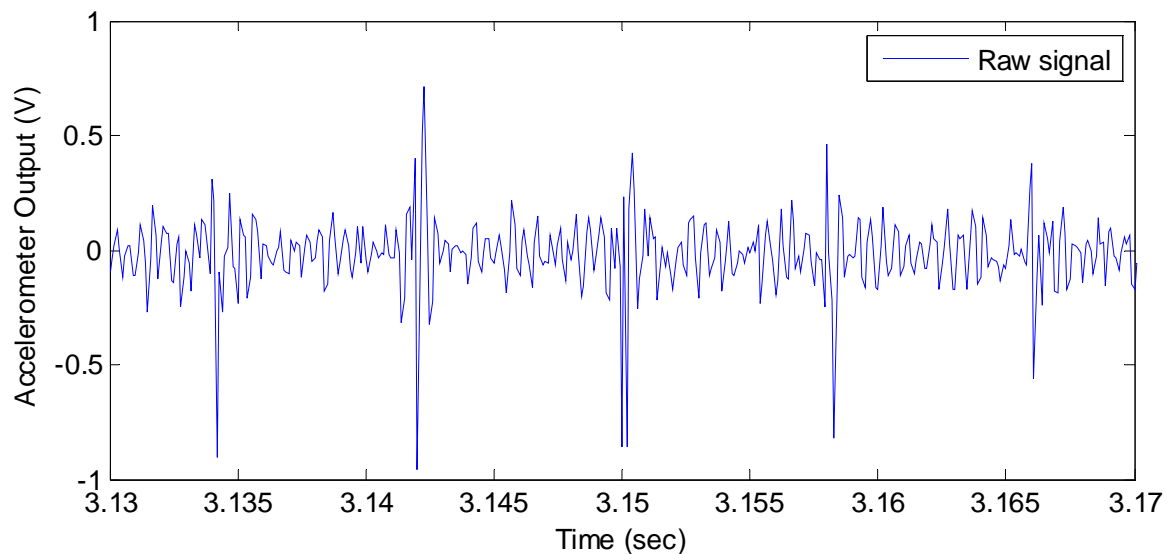


Figure 38 Partial enlarged vibration signal from the faulty bearing at 2100 RPM

This test was carried out using the same bearing and set up as the previous test, except for a higher rotating speed of the motor. The raw vibration signal shows evident impulses as well as noise. It is found that the amplitudes of these impulses are higher than that of the previous test. This is because under a higher rotating speed, larger amount of energy were generated by the defective area of the bearing.

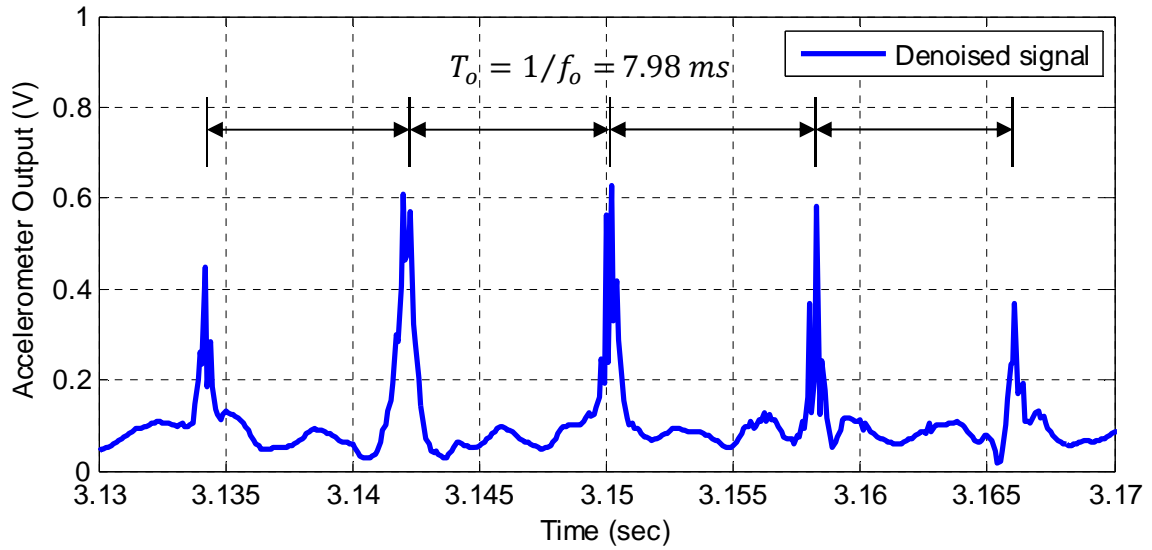


Figure 39 DTCWT-denoised signal from the faulty bearing at 2100 RPM

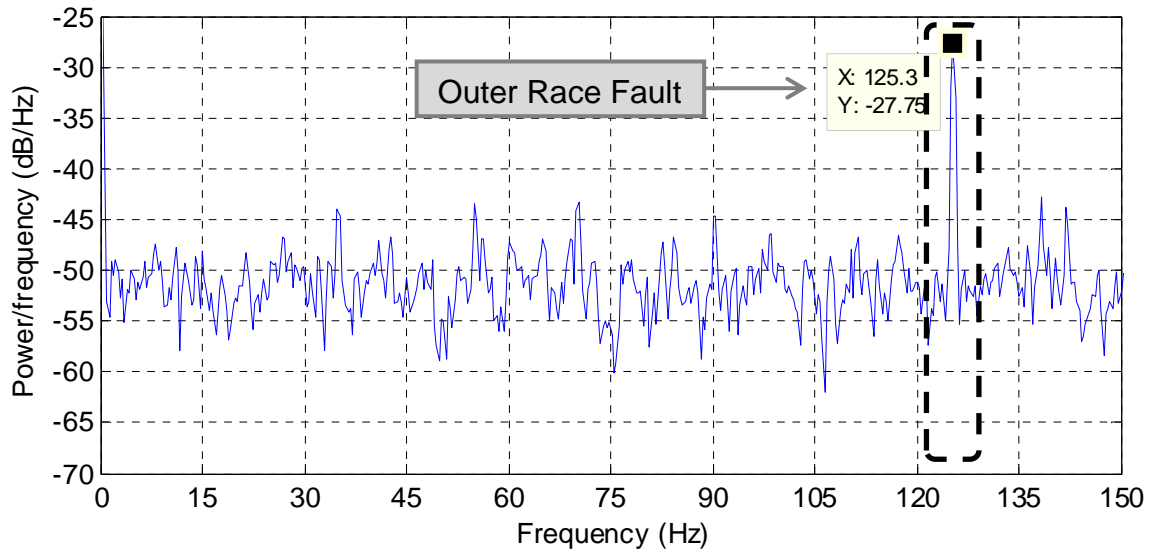


Figure 40 Frequency spectrum of denoised signal from the faulty bearing at 2100 RPM

Figure 39 shows the denoised vibration signal from the faulty bearing, where most of noise is removed while the characteristic impulses are preserved. The figure shows five peaks equally spaced with a time period of about 7.98 ms,

corresponding to 125.3 Hz. This matches with the calculated BPFO at 124.74 Hz. Thus, the result suggests an outer race fault in the test bearing.

Meanwhile, the periodic shocks produced by the faulty bearing can also be identified through the frequency spectrum. As shown in Figure 40, a distinct peak appears at 125.3 Hz, which is about 20 dB higher than the noise floor. This again suggests the fault on the outer race of the bearing.

In Table 5, the kurtosis of the faulty bearing is more than 40 times higher than that of a normal bearing, which clearly indicates the underlying machine fault.

Table 5 Kurtosis of signals from faulty and normal bearings at 2100 RPM

Signal source	Raw faulty	Raw normal	Denoised faulty	Denoised normal
Kurtosis Mean	34.58	2.86	142.37	3.51

Figure 41 shows the scalogram of the denoised signal from the faulty bearing. The marked line around 124 Hz matches the BPFO very well. Compared with Figure 37, the marked line in Figure 41 is more consecutive and the overall figure is much cleaner. This means the signature of bearing faults under higher motor speeds is more distinct.

Note that the second order harmonic of the BPFO also appears near the upper edge of Figure 41. It contains much less amount of energy compared with the first order harmonic. The appearance of higher order harmonics of the BPFO in

the spectrum is a typical phenomenon in envelope analysis, and can be regarded as an auxiliary indicator of bearing faults.

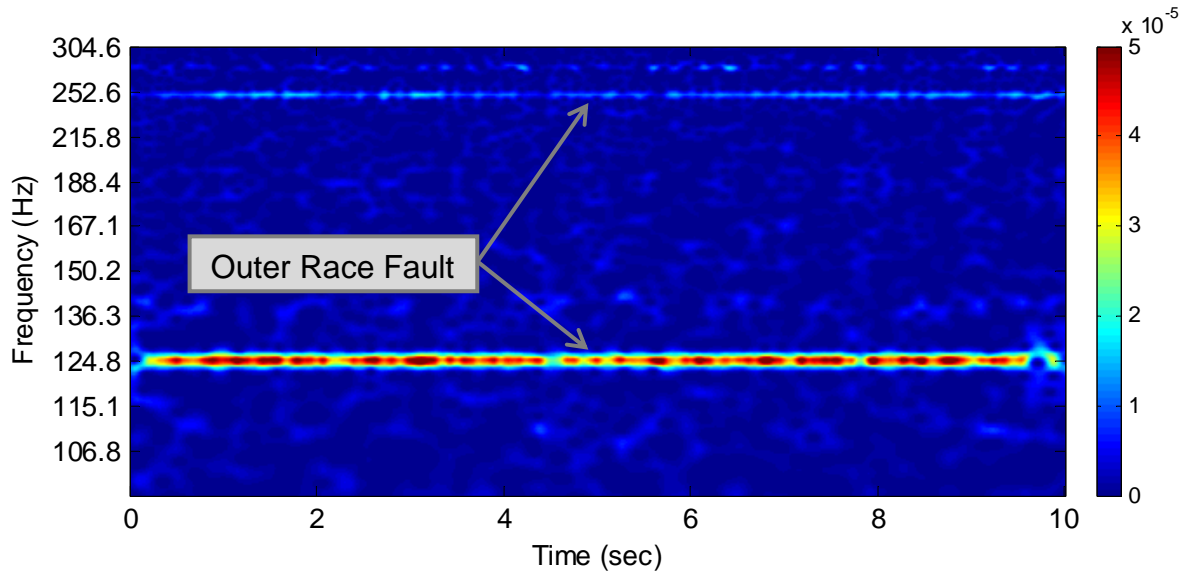


Figure 41 Scalogram of denoised signal from the faulty bearing at 2100 RPM

4.1.3 Case 3: Urban Driving Cycle

The Extra Urban Driving Cycle (EUDC) [100] is a driving cycle devised to represent typical driving conditions of a car. It is used frequently in the determination of emission levels of car engines and the assessment of average on-road fuel consumption. The prevalence of hybrid and electrical vehicles has drawn much attention to the condition monitoring of electric motors. So this test was designed in an attempt to demonstrate the effectiveness of the fault diagnosis scheme in practical situations.

In this test, the motor with the faulty bearing was driven following the speed trajectory of Figure 42. Since the machine under test was an electric motor rather than an engine, the Extra Urban Driving Cycle had been scaled accordingly. Figure 42 shows the actual speed measurement in the testing.

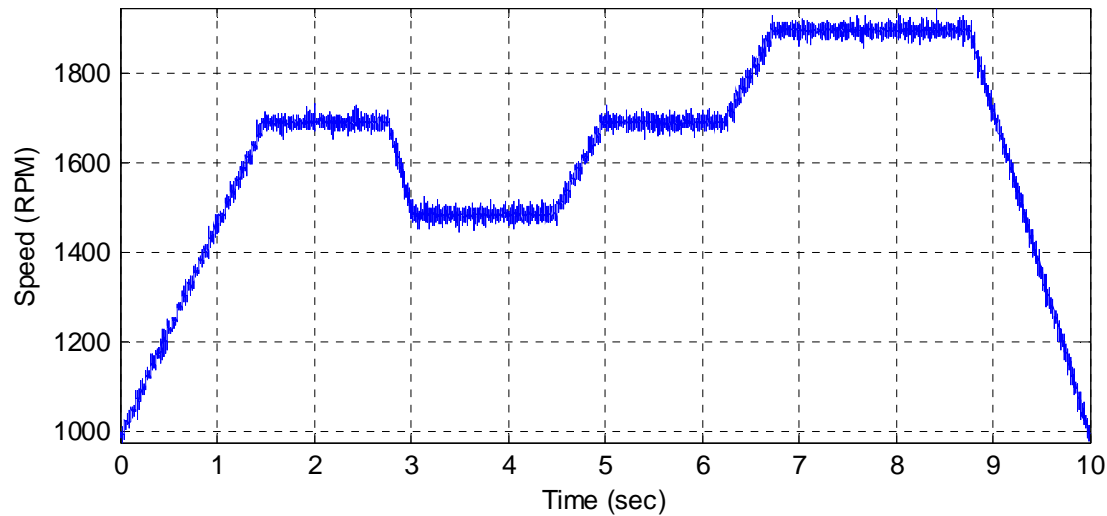


Figure 42 Measured motor speed in the Extra Urban Driving Cycle test

Figure 43 shows the BPFO corresponding to outer race fault of the bearing. Since the BPFO is proportional to the rotating speed of the motor, the trajectory in Figure 42 and Figure 43 are of the same shape. Figure 44 shows the wavelet scalogram of the denoised signal, where a trajectory is presented of the same shape with respect to Figure 43. This curve indicates the outer race fault of the bearing during the driving cycle test.

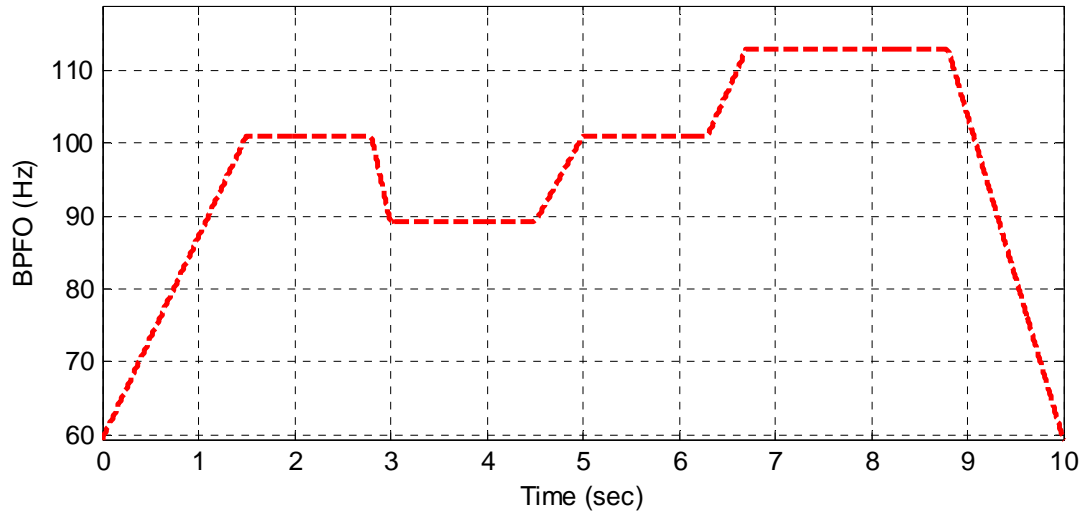


Figure 43 Ball Passing Frequency Outer Race (BPFO) in EUDC test

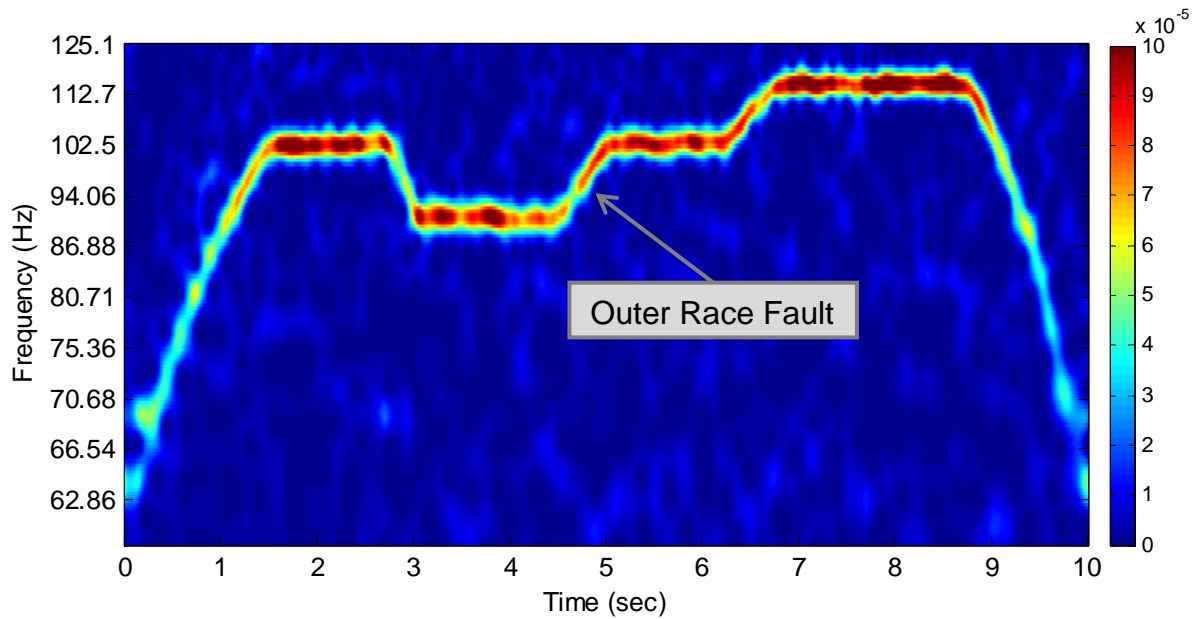


Figure 44 Scalogram of denoised signal from the faulty bearing in EUDC test

This example demonstrates the effectiveness of the diagnosis approach for bearing monitoring in practical applications, such as for hybrid vehicles.

4.2 Inner Race Fault

In an attempt to physically simulate the inner race fault, a small dent was created on the inner race of the bearing using electro-chemical etching method, as shown in Figure 45. When the rolling balls passed over the defective area, periodic shocks were produced. These shocks were then captured by vibration sensors for fault diagnosis. Details on experimental setup are provided in Appendix 1.

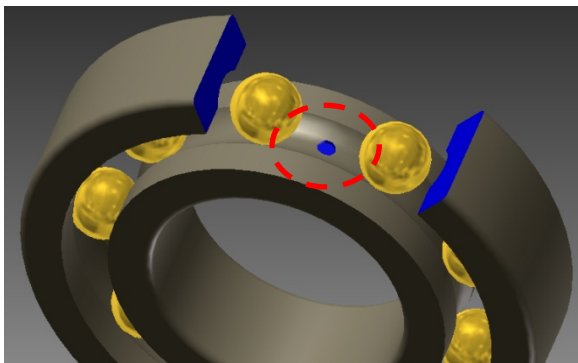


Figure 45 Inventor model of the test bearing with an inner race defect

4.2.1 Case 1: 1000 RPM

In this test, the faulty bearing in the test motor was replaced by another bearing of the same type, but with an inner race defect instead of the outer race defect. The inner race fault was physically simulated by creating a small dent on the inner race of the bearing. Figure 46 shows the measurement of raw vibration signal for 10 seconds.

Compared with the outer race fault, the characteristic impulses produced by the inner race fault are usually weaker. The reason relates to the structure of ball bearings. The outer race and the inner race are connected by rolling balls. The outer race fits into the bearing housing which connects to the sensor. Since the vibration is transmitted by the contact of rolling balls, part of the energy produced by impulses is damped during that transmission process. This results in weak fault signatures and makes the detection of inner race defect more difficult than that of the outer race defect.

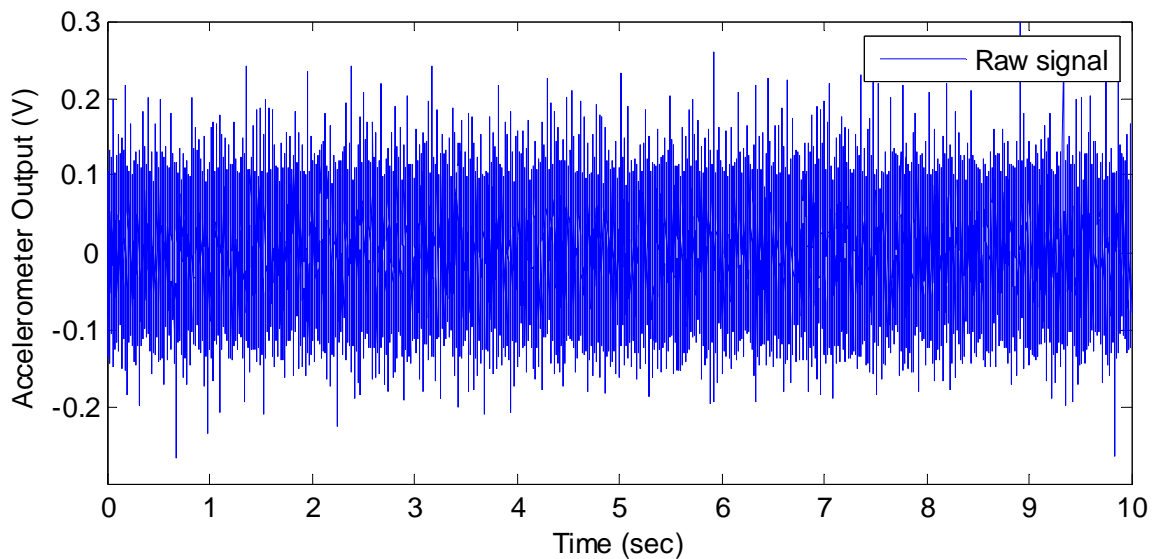


Figure 46 Raw vibration signal from the faulty bearing at 1000 RPM

In this case, the motor was running at the speed of 1000 RPM. The corresponding Ball Passing Frequency Inner Race (BPFI) was calculated according to Equation 2.2.1 as $f_i = 90.6 \text{ Hz}$. Figure 47 shows the spectrum of raw vibration signal. The dashed boxes are used to highlight the areas where the BPFI may appear.

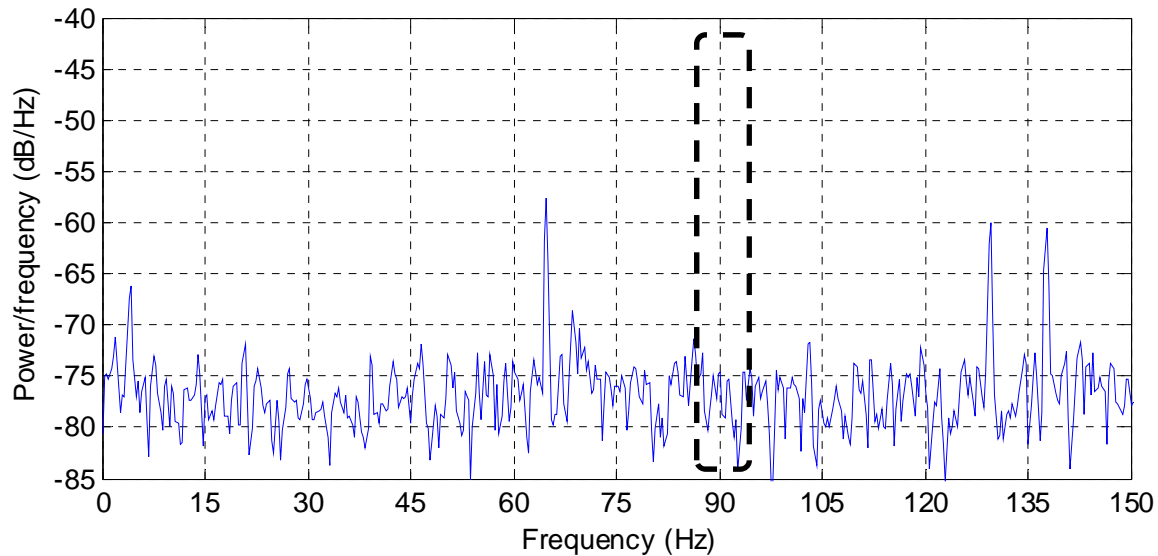


Figure 47 Frequency spectrum of raw signal from the faulty bearing at 1000 RPM

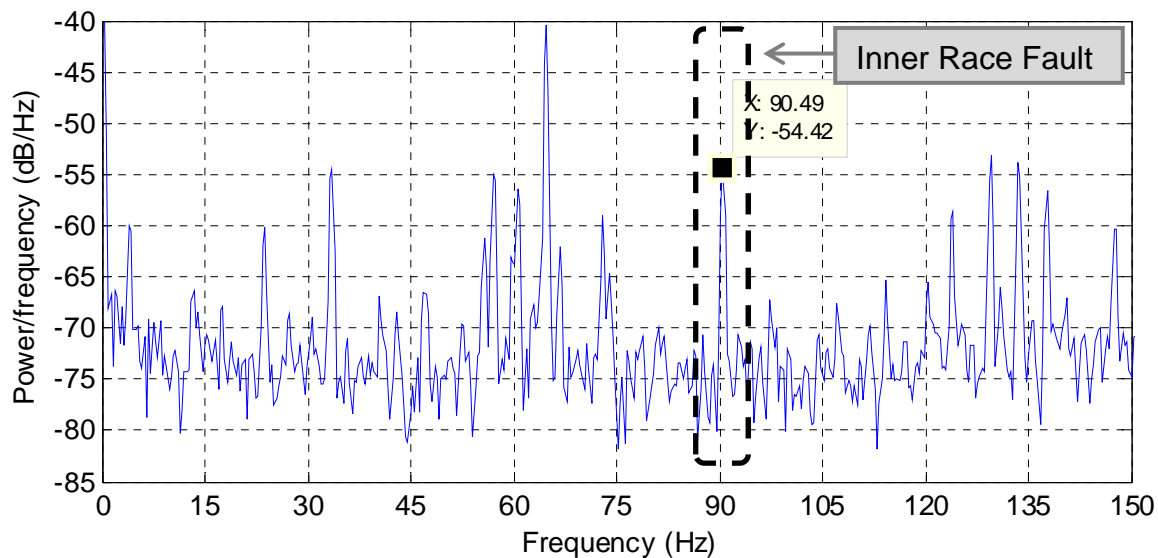


Figure 48 Frequency spectrum of denoised signal from the faulty bearing at 1000 RPM

The spectrum of raw vibration signal is shown in Figure 47, where no distinct frequency component appears within that highlighted area. This is due to the amplitude modulation effect that covers the characteristic frequencies of bearing faults.

After applying the signal denoising procedures, the resulting spectrum is shown in Figure 48. The frequency component of 90.49 Hz amongst a few other peaks is observed, which matches perfectly with the calculated BPFI at 90.6 Hz. The result thus proves the existence of an inner race fault in the bearing.

Besides, as shown in Figure 48, the inner race fault also excited a few other frequency components in the spectrum. These frequency components are not directly related to the bearing fault under investigation. Since a complete analysis of the vibration spectrum needs comprehensive knowledge of the whole system and is beyond the scope of this study, only those calculated within the expected fault frequency window were considered as indication of the specific fault conditions of this study.

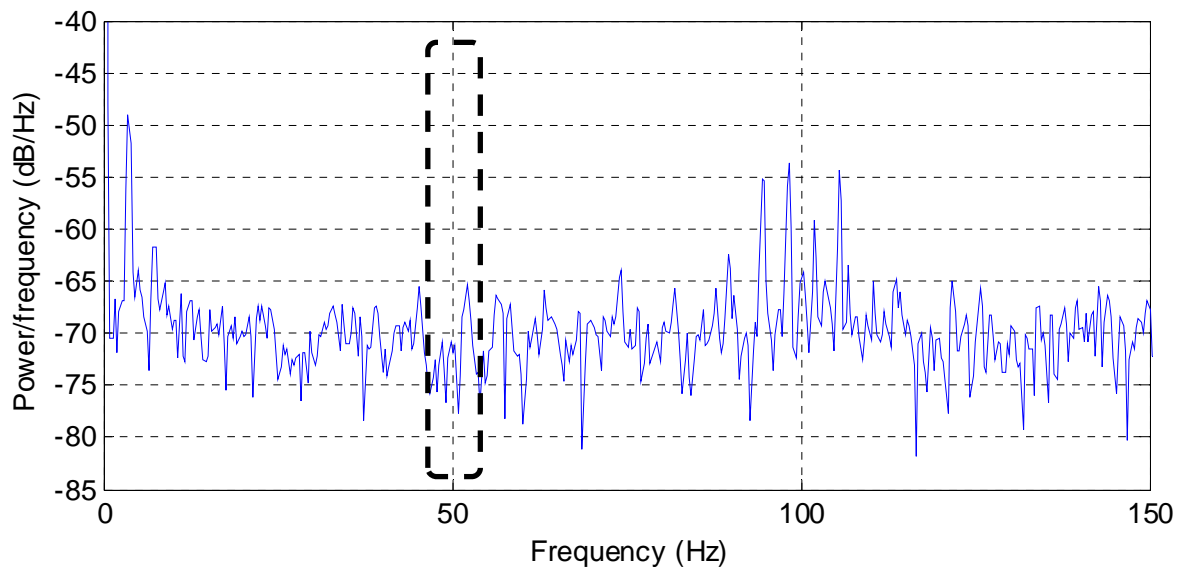


Figure 49 Frequency spectrum of raw signal from the normal bearing at 1000 RPM

In Table 6, the kurtosis of the signal from the faulty bearing is doubled after the denoising. In this case, the kurtosis does not reflect the bearing fault very well. This is due to the presence of multiple harmonics and weak signature of the inner race fault.

Table 6 Kurtosis of signals from faulty and normal bearings at 1000 RPM

Signal source	Raw faulty	Raw normal	Denoised faulty	Denoised normal
Kurtosis Mean	3.38	2.75	6.82	3.37

Figure 50 shows the wavelet scalogram, which clearly shows the BPFI. It can be seen that there is also more noise present in the scalogram, compared to Figure 41.

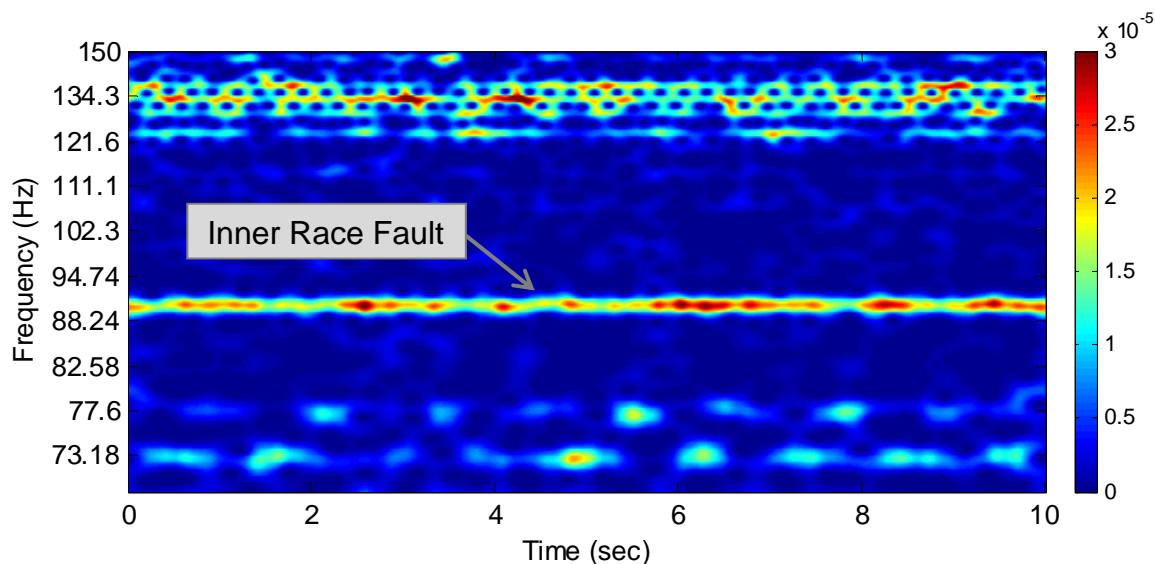


Figure 50 Scalogram of denoised signal from the faulty bearing at 1000 RPM

4.2.2 Case 2: 2800 RPM

This test was carried out using the same bearing and set up as the previous test, except for a higher motor speed of 2800 RPM.

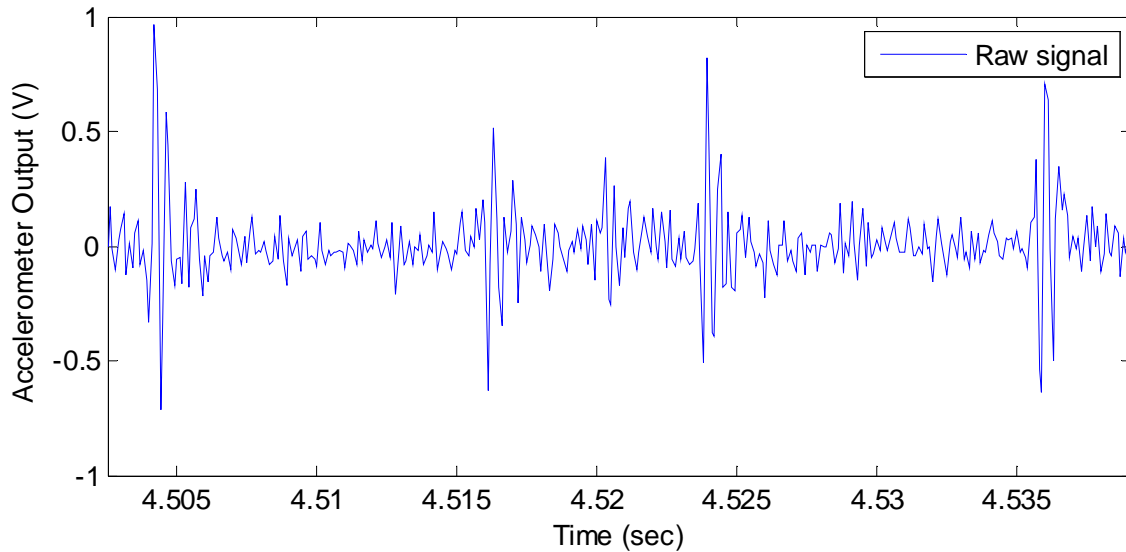


Figure 51 Partial enlarged signal from the faulty bearing at 2800 RPM

A partially enlarged plot of the raw vibration signal is shown in Figure 51. Apparently, the signal consists of a lot of frequency components and noise. The denoised signal shown in Figure 52 is much cleaner than the original one. The period of the impulses is approximately 3.94 ms, corresponding to 253.9 Hz. This perfectly matches with the BPFI at 253.7 Hz. Thus the results clearly indicate the inner race fault of the bearing.

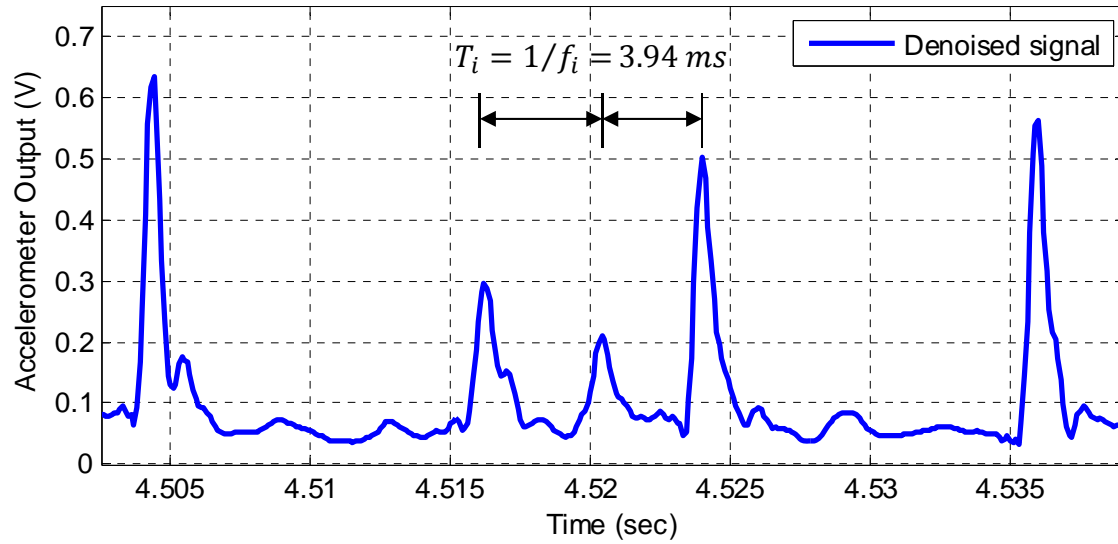


Figure 52 DTCWT-denoised signal from the faulty bearing at 1200 RPM

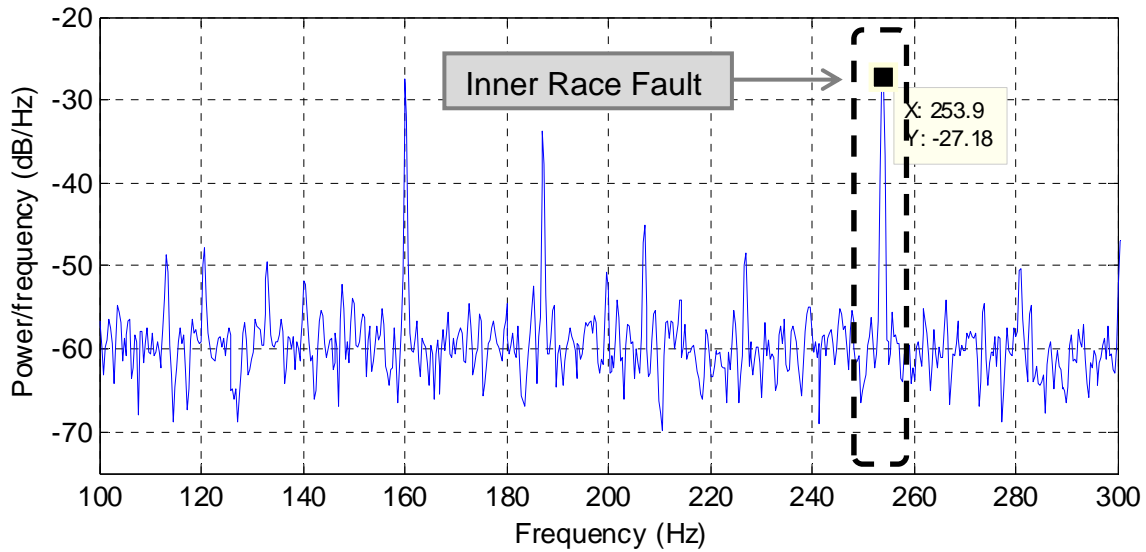


Figure 53 Frequency spectrum of denoised signal from the faulty bearing at 2800 RPM

The BPFI is also clearly shown in the frequency spectrum, as illustrated by the highlighted area of Figure 53. In Figure 54, the distinct horizontal line around 253 Hz further confirms the presence of the inner race fault.

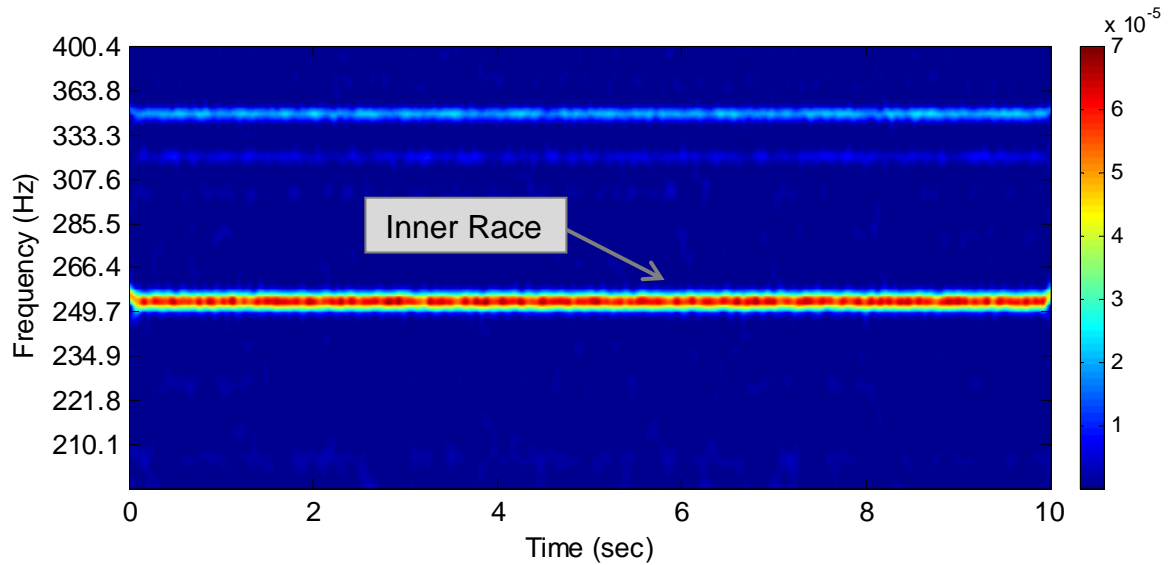


Figure 54 Scalogram of denoised signal from the faulty bearing at 2800 RPM

Table 7 Kurtosis of signals from faulty and normal bearings at 2800 RPM

Signal source	Raw faulty	Raw normal	Denoised faulty	Denoised normal
Kurtosis Mean	16.10	2.77	22.39	3.24

In Table 7, the kurtosis of the denoised signal from the faulty bearing is about 7 times larger than that of a normal bearing. The difference reveals the abnormal operating condition of the motor. Moreover, the figures also demonstrate the effectiveness of the denoising algorithm in enhancing the characteristic features of the fault.

4.2.3 Case 3: Urban Driving Cycle

The Extra Urban Driving Cycle (EUDC) [100] is a driving cycle devised to represent typical driving conditions of a car. As described in Section 4.1.3, this test was designed in an attempt to demonstrate the effectiveness of the fault diagnosis scheme in practical situations. Since the machine under test was an electric motor rather than an engine, the Extra Urban Driving Cycle had been scaled accordingly. Figure 55 shows the measured speed trajectory in the testing.

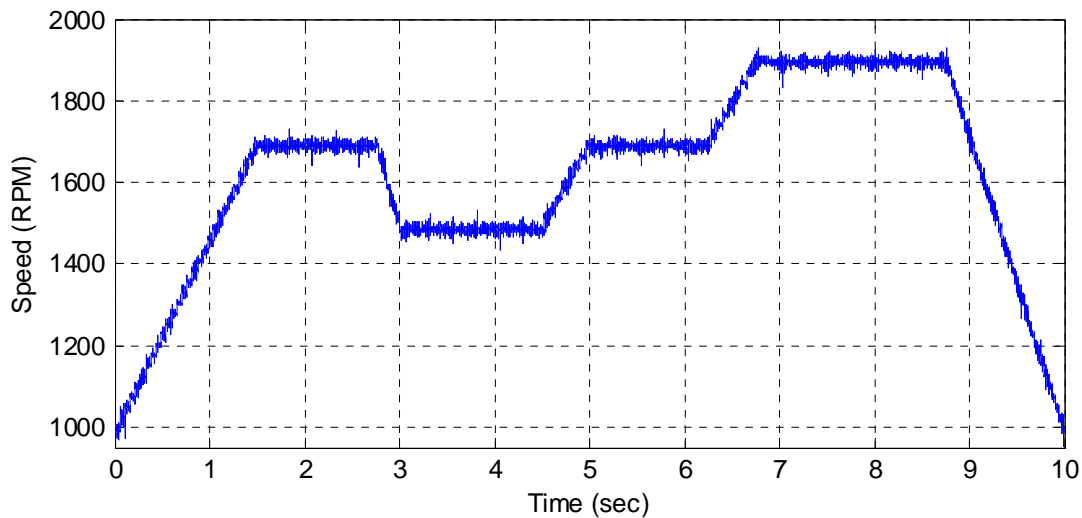


Figure 55 Measured motor speed in the Extra Urban Driving Cycle test (same as Figure 40)

Figure 43 shows the BPFO corresponding to inner race fault of the bearing. Since the BPFO is proportional to the rotating speed of the motor, the curve in Figure 42 and Figure 43 are of the same shape. Figure 44 shows the wavelet scalogram of the denoised signal, where a trajectory is presented of the same shape with respect to Figure 43. This curve indicates the inner race fault of the bearing during the driving cycle test.

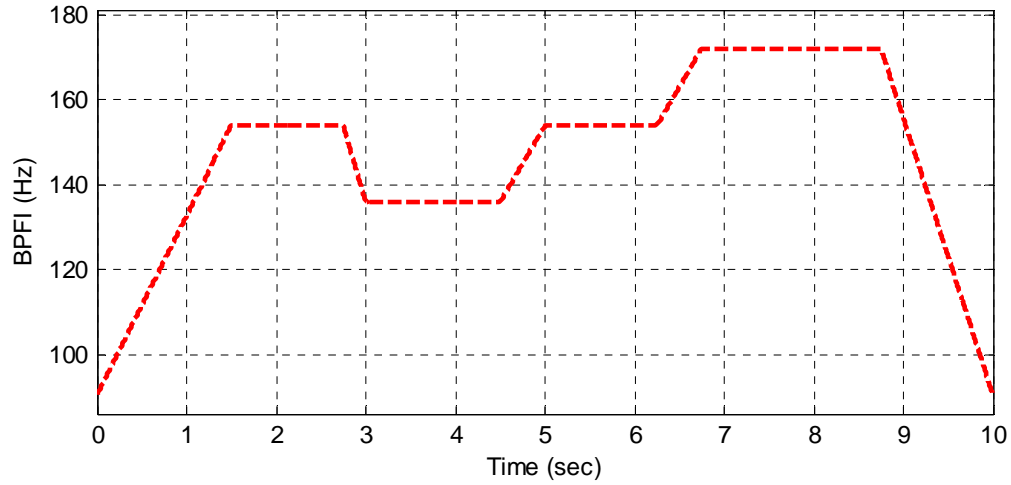


Figure 56 Ball Passing Frequency Inner Race (BPFI) in EUDC test

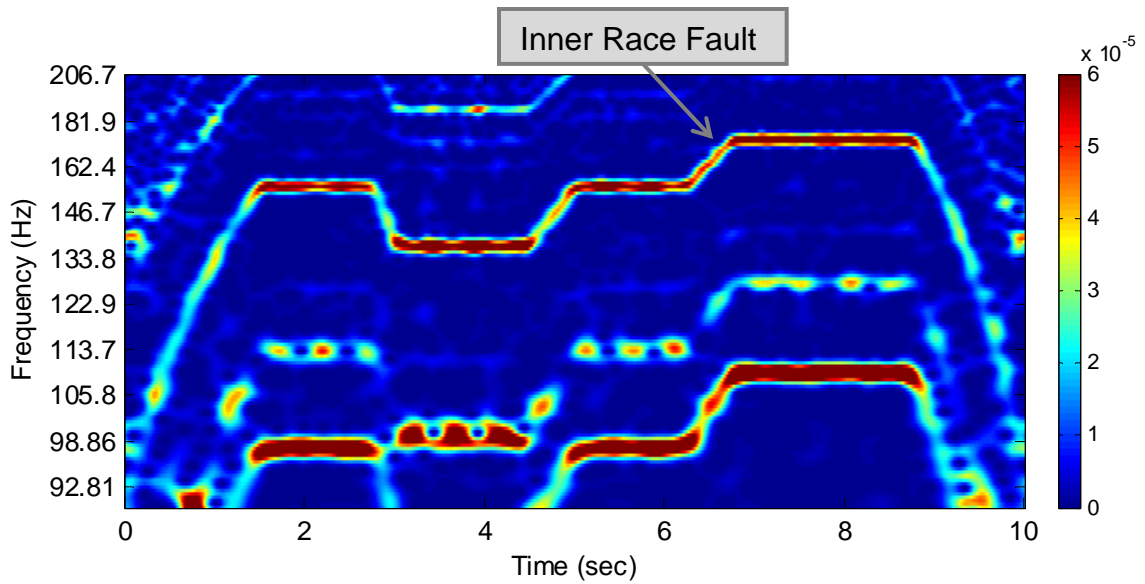


Figure 57 Scalogram of denoised signal from the faulty bearing in EUDC test

This example demonstrates the effectiveness of the diagnosis approach for bearing monitoring in practical applications, such as for hybrid vehicles.

4.3 Multiple Faults

In an attempt to physically simulate the multiple faults condition, a small dent was created on both of the inner and outer races of the bearing using electro-chemical etching method, as shown in Figure 45. When the rolling balls pass over the defective area, periodic shocks would be produced. These shocks were then captured by vibration sensors for fault diagnosis. Details on experimental setup are provided in Appendix 1.

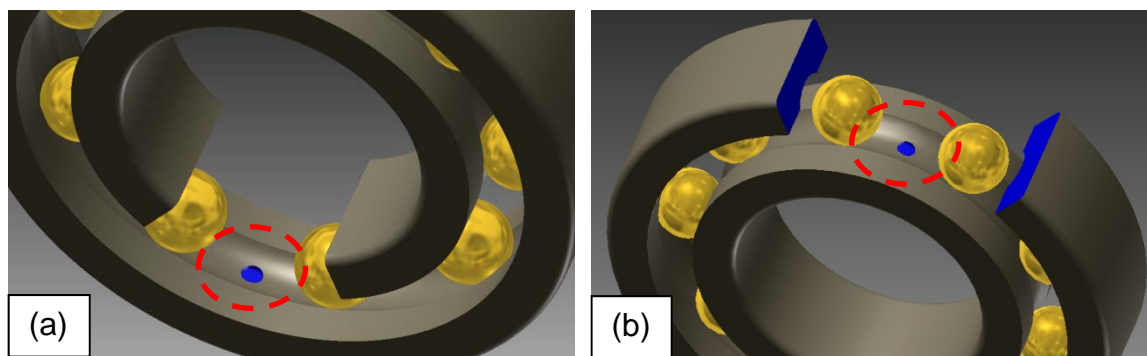


Figure 58 Inventor model of the test bearing with multiple defects: (a) Outer race defect; (b) Inner race defect

4.3.1 Case 1: RPM = 1500

In this case, the motor was running at the speed of 1500 RPM. The corresponding BPFO and BPFI are 89.1 Hz and 135.9 Hz, respectively. Figure 59 shows the raw vibration signal in the time-domain. Figure 60 is the partially enlarged view of Figure 59, where some characteristic impulses are presented. In

multiple faults diagnosis, the mixture of impulses at different frequencies increases the difficulty of signal denoising and fault diagnosis.

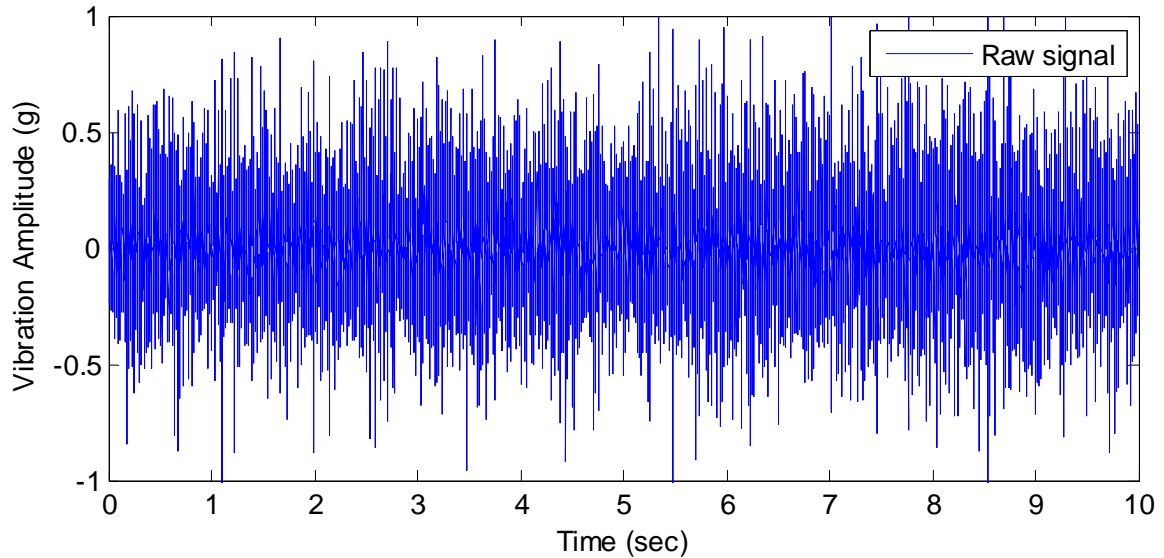


Figure 59 Raw vibration signal from the bearing with multiple faults at 1500 RPM

As shown in Figure 61, the denoised signal is much cleaner compared to the raw signal shown in Figure 60. Also, the characteristic impulses are well preserved. As marked in Figure 61, two sets of harmonics can be observed. Those impulses with larger amplitude have a period of 11.17 ms, corresponding to 89.5 Hz. That matches with the BPFO at 89.1 Hz and thus indicates the outer race defect. The impulses with smaller amplitude have a period of 7.4 ms, corresponding to 135.1 Hz. It matches the BPFI at 135.9 Hz and thus suggests the inner race defect. Besides, the impulses produced by the inner race defect suffered more damping effect than those by the outer race defect.

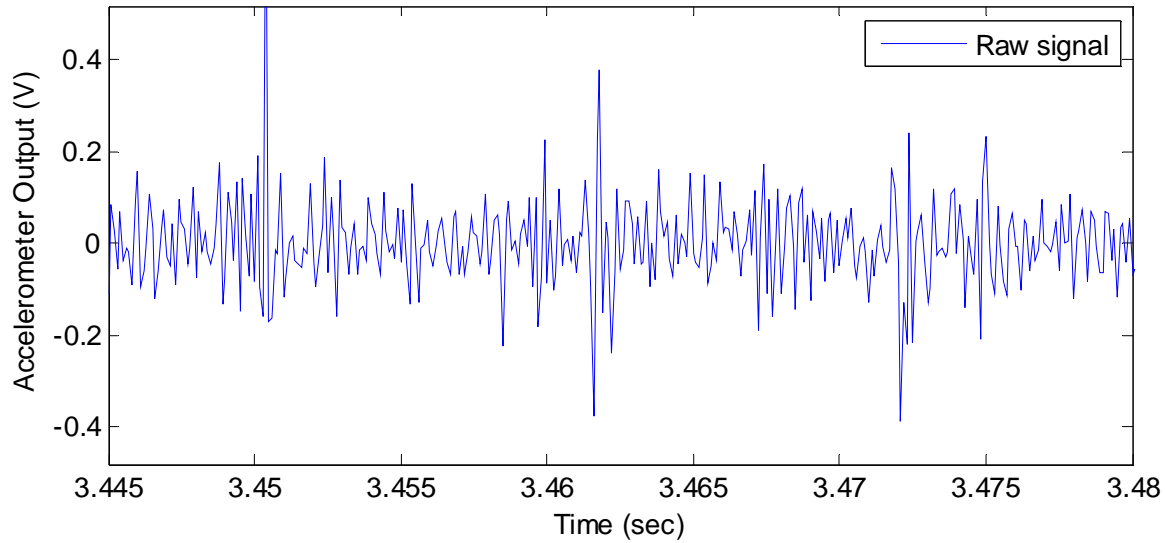


Figure 60 Partial enlarged signal from the bearing with multiple faults at 1500 RPM

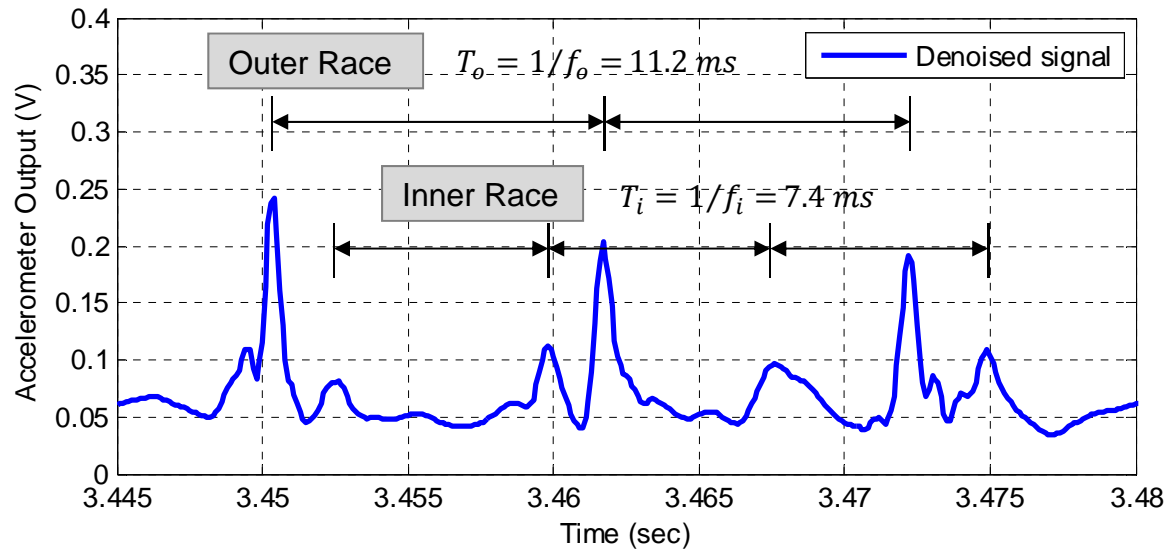


Figure 61 DTCWT-denoised signal from the bearing with multiple faults at 1500 RPM

Figure 62 and Figure 63 show the spectrum of the raw signal and the denoised signal respectively. In Figure 63, the denoised spectrum shows two frequency components at the characteristic frequencies, which clearly indicates the presence of both inner race (89.5 Hz) and outer race (135.7 Hz) fault. It also

shows the second order harmonic of the BPFO at 179 Hz, which further confirms the presence of the outer race fault.

Figure 64 shows the scalogram of the denoised signal, where the area representing the inner and outer race faults are marked. It can be seen from the figure that the impulses produced by the inner race fault is intermittent and contains much less energy compared to that of the outer race defect. In addition, compared with signal fault cases, the presence of two faults greatly increases the harmonics and noise in the signal.

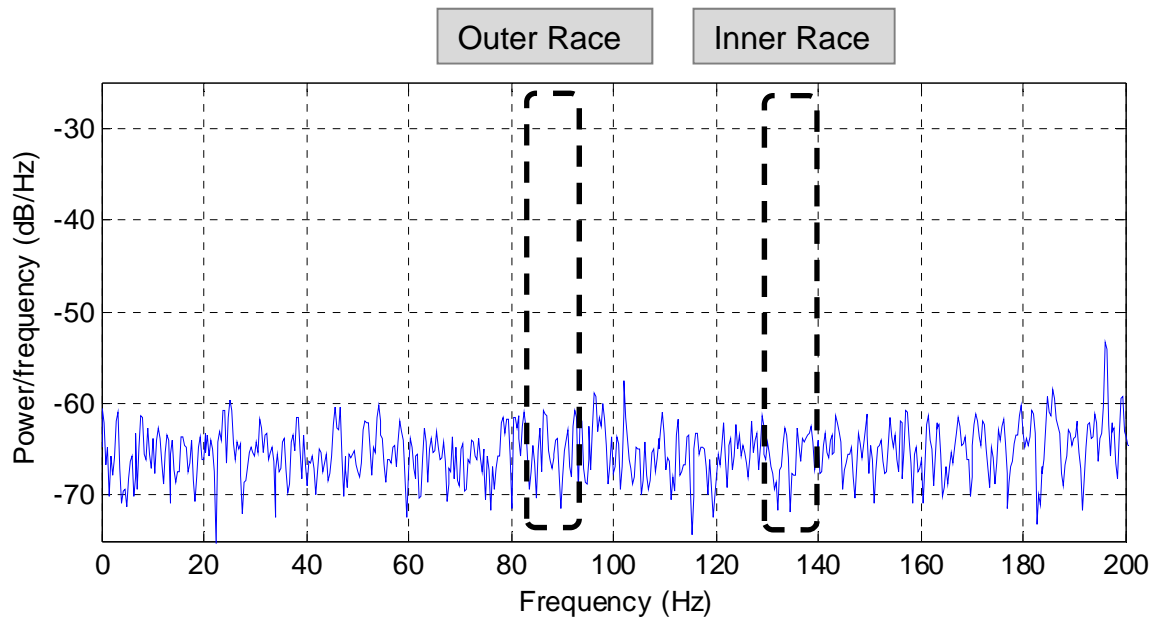


Figure 62 Frequency spectrum of raw signal from the bearing with multiple faults at 1500 RPM

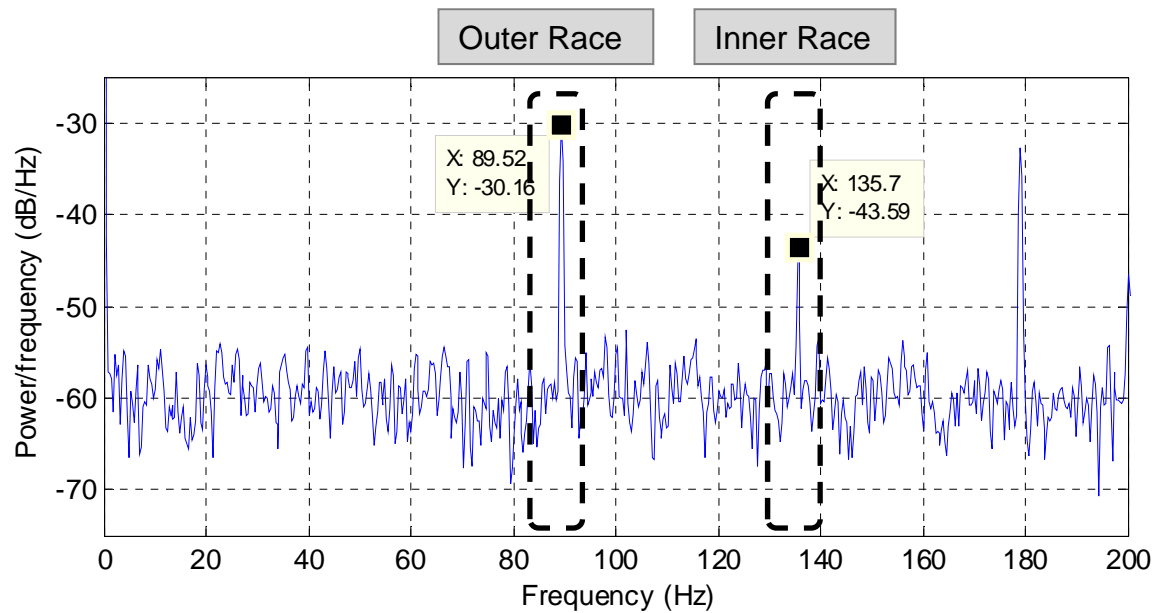


Figure 63 Frequency spectrum of denoised signal from the bearing with multiple faults at 1500 RPM

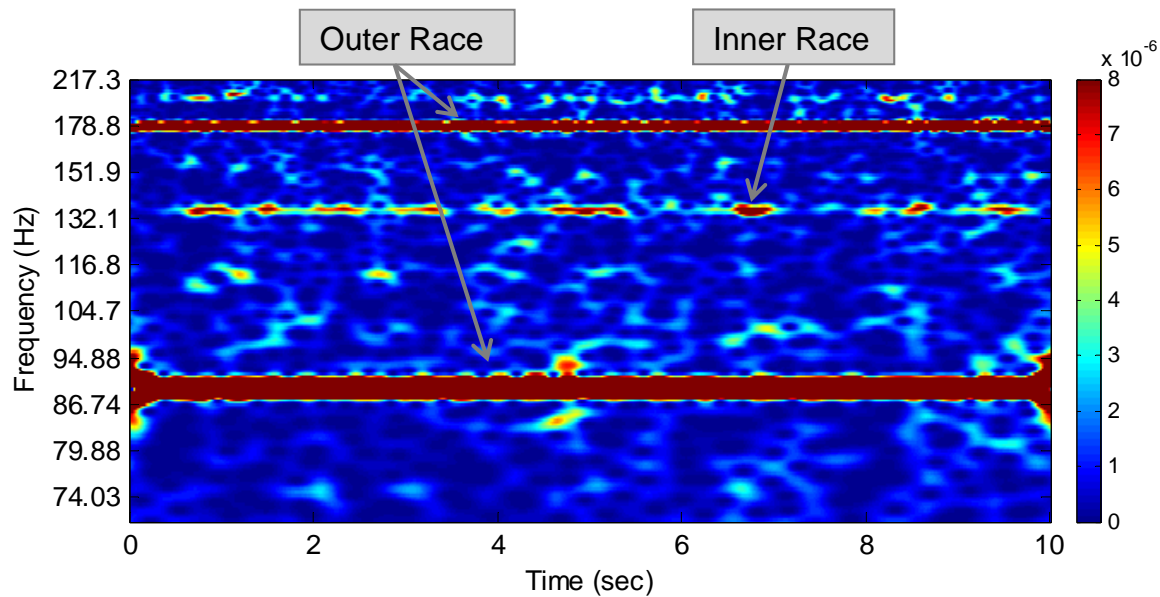


Figure 64 Scalogram of denoised signal from the bearing with multiple faults at 1500 RPM

Table 8 Kurtosis of signals from faulty and normal bearings at 1500 RPM

Signal source	Raw faulty	Raw normal	Denoised faulty	Denoised normal
Kurtosis Mean	12.36	2.69	59.48	3.05

In Table 8, the kurtosis of the denoised signal from the faulty bearing is about 20 times larger than that from the normal bearing, which suggests the presence of machine faults. It is also found that the combination of two faults at the same bearing does not give a larger kurtosis than a signal bearing a single fault would.

4.3.2 Case 2: RPM = 2500

In this test, the motor was running at the speed of 2500 RPM. The faulty bearing was the same as the one used in the previous case, with both an inner race fault and an outer race fault. Figure 65 gives an example of the raw signal in time-domain. In Figure 66, the denoised signal is much cleaner and it depicts two distinct patterns. The time periods of these two sets of impulses are 4.42 ms and 6.69 ms, corresponding to 226.2 Hz and 149.4 Hz, respectively. These frequencies perfectly match with the calculated BPFO at 148.5 Hz and BPFI at 226.5 Hz.

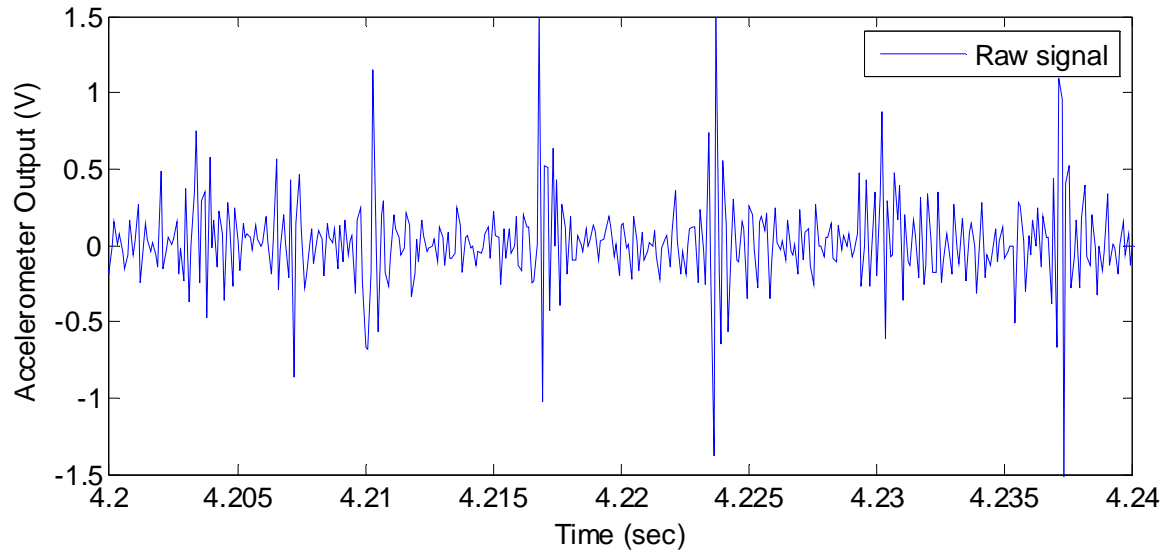


Figure 65 Partial enlarged vibration signal from the bearing with multiple faults at 2500 RPM

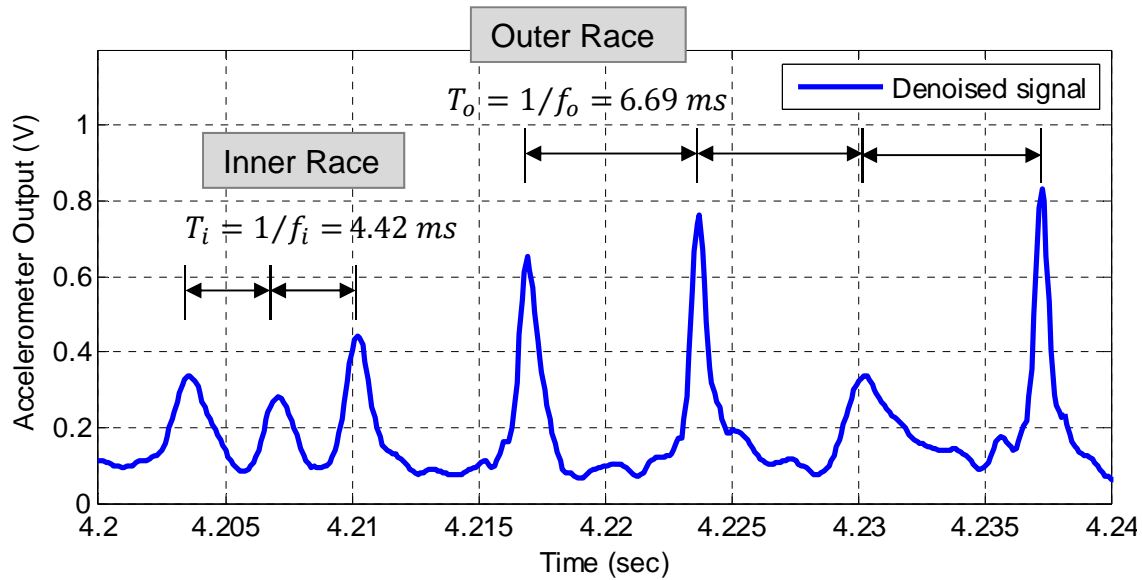


Figure 66 DTCWT-denoised signal from the bearing with multiple faults at 2500 RPM

Figure 67 shows the frequency spectrum of the denoised signal. Apparently, the BPFO and BPFI representing the outer race and the inner race faults, respectively, are present in the frequency spectrum.

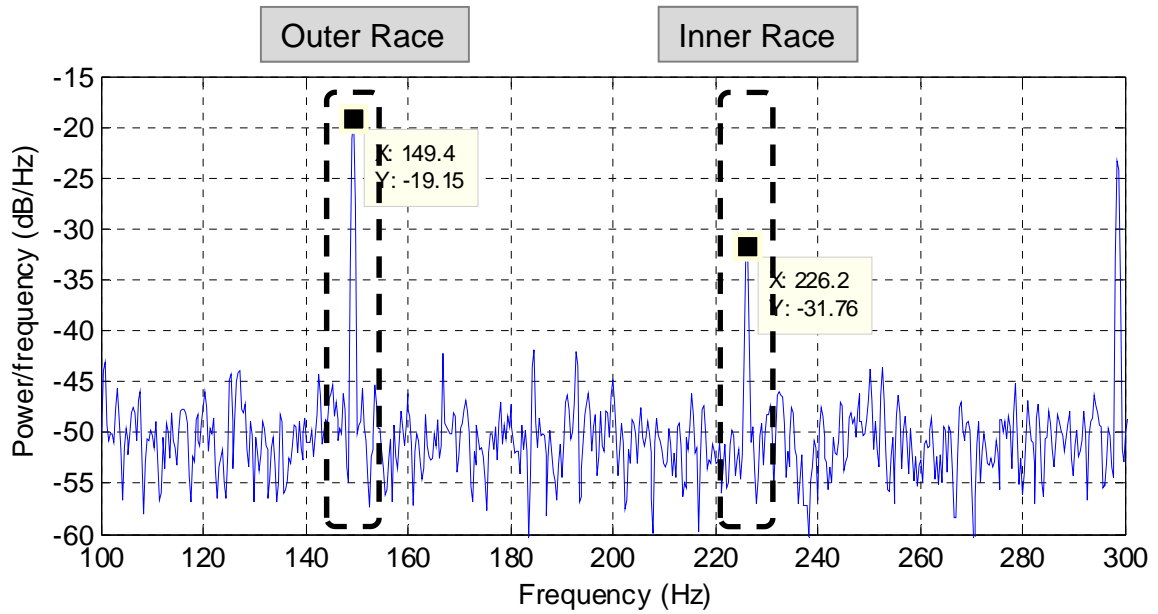


Figure 67 Frequency spectrum of denoised signal from the bearing with multiple faults at 2500 RPM

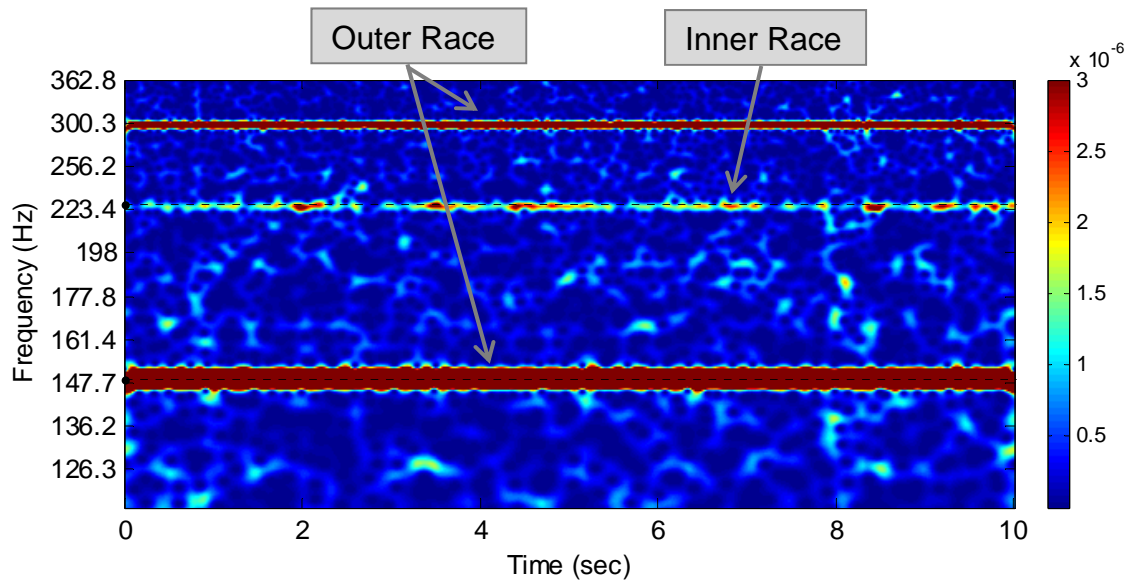


Figure 68 Scalogram of denoised signal from the bearing with multiple faults at 2500 RPM

In Figure 68, the wavelet scalogram also clearly shows the inner and the outer race faults. Both the first and the second harmonics of the BPFO are

present. Due to the damping effect, the fault signature of the inner race defect is not as strong as that of the outer race defect.

Table 9 Kurtosis of signals from faulty and normal bearings at 2500 RPM

Signal source	Raw faulty	Raw normal	Denoised faulty	Denoised normal
Kurtosis Mean	11.47	2.78	29.73	3.51

In Table 9, the kurtosis of the denoised signal from the faulty bearing is more than 8 times larger than that from a normal bearing, which suggests the underlying machine faults. The effectiveness of DTCWT in enhancing characteristic features of faults is also reflected by the increase of the kurtosis from 11.47 to 29.73.

4.3.3 Case 3: Urban Driving Cycle

The Extra Urban Driving Cycle (EUDC) [100] is a driving cycle devised to represent typical driving conditions of a car. As described in Section 5.1.2.3, this test was designed in an attempt to demonstrate the effectiveness of the fault diagnosis scheme in practical situations. Figure 69 shows the measured speed trajectory in the testing. Figure 70 shows the BPFO and BPFI corresponding to outer and inner race faults respectively. Since the BPFs are proportional to the

rotating speed of the motor, the curves shown in Figure 69 and Figure 70 are of the similar shape.

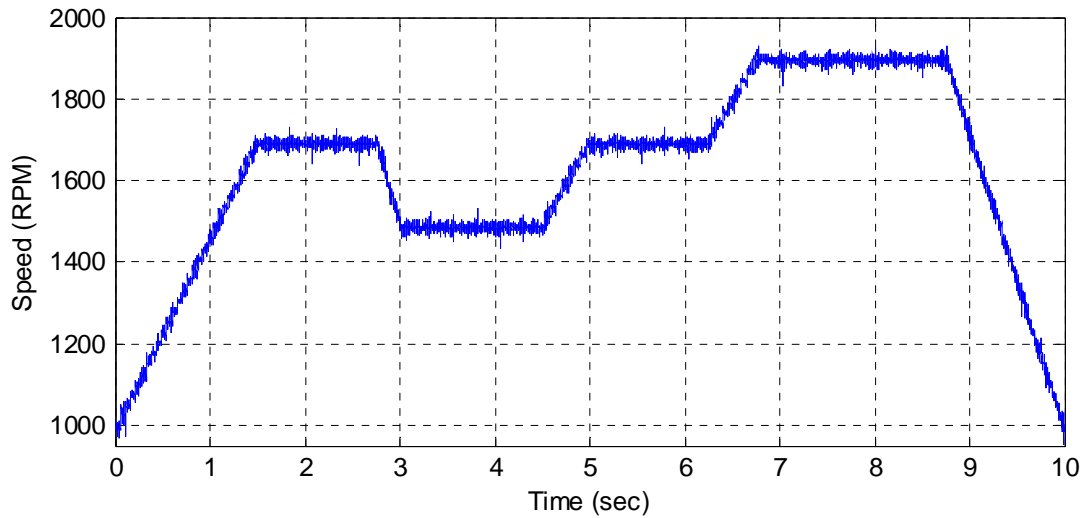


Figure 69 Measured motor speed in the Extra Urban Driving Cycle test (same as Figure 40)

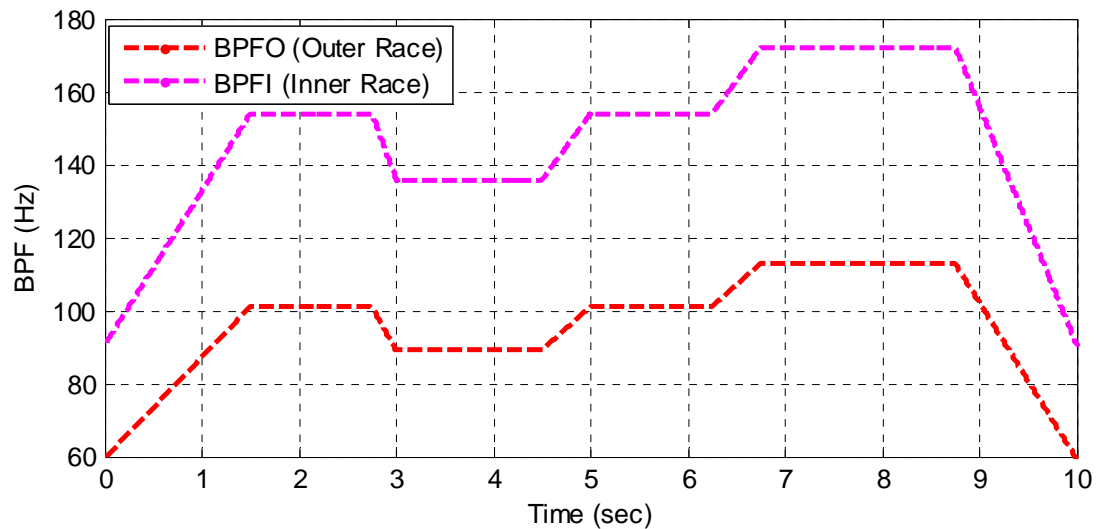


Figure 70 Ball Passing Frequencies (BPFO and BPFI) in EUDC test

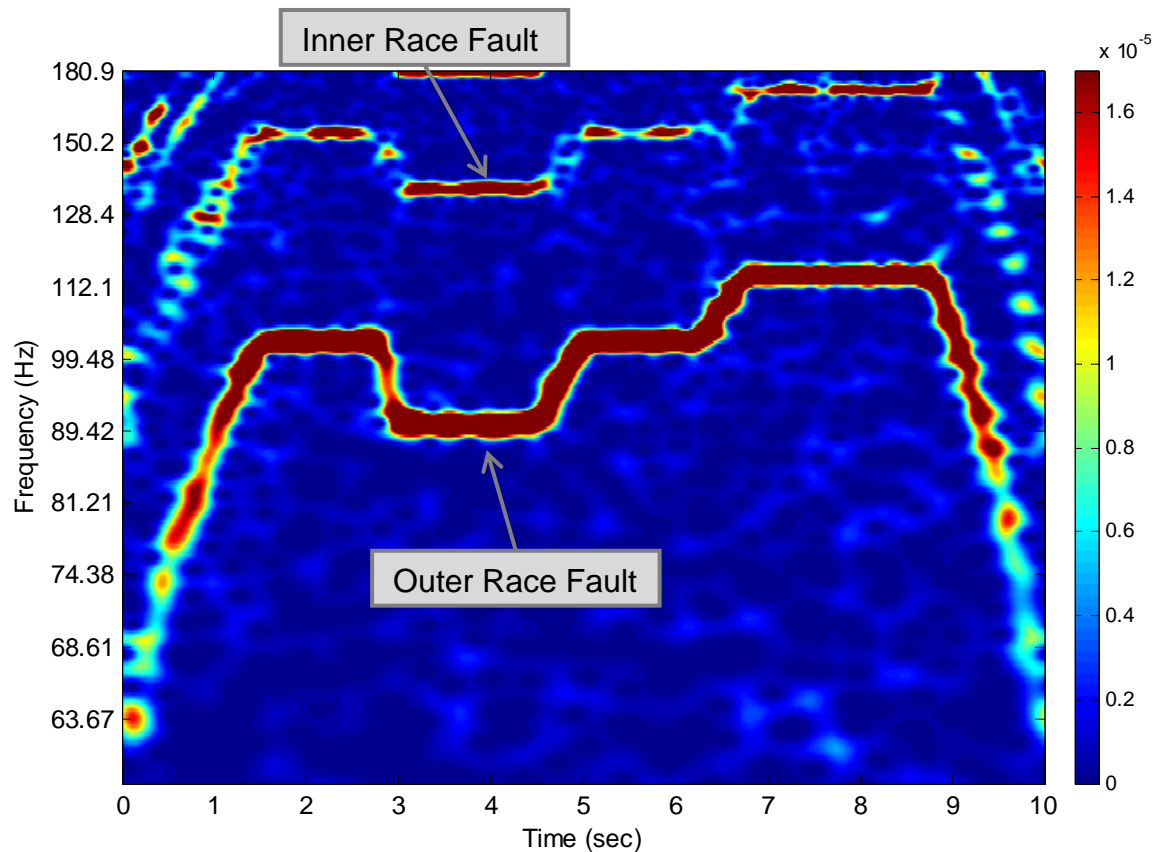


Figure 71 Scalogram of denoised signal from the faulty bearing in EUDC test

Figure 71 shows the wavelet scalogram of the denoised signal. Two curves present in Figure 71, which indicate the inner race fault and the outer race fault respectively. The fault signature of the outer race defect is much stronger than that of the inner race defect. The curves shown in Figure 71 appear not exactly as the BPF curves shown in Figure 70. This is because the wavelet scalogram shown in Figure 71 has varying frequency resolution (y-axis).

4.4 Summary

This section provided the experimental results and discussions of the fault diagnosis conducted on the BLDC motor. The denoising algorithm, which incorporates the Dual-Tree Complex Wavelet Transform with Bivariate shrinkage played a central role in the denoising and feature enhancement of the measured signal. During the tests, the front bearing in the test motor was replaced by a faulty one. Four conditions were considered, namely normal bearing, bearing with inner race defect, bearing with outer race defect, and bearing with multiple defects. In each group of defect, two motor speeds were selected and the results were compared. By applying the DTCWT-based algorithms on vibration measurements, the bearing faults were detected successfully and repeatedly. Meanwhile, it was found that fault could be diagnosed and identified under varying speeds conditions, such as the EUDC driving cycle. The results also suggested that higher rotating speed would produce stronger characteristic features for fault diagnosis. All of the results presented in this chapter demonstrate the effectiveness of the proposed approach in fault detection and diagnosis of rolling bearings.

Chapter 5 Estimation Theory

State estimation is an important concept in control and instrumentation. In mechanical or electrical systems, the internal dynamics are usually described by a set of state variables. The goal of state estimation is to extract the states from available measurements, which are usually noisy. Accurate estimation of the states plays a key role in control systems. For example, in order to control the speed and the position of a motor, the controller may need to estimate the winding currents and the winding resistances of the motor. This can be achieved by using state and parameter estimation algorithms. In this chapter, one of the most well-known estimation methods, the *Kalman Filter*, is briefly introduced. The *Smooth Variable Structure Filter* is also considered [101].

5.1 The Kalman Filter

The *Kalman Filter* was first published by R.E. Kalman in 1960 in his famous paper that described a recursive solution to the discrete linear filtering problem [102]. Since then, the *Kalman Filter* has become the best used filter for estimation and has been the subject of extensive research [102-116]. One of the applications that made it famous was its use in NASA lunar and Apollo missions [117].

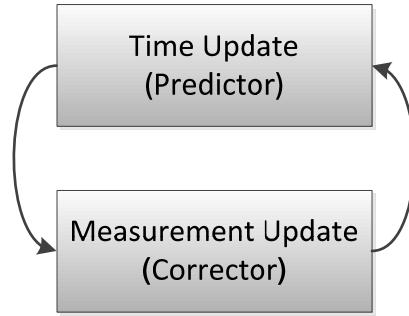


Figure 72 The discrete Kalman Filter cycle

Basically, the *Kalman Filter* consists of a set of mathematical equations that estimate the states of a process in a predictor-corrector fashion. It addresses the estimation problem of a process governed by linear stochastic difference equations through the minimization of the mean squared error of the estimates. The popularity of KF comes from its optimality in terms of Root Mean Square Error (RMSE), and its ability to minimize the *a posteriori* state estimation error [118]. A detailed introduction to the *Kalman Filter* can be found in [116], and is summarized as follows.

Consider a discrete-time system:

$$x_{k+1} = Ax_k + Bu_k + \omega_k, \quad \text{Equation}$$

with states $x \in \mathbb{R}^n$ and a measurement $z \in \mathbb{R}^m$:

$$z_{k+1} = Cx_{k+1} + v_{k+1}. \quad \text{Equation 5.1.2}$$

The random variables ω_k and v_k represent the process and the measurement noise, respectively. It is assumed that ω_k and v_k are independent of each other, and have zero mean Gaussian distributions, i.e.:

$$p(\omega) \sim N(0, Q), \quad \text{Equation 5.1.3}$$

$$p(v) \sim N(0, R) \quad \text{Equation 5.1.4}$$

where the process noise covariance Q and measurement noise covariance R are assumed to be constant during the process. The corresponding error covariance matrix is then defined as:

$$P_{k+1|k} = E[e_{k+1|k} e_{k+1|k}^T], \quad \text{Equation 5.1.5}$$

$$P_{k+1|k+1} = E[e_{k+1|k+1} e_{k+1|k+1}^T]. \quad \text{Equation 5.1.6}$$

The *a posteriori* state estimate $\hat{x}_{k+1|k+1}$ is defined as a linear combination of an *a priori* estimate $\hat{x}_{k+1|k}$ and a weighted difference between an actual measurement z_{k+1} and a measurement prediction $h\hat{x}_{k+1|k}$:

$$\hat{x}_{k+1|k+1} = \hat{x}_{k+1|k} + K_{k+1}(z_{k+1} - C\hat{x}_{k+1|k}) \quad \text{Equation 5.1.7}$$

where the difference $(z_{k+1} - C\hat{x}_{k+1|k})$ is called the measurement innovation; the $\hat{x}_{k+1|k} \in \mathbb{R}^n$ is the *a priori* state estimate at time $k + 1$ given the knowledge of the process at time k ; $\hat{x}_{k+1|k+1} \in \mathbb{R}^n$ is *a posteriori* state estimate at time $k + 1$ given the measurements z_{k+1} ; C is the measurement matrix; the K_{k+1} in Equation 5.1.7 is a $n \times m$ matrix used in every iteration of the estimation process, referred to as the Kalman gain:

$$K_{k+1} = P_{k+1|k} C^T (C P_{k+1|k} C^T + R_{k+1})^{-1} \quad \text{Equation 5.1.8}$$

The Kalman gain is designed to minimize the *a posteriori* error covariance, given as:

$$P_{k+1|k+1} = (I - K_{k+1}C)P_{k+1|k} \quad \text{Equation 5.1.9}$$

Note that R_k and Q_k can vary during the process, but they are often chosen as constants prior to the estimation. In the case where the measurement is less noisy, the corresponding measurement covariance R_k should be set to a relatively small value, and the Kalman gain thus weighs the measurement innovation more, as if the *Kalman Filter* ‘trusts’ the measurement more than the prediction of the model. Otherwise, the Kalman Filter ‘trusts’ the model more.

One of the very appealing features of the *Kalman Filter* comes from its *predictor-corrector* form, which recursively conditions the current estimate of a process on all of the past measurements. As Figure 72 shows, the *Kalman Filter* consists of time update equations, which are responsible for projecting forward the current estimates to obtain the *a priori* estimate of the next time step, and measurement update equations, which are responsible for incorporating the new measurement into the *a priori* estimate to produce the adjusted *a posteriori* estimate. After each time and measurement update pair, the process is repeated using the previous *a posteriori* estimates to predict the new *a priori* estimates.

In the implementation of the filter, the measurement noise covariance R_k and the process noise covariance Q_k are often manually tuned by trial and error.

5.2 The Extended Kalman Filter (EKF)

In the case where the system to be estimated is nonlinear, the classical *Kalman Filter* is modified to form the *Extended Kalman Filter* (EKF). The basic idea is to linearize the non-linear system model around the current state estimates using partial derivatives. This results in the loss of optimality, thus the EKF no longer provides the optimal estimates.

Consider a process governed by the nonlinear stochastic difference equation:

$$x_{k+1} = f(x_k, u_k) + \omega_k \quad \text{Equation 5.2.1}$$

with a measurement equation:

$$z_{k+1} = h(x_{k+1}) + v_{k+1} \quad \text{Equation 5.2.2}$$

where h is the nonlinear measurement model. Let $\hat{x}_{k+1|k}$ and $\hat{z}_{k+1|k}$ be the *a priori* state and measurement vectors respectively,

$$\hat{x}_{k+1|k} = f(\hat{x}_{k|k}, u_k) \quad \text{Equation 5.2.3}$$

And the corresponding *a priori* estimated error covariance becomes:

$$P_{k+1|k} = F_k P_{k|k} F_k^T + Q_k \quad \text{Equation 5.2.4}$$

where Q_k is the process noise covariance matrix. The matrices F_k and H_{k+1} are Jacobian matrices and are derived from the partial derivatives of f and h with respect to the states:

$$F_k = \left. \frac{\partial f(x)}{\partial x} \right|_{x=\hat{x}_{k|k}, u_k} \quad \text{Equation 5.2.5}$$

$$H_{k+1} = \left. \frac{\partial h(x)}{\partial x} \right|_{x=\hat{x}_{k+1|k}} \quad \text{Equation 5.2.6}$$

While the measurement error is given as:

$$\tilde{y}_{k+1} = z_{k+1} - h(\hat{x}_{k+1|k}) \quad \text{Equation 5.2.7}$$

and the measurement error covariance matrix S_{k+1} is defined as:

$$S_{k+1} = H_{k+1} P_{k+1|k} H_{k+1}^T + R_{k+1} \quad \text{Equation 5.2.8}$$

where R_{k+1} is the measurement noise covariance matrix. The next step is to update the *a priori* estimates to the *a posteriori* estimates, by applying the EKF gain:

$$\hat{x}_{k+1|k+1} = \hat{x}_{k+1|k} + K_{k+1} \tilde{y}_{k+1} \quad \text{Equation 5.2.9}$$

$$\text{where } K_{k+1} = P_{k+1|k} H_{k+1}^T S_{k+1}^{-1}, \quad \text{Equation 5.2.10}$$

The final step is to update the *a posteriori* estimation error covariance:

$$P_{k+1|k+1} = (I - K_{k+1} H_{k+1}) P_{k+1|k} \quad \text{Equation 5.2.11}$$

For mildly nonlinear system, the EKF is easy to implement and can provide satisfactory performance. However, the linearization of the system model in the EKF may introduce instabilities to the estimation process [117]. Besides, the EKF is sensitive to computer precision, and the complexity of computations is relatively high due to matrix inversions [118]. More discussions on the *Kalman*

Filter can be found in [117]. The steps involved in the EKF are also summarized in Table 10.

Table 10 Summary of EKF equations [116]

Time Update (Predictor)	Measurement Update (Corrector)
<p>(1). Projector the state ahead</p> $\hat{x}_{k+1 k} = f(\hat{x}_{k k}, u_k)$ <p>(2). Project the error covariance ahead</p> $P_{k+1 k} = F_k P_{k k} F_k^T + Q_k$	<p>(1). Compute the Kalman gain</p> $K_{k+1} = P_{k+1 k} H_{k+1}^T S_{k+1}^{-1}$ $S_{k+1} = H_{k+1} P_{k+1 k} H_{k+1}^T + R_{k+1}$ <p>(2). Update estimate</p> $\tilde{y}_{k+1} = z_{k+1} - h(\hat{x}_{k+1 k})$ $\hat{x}_{k+1 k+1} = \hat{x}_{k+1 k} + K_{k+1} \tilde{y}_{k+1}$ <p>(3). Update the error covariance</p> $P_{k+1 k+1} = (I - K_{k+1} H_{k+1}) P_{k+1 k}$

5.3 The Smooth Variable Structure Filter (SVSF)

The *Smooth Variable Structure Filter* (SVSF) was first presented in 2007, as the successor of *Variable Structure filter* (VSF) [101]. It is a novel model-based estimation strategy that closely relates to the sliding model control (SMC) concept. The SMC utilizes a discontinuous switching plane along the desired state trajectory (sliding surface), so as to keep the state values along this surface and minimize the trajectory errors [119, 120]. In this way, it can guarantee

stability given bounded uncertainties and disturbances [117]. This concept was brought to the design of SVSF, which lead to its stability and robustness. It was proved in [101] that SVSF with its inherent switching action can guarantee convergence of estimates to a neighbourhood of the actual states, given an upper bound for uncertainties and noise levels. This property is particularly advantageous for fault detection and condition monitoring. Hence, the SVSF was used in this research.

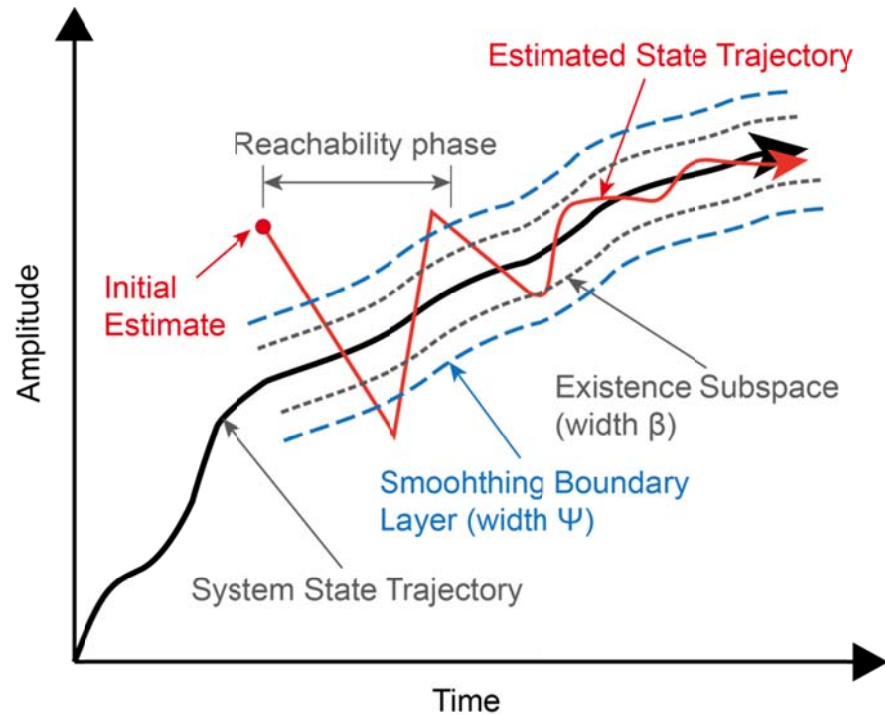


Figure 73 SVSF state estimation concept.

The basic idea of SVSF is illustrated in Figure 73, which shows the actual and the estimated trajectory of a single state being estimated. The estimation starts with an initial state value. Then, the SVSF predicts and adjusts the state

estimate given an uncertain system model and forces it towards the real trajectory. During this process, the estimated trajectory then reaches the existence subspace. The existence subspace is a time varying space that encloses the true state trajectory, and is calculated based on the state trajectory, uncertainties, noise, and disturbances. After reaching an existence subspace, the estimated state will stay within it and switch back and forth across the true state trajectory. The period from the beginning to when the estimates reach the existence subspace, is called the reachability phase, as marked in Figure 73.

The SVSF works in a predictor-corrector fashion that resembles the *Kalman Filter*. In every cycle of the estimation, the SVSF calculates an *a priori* state estimate $\hat{x}_{k+1|k}$ based on the *a posteriori* estimate $\hat{x}_{k|k}$ of the previous step, It then updates the *a priori* estimate $\hat{x}_{k+1|k}$ to an *a posteriori* value $\hat{x}_{k+1|k+1}$, by applying the SVSF gain. According to [101], during reachability phase the estimation will be stable and will converge to the existence subspace, if the following condition is satisfied:

$$|e_{k+1|k+1}| < |e_{k|k}| \quad \text{Equation 5.3.1}$$

Essentially, Equation 5.3.1 means that the *a posteriori* estimation error of SVSF will decrease with time, thus the estimate will converge to the existence subspace. The width of the existence subspace β varies with time, and is a function of the uncertain dynamics [117]. The upper bound of β can be estimated based on the upper bounds of uncertainties.

Since the chattering caused by the switching of the SVSF is not desirable in most cases, a smoothing boundary layer is used to smooth the estimates, as shown in Figure 73. The smoothing boundary layer should be chosen to enclose the existence subspace, i.e. $\psi > \beta$. Details of the derivation and proof of the SVSF can be found in [101, 117]. The following is a brief overview of the implementation steps of SVSF.

Consider a nonlinear process with a linear measurement equation, where the *a priori* state estimate $\hat{x}_{k+1|k}$ of the system can be expressed as:

$$\hat{x}_{k+1|k} = \hat{f}(\hat{x}_{k|k}, u_k) \quad \text{Equation 5.3.2}$$

The estimated measurements and the *a priori* estimation error can be derived as:

$$\hat{z}_{k+1|k} = C\hat{x}_{k+1|k} \quad \text{Equation 5.3.3}$$

$$e_{z,k+1|k} = z_{k+1} - \hat{z}_{k+1|k} \quad \text{Equation 5.3.4}$$

The SVSF gain is then defined as:

$$K_{k+1}^{SVSF} = C^{-}(|e_{z,k+1|k}| + \gamma|e_{z,k|k}|) \cdot \text{sat}\left(\frac{e_{z,k+1|k}}{\psi}\right) \quad \text{Equation 5.3.5}$$

where $|e_{z,k+1|k}|$ and $|e_{z,k|k}|$ are the absolute values of the *a priori* and the *a posteriori* state estimate error respectively; ψ is the smoothing boundary layer width; the SVSF convergence rate is defined by γ , that is chosen between 0 and 1; C is the measurement matrix. With the SVSF corrective action, the *a posteriori* state estimate at time $k + 1$ is calculated as:

$$\hat{x}_{k+1|k+1} = \hat{x}_{k+1|k} + K_{k+1}^{SVSF} \quad \text{Equation 5.3.6}$$

Then, the *a posteriori* estimated measurement $\hat{z}_{k+1|k+1}$ and the corresponding *a posteriori* estimation error are updated as:

$$\hat{z}_{k+1|k+1} = C\hat{x}_{k+1|k+1} \quad \text{Equation 5.3.7}$$

$$e_{z,k+1|k+1} = z_{k+1} - \hat{z}_{k+1|k+1} \quad \text{Equation 5.3.8}$$

Table 11 summarizes the process of the SVSF

Table 11 Summary of SVSF estimation steps

Time Update (Predictor)
<p>(1). Project the state ahead</p> $\hat{x}_{k+1 k} = \hat{f}(\hat{x}_{k k}, u_k)$ <p>(2). Update the <i>a priori</i> estimation error</p> $e_{z,k+1 k} = z_{k+1} - H_{k+1}\hat{x}_{k+1 k}$
Measurement Update (Corrector)
<p>(3). Compute the SVSF gain</p> $K_{k+1}^{SVSF} = C^{-}(e_{z,k+1 k} + \gamma e_{z,k k}) \cdot \text{sat}\left(\frac{e_{z,k+1 k}}{\psi}\right)$ <p>(4). Update the <i>a posteriori</i> state estimate</p> $\hat{x}_{k+1 k+1} = \hat{x}_{k+1 k} + K_{k+1}^{SVSF}$ <p>(5). Update the <i>a posteriori</i> measurement error</p> $e_{z,k+1 k+1} = z_{k+1} - C\hat{x}_{k+1 k+1}$

In the above equations, it is assumed that all of the states of the system have corresponding measurements and that the measurement matrix is full rank. Sometimes only some of the states are directly measurable. If the system is completely observable and controllable, then SVSF can still be applied. The solution to this 'fewer measurements than states' scenario is a 'reduced order' approach that formulates a full measurement matrix [101]. The idea is to construct 'artificial measurements' for the unmeasured states using available measurements [101]. As such, the aforementioned estimation steps can still be applied, and the SVSF can still provide robust estimates of the system that.

5.4 The EK-SVSF

The EK-SVSF is a combination of EKF and SVSF, which achieves better estimation accuracy while preserving the robustness feature of SVSF. This strategy is summarized below.

In an effort to achieve optimality, an optimal time varying smoothing boundary layer (VBL) was first derived in [121]. The original smoothing boundary layer was replaced by the VBL. The VBL was obtained by taking the partial derivative of the *a posteriori* error covariance matrix with respect to the smoothing boundary layer term [117]. In a linear system, the VBL yields an optimal gain value which makes SVSF equivalent to the *Kalman Filter*. The

convergence of the SVSF to the *Kalman Filter* or EKF is only desirable within the existence subspace for optimality. Outside of it, the SVSF should be retained to ensure robust stability, as illustrated in Figure 74. As such, an upper limit was specified for the VBL. Outside the limit the robustness and stability of the SVSF was maintained, while inside the boundary layer the optimal gain was applied.

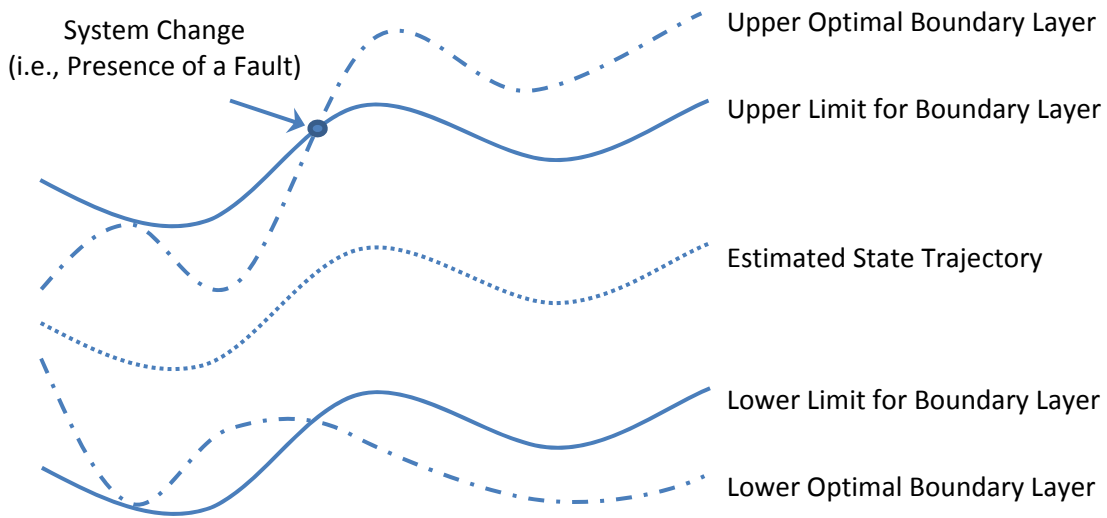


Figure 74 The concept of EK-SVSF strategy [117]

To calculate the VBL, the *a priori* estimation error covariance needs to be calculated:

$$P_{k+1|k} = F_k P_{k|k} F_k^T + Q_k \quad \text{Equation 5.4.1}$$

where the Q_k is the measurement noise covariance, as defined in Equation 5.1.3; F_k and H_k are the partial derivatives of the system matrix and the measurement matrix with respect to the states, respectively.

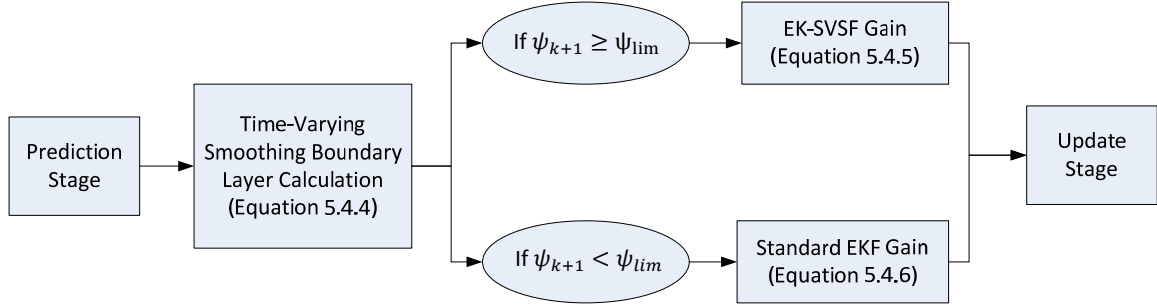


Figure 75 Methodology of combining nonlinear filtering strategies [117].

The *a priori* and the *a posteriori* estimation errors have the same formulation as defined in the original SVSF by Equation 5.3.4 and Equation 5.3.8. A new innovation covariance is obtained as:

$$S_{k+1} = H_{k+1}P_{k+1|k}H_{k+1}^T + R_{k+1} \quad \text{Equation 5.4.2}$$

Followed by a combined error vector:

$$\bar{A}_{k+1} = |e_{z,k+1|k}| + \gamma|e_{z,k|k}| \quad \text{Equation 5.4.3}$$

The VBL is defined as a function of S_{k+1} and A_{k+1} :

$$\psi_{k+1} = (\bar{A}_{k+1}^{-1}H_{k+1}P_{k+1|k}H_{k+1}^TS_{k+1}^{-1})^{-1} \quad \text{Equation 5.4.4}$$

Note that a 'divide by zero' check should be performed on Equation 5.4.3 to avoid inversion of zero in Equation 5.4.4 [117]. The concept behind the EK-SVSF is illustrated in Figure 75. Essentially, the values of Equation 5.4.4 are compared with the limits for the smoothing boundary layer widths (a designer setting) to determine which gain is used (EKF or SVSF) [117]. If the values of Equation 5.4.4 are larger than the limits (i.e. $\psi_{k+1} \geq \psi_{lim}$), the EK-SVSF gain is defined by:

$$K_{k+1} = H^{-1} \text{diag}[(|e_{z,k+1|k}| + \gamma |e_{z,k|k}|) \cdot \text{sat}(\bar{\psi}^{-1} e_{z,k+1|k})] [\text{diag}(e_{z,k+1|k})]^{-1}$$

Equation 5.4.5

Otherwise, the standard EKF gain may be used, as defined in Equation 5.4.6.

$$K_{k+1} = H_{k+1}^{-1} \bar{A}_{k+1} \psi_{k+1}^{-1}$$

Equation 5.4.6

The *a posteriori* state estimate equation is modified as:

$$\hat{x}_{k+1|k+1} = \hat{x}_{k+1|k} + K_{k+1} e_{z,k+1|k}$$

Equation 5.4.7

Finally, the *a posteriori* estimation error covariance is obtained as:

$$P_{k+1|k+1} = (I - K_{k+1} H_{k+1}) P_{k+1|k} (I - K_{k+1} H_{k+1})^T + K_{k+1} R_{k+1} K_{k+1}^T$$

Equation 5.4.8

Finally, the *a posteriori* measurement error $e_{z,k+1|k+1}$ is updated using $\hat{x}_{k+1|k+1}$,

$$e_{z,k+1|k+1} = z_{k+1} - h(\hat{x}_{k+1|k+1})$$

Equation 5.4.9

Table 12 Summary of EK-SVSF (Predictor)

Time Update (Predictor)
<p>(1). Project the state ahead</p> $\hat{x}_{k+1 k} = \hat{f}(\hat{x}_{k k}, u_k)$ <p>(2). Linearize the system and the measurement matrices</p> $F_k = \left. \frac{\partial f(x)}{\partial x} \right _{x=\hat{x}_{k k}, u_k} \quad \text{and} \quad H_{k+1} = \left. \frac{\partial h(x)}{\partial x} \right _{x=\hat{x}_{k+1 k}}$

(3). Calculate the *a priori* estimation error covariance

$$P_{k+1|k} = F_k P_{k|k} F_k^T + Q_k$$

(4). Update *a priori* estimation error

$$e_{z,k+1|k} = z_{k+1} - h(\hat{x}_{k+1|k})$$

Table 13 Summary of EK-SVSF (Corrector)

Measurement Update (Corrector)
<p>(5). Calculate the smoothing boundary layer width ψ_{k+1}</p> $S_{k+1} = H_{k+1} P_{k+1 k} H_{k+1}^T + R_{k+1} \quad \bar{A}_{k+1} = (e_{z,k+1 k} + \gamma e_{z,k k}) \quad \psi_{k+1}$ $\bar{A}_{k+1} = (e_{z,k+1 k} + \gamma e_{z,k k}) \quad \psi_{k+1} = (\bar{A}_{k+1}^{-1} H_{k+1} P_{k+1 k} H_{k+1}^T S_{k+1}^{-1})^{-1}$ $\psi_{k+1} = (\bar{A}_{k+1}^{-1} H_{k+1} P_{k+1 k} H_{k+1}^T S_{k+1}^{-1})^{-1}$ $= (\bar{A}_{k+1}^{-1} H_{k+1} P_{k+1 k} H_{k+1}^T S_{k+1}^{-1})^{-1}$ <p>(6). Compute the EK-SVSF gain</p> $K_{k+1} = \begin{cases} P_{k+1 k} H_{k+1}^T S_{k+1}^{-1}, & \text{if } \psi_{k+1} < \psi_{lim} \\ H^{-1} \text{diag}[(e_{z,k+1 k} + \gamma e_{z,k k}) \cdot \text{sat}(\bar{\psi}^{-1} e_{z,k+1 k})] [\text{diag}(e_{z,k+1 k})]^{-1}, & \text{if } \psi_{k+1} \geq \psi_{lim} \end{cases}$ <p>(7). Update <i>a posteriori</i> state estimate</p> $\hat{x}_{k+1 k+1} = \hat{x}_{k+1 k} + K_{k+1} e_{z,k+1 k}$ <p>(8). Calculate <i>a posteriori</i> estimation error covariance</p> $P_{k+1 k+1} = (I - K_{k+1} H_{k+1}) P_{k+1 k} (I - K_{k+1} H_{k+1})^T + K_{k+1} R_{k+1} K_{k+1}^T$

(9).Update *a posteriori* measurement error

$$e_{z,k+1|k+1} = z_{k+1} - h(\hat{x}_{k+1|k+1})$$

5.5 Summary

This chapter briefly described the implementation of the *Extend Kalman Filter* and the *Smooth Variable Structure Filter*. The EKF is well-established in the estimation field. For linear systems with Gaussian noise, the *Kalman Filter* provides optimal estimates in terms of mean square error. In nonlinear systems, the EKF is applied. The *Kalman Filter* suffers a major drawback which is its sensitivity to modeling uncertainties.

To overcome this limitation, the SVSF may be used [117]. The SVSF is a robust state estimator [101]. The EK-SVSF provides the accuracy of the EKF as well as the robustness of the SVSF in the presence of modeling errors.

Chapter 6 Experimental Results of Stator Winding Fault Diagnosis

In terms of the stator winding faults of electric motors, the most common ones are the open circuit and short circuit faults. It is believed that these faults usually start as turn-to-turn faults and then gradually grow and culminate into a winding failure [16]. With the progression and the deterioration of the fault, the stator winding resistance will also vary correspondingly with time. Thus, the continuous estimation of the stator winding resistance becomes very important in condition monitoring of motors. In this research, artificial winding faults were physically simulated on the test motor. A description of experimental setup is provided in Appendix 1. With the measurements of the currents and voltages of the three phases, the estimation techniques were applied to track the variation of the winding resistance. Specifically, the EKF and EK-SVSF were implemented for estimation of the states and the parameters of the motor.

The EK-SVSF was applied for the estimation of the states and the parameters of the test motor. The EK-SVSF requires a model of the motor as defined later in this chapter (Equation 6.5.1). A goal of this research was to compare the effectiveness of the EK-SVSF with that of the Extended Kalman Filter in the diagnosis of stator winding faults.

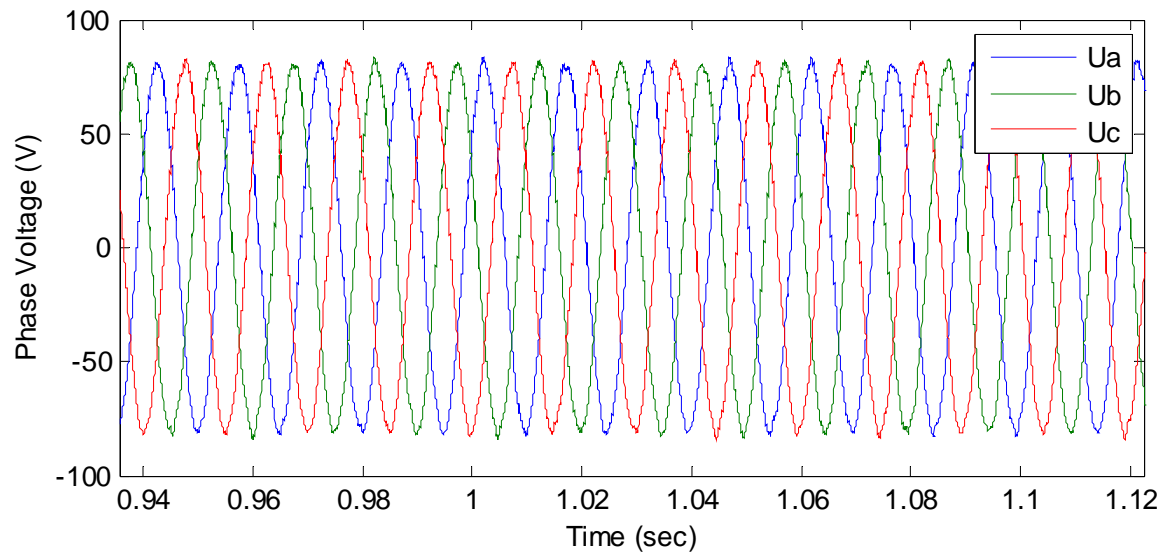


Figure 76 Typical voltage measurements

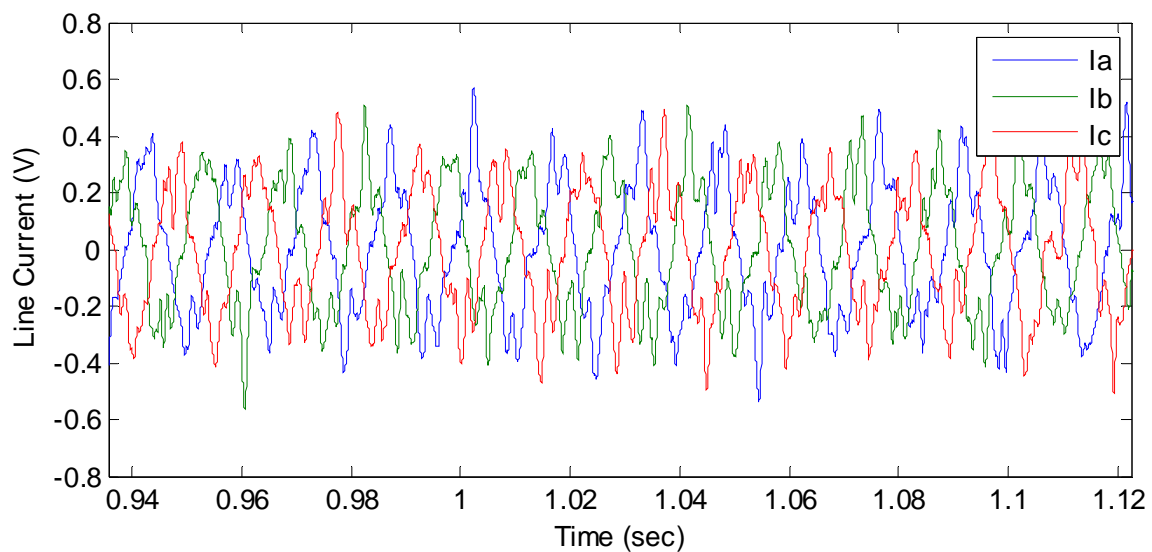


Figure 77 Typical current measurements

The experimental setup used in this study is described in Appendix 1. . As shown in Figure 76, the phase-to-neutral input voltages U_a , U_b and U_c of the motor. The phase voltages were obtained by direct line voltage measurements. The associated phase currents were also measured as shown in Figure 77. All

measurements were pre-processed by an anti-aliasing filter with a cut-off frequency of 500 Hz. During the test, the speed of the motor was fixed to 1000 RPM with no external load. The angular position of the motor was measured by an absolute encoder.

The discrete-time state space model of the motor was obtained based on Equation 1.2.1 to Equation 1.2.4 [122-124], and an equivalent circuit diagram shown in Figure 78 (same as Figure 1). More descriptions can be found in Section 1.2.

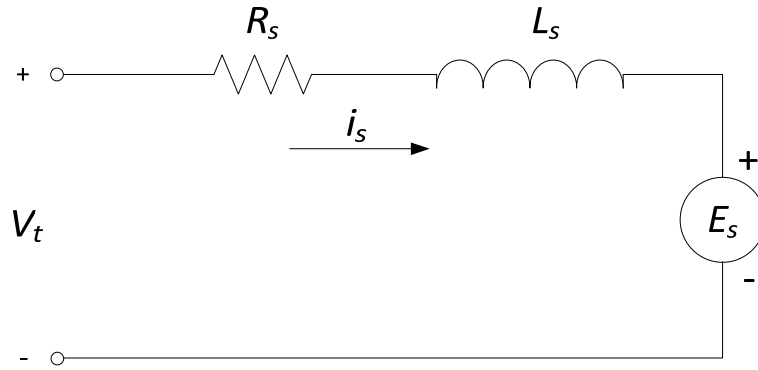


Figure 78 Simplified equivalent circuit of the BLDC motor (same as Figure 1) [3].

The motor was modeled as a third-order nonlinear system with six state variables related to its phase currents and phase resistances. The value of the constants used in the model can be found in Table 21 in the Appendix 1.

At the beginning, the estimated states were initialized to zero. The sampling frequency of the system was $f_T = 32,000 \text{ Hz}$.

$$\begin{aligned} \mathbf{x}^{k+1} = & \begin{bmatrix} -R_a^k dt/L_s & 0 & 0 & 0 & 0 & 0 \\ 0 & -R_b^k dt/L_s & 0 & 0 & 0 & 0 \\ 0 & 0 & -R_c^k dt/L_s & 0 & 0 & 0 \\ 0 & 0 & 0 & 1 & 0 & 0 \\ 0 & 0 & 0 & 0 & 1 & 0 \\ 0 & 0 & 0 & 0 & 0 & 1 \end{bmatrix} \cdot \mathbf{x}^k \\ & + \begin{bmatrix} dt/L_s & 0 & 0 & -K_e \Phi_a^k & 0 \\ 0 & dt/L_s & 0 & -K_e \Phi_b^k & 0 \\ 0 & 0 & dt/L_s & -K_e \Phi_c^k & 0 \\ 0 & 0 & 0 & 0 & 0 \\ 0 & 0 & 0 & 0 & 0 \\ 0 & 0 & 0 & 0 & 0 \end{bmatrix} \cdot \mathbf{u}^k \end{aligned} \quad \text{Equation 6.5.1}$$

$$\mathbf{x}^k = [I_a^k \quad I_b^k \quad I_c^k \quad R_a^k \quad R_b^k \quad R_c^k]^T, \quad \text{Equation 6.5.2}$$

$$\mathbf{u}^k = [u_a^k \quad u_b^k \quad u_c^k \quad \omega^k \quad \theta_e^k], \quad \text{Equation 6.5.3}$$

where $\Phi_a^k = \sin(\theta_e)$, $\Phi_b^k = \sin\left(\theta_e + \frac{2}{3}\pi\right)$, $\Phi_c^k = \sin\left(\theta_e - \frac{2}{3}\pi\right)$, and the relation between the electrical angle θ_e and the physical angle θ of the rotor is $\theta_e = 2P\theta$, P is the number of pole pairs. $K_e = 0.77$ [V · s/rad] and $L_s = 0.0048$ [H]. The corresponding measurement equation can be defined as:

$$\mathbf{z}^{k+1} = \mathbf{C} \cdot \mathbf{x}^{k+1} \quad \text{Equation 6.5.4}$$

where \mathbf{C} is the measurement matrix.

Note that for systems that have fewer measurements than states, Luenberger's approach is used to formulate a full measurement matrix, as

presented in [101, 117, 125]. Essentially, 'artificial measurements' are created and used throughout the estimation process [117]. In this case, the artificial measurements of phase resistances were calculated using available measurements of the phase voltages and currents, as given by Equation 6.5.5:

$$r_{MN,a} = \frac{u_{MN,a} - L \frac{di_{MN,a}}{dt} - K_{e2} \omega_{MN}}{i_{MN,a}} \quad \text{Equation 6.5.5}$$

where the subscript "MN" denotes the mean value of the variable in every half cycle, the subscript "a" denotes phase A, and K_{e2} is a voltage constant which equals to $0.4877 \text{ [V} \cdot \text{s/rad]}$. The $r_{MN,a}$ was then low-pass filtered to reduce the noise amplified by the differentiation operation in Equation 6.5.5. An example of the artificial measurements is shown in Figure 79.

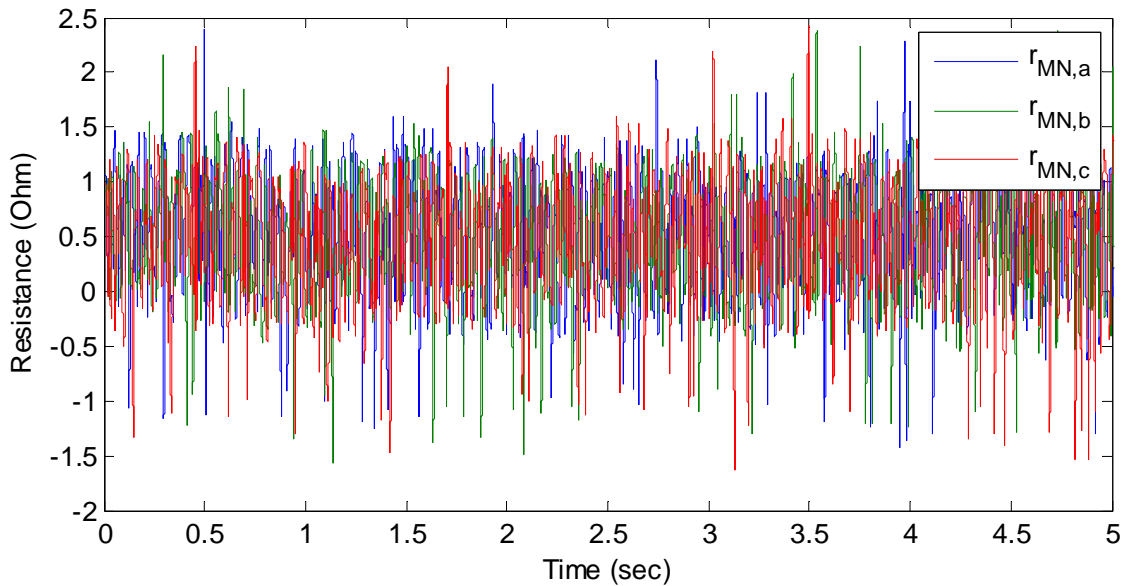


Figure 79 Artificial measurements of phase resistance

Thus, the new measurement vector \mathbf{z}^{k+1} is defined as:

$$\mathbf{z}^{k+1} = [i_a^{k+1} \quad i_b^{k+1} \quad i_c^{k+1} \quad r_{MN,a}^{k+1} \quad r_{MN,b}^{k+1} \quad r_{MN,c}^{k+1}]^T$$

where the measurement matrix C becomes an identity matrix, i.e.:

$$C = \begin{bmatrix} 1 & 0 & 0 & 0 & 0 & 0 \\ 0 & 1 & 0 & 0 & 0 & 0 \\ 0 & 0 & 1 & 0 & 0 & 0 \\ 0 & 0 & 0 & 1 & 0 & 0 \\ 0 & 0 & 0 & 0 & 1 & 0 \\ 0 & 0 & 0 & 0 & 0 & 1 \end{bmatrix}$$

Note that the same (artificial) measurements were used by both of the SVSF and the Kalman Filter. For the Kalman Filter, the artificial measurements could decrease estimation errors, particularly in the presence of modeling uncertainties [126]. Some results of the Kalman Filter without using Luenberger's approach are provided in Appendix 2 as a comparison.

The For the Kalman Filter, the system noise covariance Q and measurement noise covariance R , and initial state error covariance $P_{0|0}$ were determined by trial and error as follows:

$$Q = \begin{bmatrix} 1 \times 10^{-5} & 0 & 0 & 0 & 0 & 0 \\ 0 & 1 \times 10^{-5} & 0 & 0 & 0 & 0 \\ 0 & 0 & 1 \times 10^{-5} & 0 & 0 & 0 \\ 0 & 0 & 0 & 0.5 \times 10^{-7} & 0 & 0 \\ 0 & 0 & 0 & 0 & 0.5 \times 10^{-7} & 0 \\ 0 & 0 & 0 & 0 & 0 & 0.5 \times 10^{-7} \end{bmatrix},$$

$$R = \begin{bmatrix} 1 \times 10^{-3} & 0 & 0 & 0 & 0 & 0 \\ 0 & 1 \times 10^{-3} & 0 & 0 & 0 & 0 \\ 0 & 0 & 1 \times 10^{-3} & 0 & 0 & 0 \\ 0 & 0 & 0 & 0.2 & 0 & 0 \\ 0 & 0 & 0 & 0 & 0.2 & 0 \\ 0 & 0 & 0 & 0 & 0 & 0.2 \end{bmatrix},$$

$$P_{0|0} = \begin{bmatrix} 1 \times 10^{-4} & 0 & 0 & 0 & 0 & 0 \\ 0 & 1 \times 10^{-4} & 0 & 0 & 0 & 0 \\ 0 & 0 & 1 \times 10^{-4} & 0 & 0 & 0 \\ 0 & 0 & 0 & 1.5 \times 10^{-4} & 0 & 0 \\ 0 & 0 & 0 & 0 & 1.5 \times 10^{-4} & 0 \\ 0 & 0 & 0 & 0 & 0 & 1.5 \times 10^{-4} \end{bmatrix},$$

For the EK-SVSF, the ‘memory’ or convergency rate was set to $\gamma = 0.2$. The limit for the smoothing boundary layer widths for the six states were set as $\psi = [2 \ 2 \ 2 \ 2 \ 2 \ 2]^T$.

Four different cases were studied. The first case was considered a normal condition, where no faults occurred in the motor.

The second case included a faulty resistance in one of the phases of the motor. The fault conditions are described in Table 14.

Table 14 Faulty conditions of the motor in the sencond case of experimental tests

Fault Condition	Normal Resistance	Faulty Resistance	Occurrence Time	Duration
Change of winding resistance in phase C	$R_c = 0.5 \text{ Ohm}$	$R_c = 1.0 \text{ Ohm}$	$t = 8 \text{ sec}$	Till the end

In the third case, a modeling error was injected in to the estimator half-way through the process, in order to test the robustness of the methods. The modeling uncertainties are described in Table 15.

Table 15 Modeling uncertainties in the third case of experimental tests

Type of Modeling Uncertainties	Normal Condition	Modeling Error Condition	Occurrence Time	Duration
Change of the model parameter K_e	$K_e = 0.77$	$K_e = 0.77 * 90\%$	$t = 1.7 \text{ sec}$	$t = 1.6 \text{ sec}$

The fourth case was a combination of the second case and the third case, which involved the faulty resistance and the modeling error. The fault conditions and modeling uncertainties are provided in Table 16.

Table 16 Fault conditions and modeling uncertainties in the fourth case of experimental tests

Fault Condition / Modeling Uncertainties	Normal	Faulty	Occurrence Time	Duration
Change of winding resistance in phase C	$R_c = 0.5 \text{ Ohm}$	$R_c = 1.0 \text{ Ohm}$	$t = 8 \text{ sec}$	Till the end
Change of the model parameter K_e	$K_e = 0.77$	$K_e = 0.77 * 90\%$	$t = 8 \text{ sec}$	Till the end

6.1 Normal Condition

In this case, the motor was running in normal conditions. Figure 80 and Figure 81 show the parameter estimation results from the EK-SVSF and the Extended Kalman Filter, respectively. The nominal phase resistance of the motor is 0.5 Ohm. As we can see from the figures, the EKF and the EK-SVSF produce similar results when estimating this resistance. The current estimates for both the EK-SVSF and the EKF are also comparable. The Root Mean Square Error (RMSE) comparison of two filters is presented in Table 17.

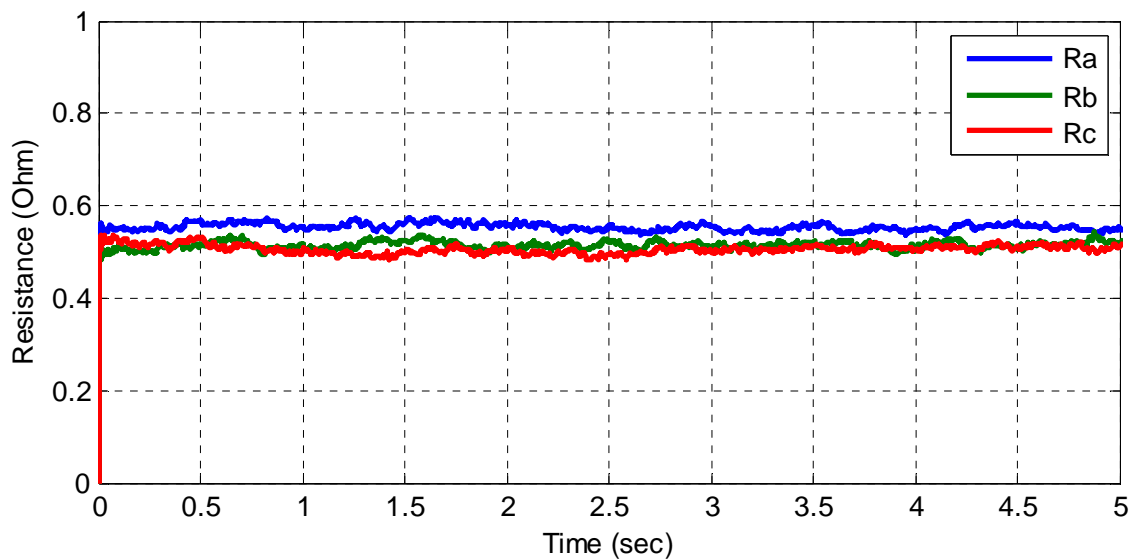


Figure 80 Estimation of phase resistance using EK-SVSF

A small discrepancy in the estimation of R_a is observed in Figure 80 and Figure 81. This discrepancy is also found in all of the following results, and is believed to be caused by the slightly unbalanced supply voltage in phase A from the motor drive.

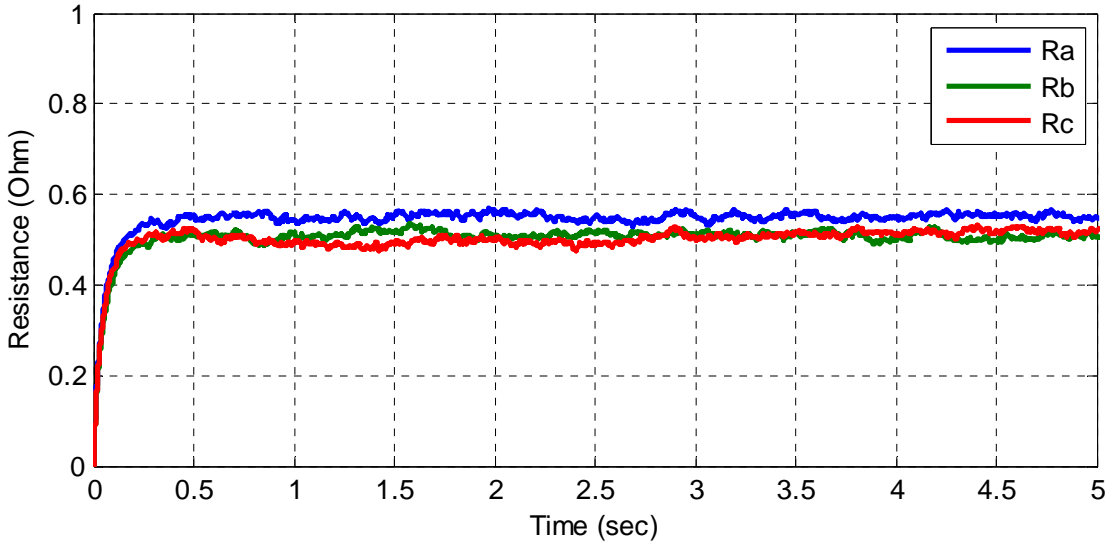


Figure 81 Estimation of phase resistance using Extended Kalman Filter (EKF)

As claimed in [117], for a known system subjected to Gaussian noise, the Kalman Filter gives the optimal estimates. The EK-SVSF yields the same results with better robustness. In this case, the target system is nonlinear, and the noise distribution is Gaussian but not exactly known.

Table 17 Root Mean Square Error of estimated parameters (Normal Case)

Filter	R_a	R_b	R_c
EKF	5.939×10^{-2}	3.723×10^{-2}	3.587×10^{-2}
EK-SVSF	5.042×10^{-2}	1.266×10^{-2}	1.355×10^{-2}

As shown in Table 17, EK-SVSF outperformed the EKF in terms of the RMSE. This is likely due to the faster convergence of EK-SVSF over EKF at first 0.5 sec, which results in an overall smaller RMSEs. Furthermore, if the leftmost

part of Figure 80 is compared to Figure 81, it can be seen that the EK-SVSF converges to the true state trajectory faster than the EKF. This demonstrates the merits of EK-SVSF, which brings the fast convergence property of SVSF together with the accuracy of the EKF, thus giving a better overall performance than either alone.

6.2 Winding Resistance Fault

To simulate this fault condition, an external resistor was added to the stator winding of the motor, doubling its resistance R_c halfway in the estimation process. A description of experimental setup is provided in the Appendix 1.

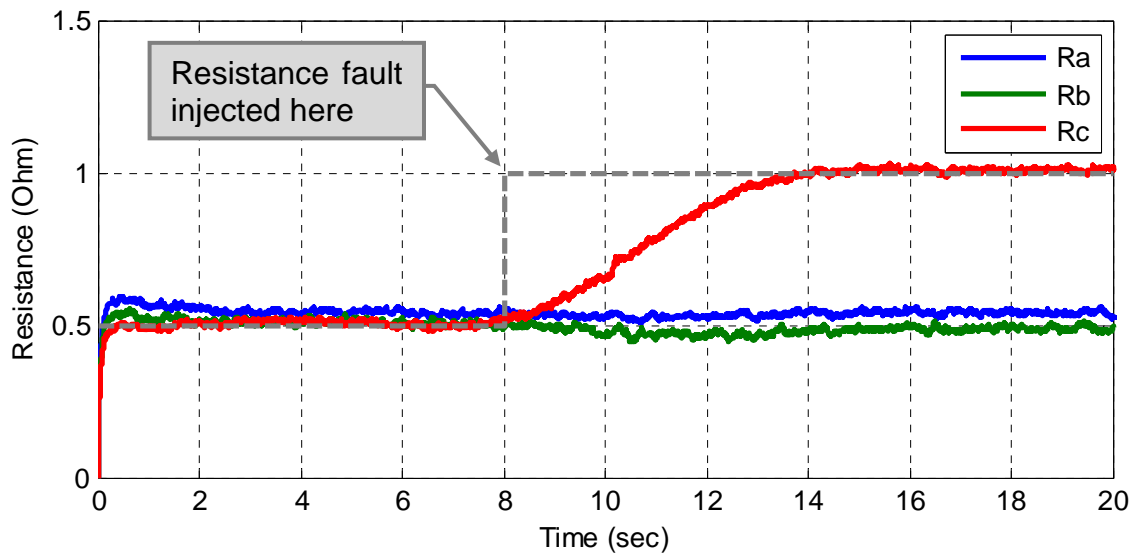


Figure 82 Estimation of phase resistance using Extended Kalman Filter (EKF)

Figure 82 shows the estimated resistance by using the EKF, with the dashed line in grey indicating the change in the resistance value. As we can see

from Figure 82, EKF provides satisfactory results. The change in the resistance R_c from 0.5 Ohm to 1 Ohm was successfully captured, and the estimation of the other two phases are not affected by this disturbance. Figure 83 shows the estimation results of the EK-SVSF that are similar to that of the EKF. The reason is that in the absence of modeling error, the SVSF gain is practically the same as that of the EKF's. The change in the resistance R_c was successfully tracked, and the estimation stabilized. As we can see in the Figure 83, the change of R_c did not affect the other two phases. This means the approach can estimate the three states independently in a decoupled way.

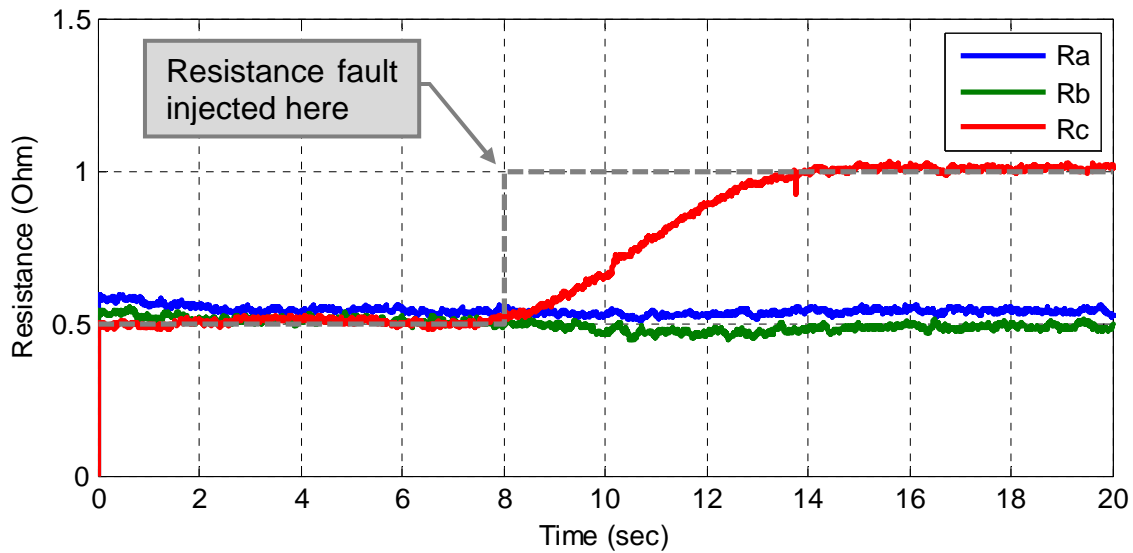


Figure 83 Estimation of phase resistance using EK-SVSF

The RMSE of the estimation given in Table 18 also suggests that the performance of these two methods is similar. The RMSE of the R_c estimate is nearly the same for both the EK-SVSF and the EKF. The EK-SVSF has slightly

smaller error in R_a and R_b , mostly because of the faster convergence of the EK-SVSF in the beginning of the estimation.

Table 18 Root Mean Square Error of estimated parameters (Winding Resistance Fault)

Filter	R_a	R_b	R_c
EKF	3.224×10^{-2}	1.150×10^{-2}	1.409×10^{-1}
EK-SVSF	3.057×10^{-2}	1.004×10^{-2}	1.364×10^{-1}

6.3 Modeling Uncertainty

The third case was to compare the robustness of the filters under modeling uncertainties. As per [101], consider the introduction of a modeling error or uncertainty at 1.7 seconds into the test. The modeling uncertainty was introduced by decreasing the value of K_e in the model by 10%. The altered parameter was then changed back to the correct value at 3.3 seconds. While the model given to the filters was changed, the actual running conditions of the motor remained the same. The corresponding resistance estimates for this case are shown in the following figures.

Figure 84 is the result from the EKF. The abrupt jump at 1.7 sec is shown together with a sudden drop at 3.3 sec. The estimation error of the EKF due to the modeling uncertainties is more than five times larger than the true value. Obviously, the estimates of EKF completely diverge from the true state trajectory

because of the injected modeling error. Although Kalman Filter gives the optimal estimate in known systems with white noise, one of its well-known deficiencies is its sensitivity to modeling uncertainties.

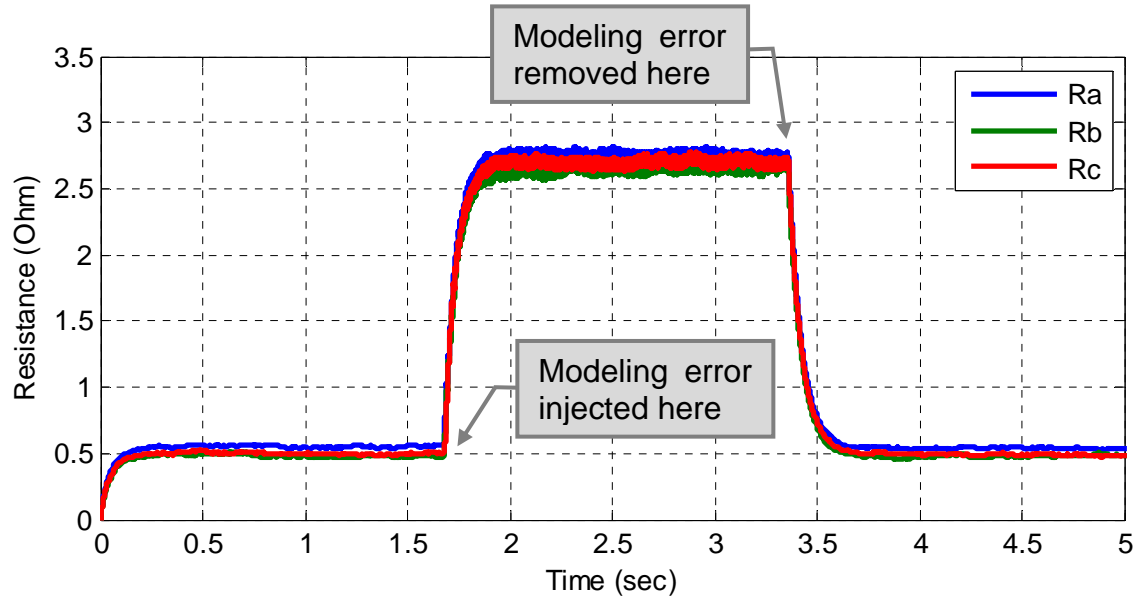


Figure 84 Estimation of phase resistance using Extended Kalman Filter (EKF)

On the other hand, the estimation results in Figure 85 demonstrate the robustness of the EK-SVSF given modeling uncertainties. As seen in Figure 85, the modeling error from 1.7 seconds to 3.3 seconds does not cause a large error in the estimated resistance R_c . Instead, all of the three states start chattering around the true state values when modeling errors are injected. As the author of the SVSF points out [101], the merit of SVSF lies in its ability to minimize the influence of modeling errors while preserving stability. Furthermore, the chattering phenomenon shown in Figure 85 is an indicator that can be used to identify the hidden fault in the system. Although the estimates of EK-SVSF are

not completely immune from the injected modeling error, the EK-SVSF is nevertheless much better than the EKF, as compared in Table 19.

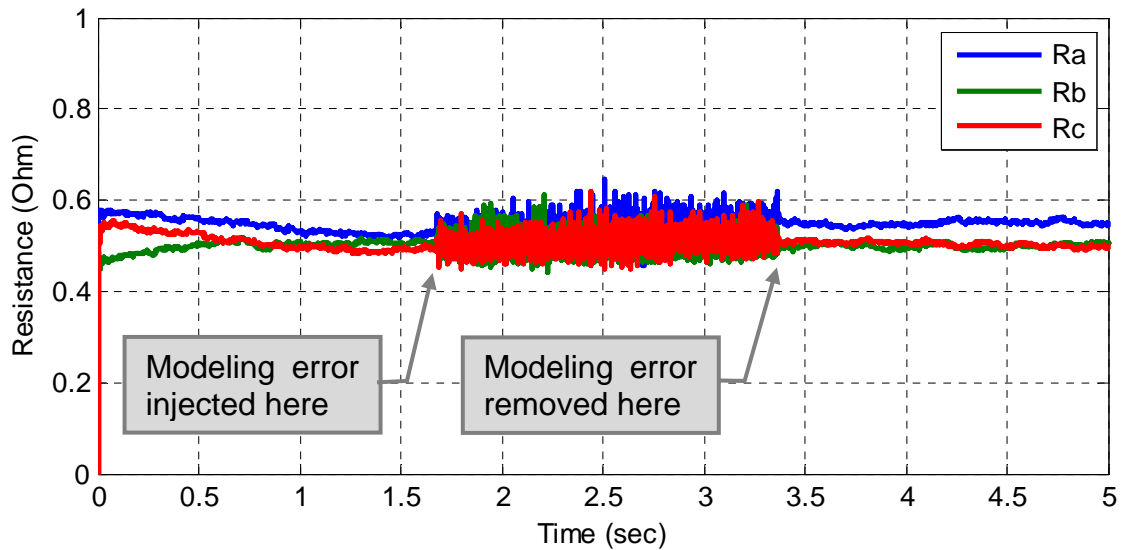


Figure 85 Estimation of phase resistance using EK-SVSF

In addition, the VBL is a reflection of the modeling uncertainties during the estimation process. Figure 86 shows that after the modeling uncertainties are injected into the model at 1.7 seconds, the VBL also increases drastically. The variation of the VBL thus is another indicator for fault conditions.

Note that under normal conditions, the EK-SVSF has the same performance as the EKF. However, when the system is subjected to modeling uncertainties, as shown in Figure 84 and Figure 85, the EKF fails to yield a reasonable estimate and deviates from the true values. The EK-SVSF on the other hand remains robust and stable. Its estimates remain bounded to within a

region of the true state trajectory. In terms of RMSE, the EK-SVSF strategy in this case also yields much better results, as shown in the following table.

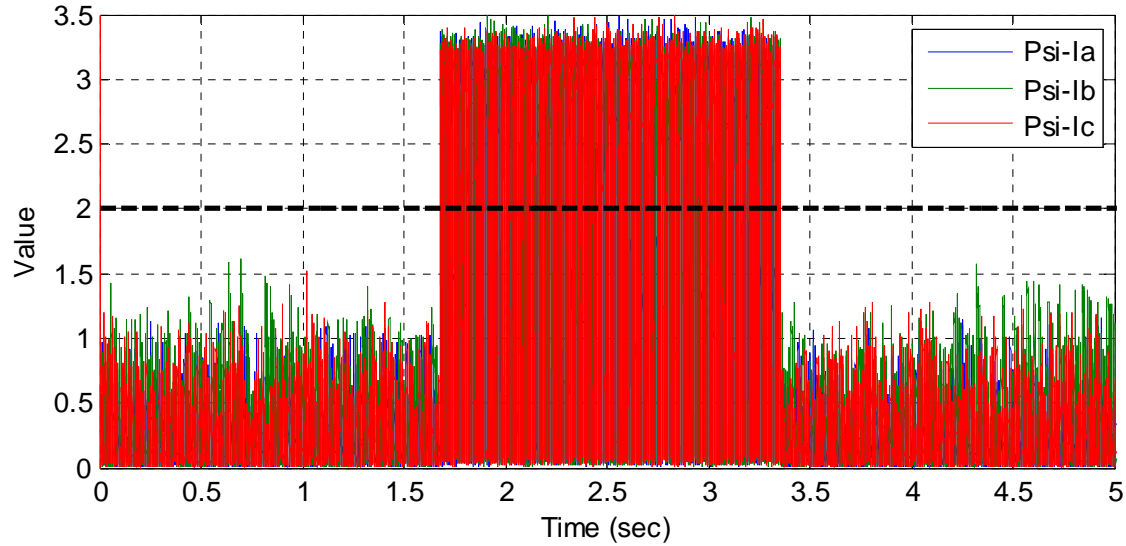


Figure 86 The VBL trajectory of the three-phase currents in EK-SVSF

Table 19 Root Mean Square Error of estimated parameters (Modeling Uncertainty)

Filter	R_a	R_b	R_c
EKF	1.283×10^0	1.248×10^0	1.252×10^0
EK-SVSF	5.157×10^{-2}	1.637×10^{-2}	1.804×10^{-2}

In this case, it is very clear that the SVSF greatly outperformed EKF, as the RMSEs of the EKF are more than 30 times larger than those of the EK-SVSF.

6.4 Winding Resistance Fault and Modeling Uncertainty

The fourth case was a combination of the second case (Section 6.3) and the third case (Section 6.4), which involved the resistance fault as well as the modeling uncertainty. Consider the introduction of a modeling uncertainty at 8 seconds into the test. The modeling uncertainty was introduced by decreasing the value of K_e in the model by 10%. At the same time, an external resistor was also added to the stator winding of the motor, doubling its resistance R_c halfway in the estimation process. Note that the resistance fault and the modeling uncertainty occurred at the same time in order to exaggerate the effect of uncertainty in the system. The corresponding resistance estimates for this case are shown in the following figures.

Figure 87 shows the estimated resistance by using the EKF, with the dashed line in grey indicating the change in the resistance value. As we can see, the estimation error of the EKF is more than three times larger than the true value. Apparently, the estimates of EKF were strongly affected by the modeling error and diverged from the true state trajectory. Although Kalman Filter gives the optimal estimate in known systems with white noise, one of its well-known deficiencies is its sensitivity to modeling uncertainties.

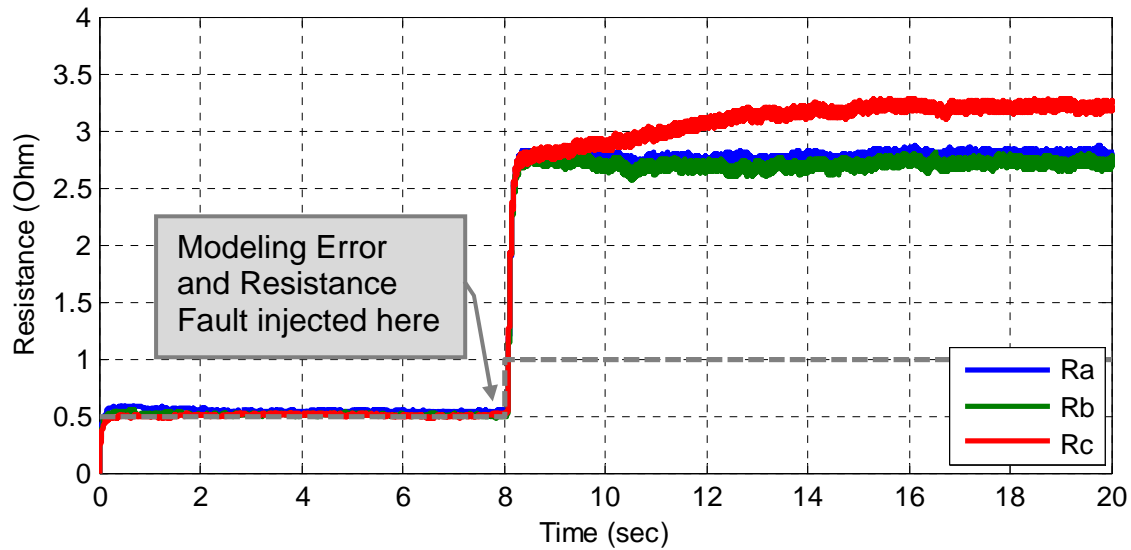


Figure 87 Estimation of phase resistance using Extended Kalman Filter (EKF)

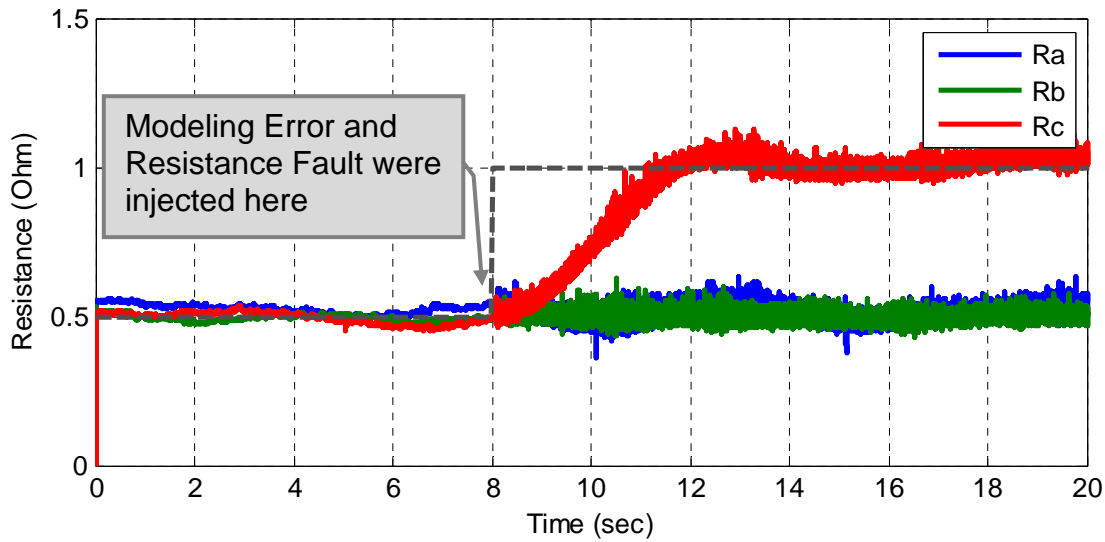


Figure 88 Estimation of phase resistance using EK-SVSF

On the other hand, the estimation results in Figure 88 demonstrate the robustness of the EK-SVSF given modeling uncertainties. The modeling uncertainty does not cause a large error in the estimated resistance R_c , and the resistance fault is effectively estimated by EK-SVSF. Furthermore, all of the three

states start chattering after the injection of modeling errors. The chattering phenomenon shown in Figure 88 is an indicator that can be used to identify the hidden fault in the system. Although the estimates of EK-SVSF are not completely immune from the injected modeling error, the EK-SVSF is nevertheless much better than the EKF.

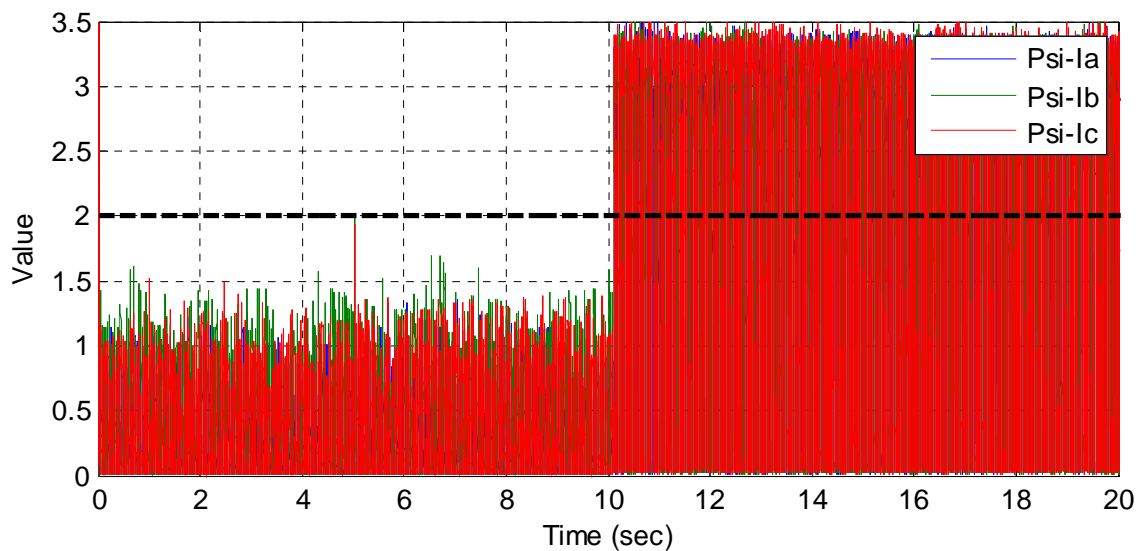


Figure 89 The VBL trajectory of the three-phase currents in EK-SVSF

Under normal conditions, the EK-SVSF has the same performance as the EKF. However, when the system is subjected to modeling uncertainties, as shown in Figure 84 and Figure 85, the EKF fails to yield a reasonable estimate and deviates from the true values. The EK-SVSF on the other hand remains robust and stable. Its estimates remained bounded to within a region of the true state trajectory.

The VBL is a reflection of the modeling uncertainties during the estimation process. As shown in Figure 89, the VBL increases drastically when the modeling uncertainty is injected into the system. The variation of the VBL in SVSF thus is another useful indicator of fault conditions in the system being estimated.

Table 20 Root Mean Square Error of estimated parameters

Filter	R_a	R_b	R_c
EKF	1.751×10^0	1.704×10^0	2.007×10^0
EK-SVSF	3.633×10^{-2}	1.480×10^{-2}	1.409×10^{-1}

In terms of RMSE, the EK-SVSF strategy in this case also yields much better results. As shown in Table 20, the RMSEs of the EKF are much larger than those of the EK-SVSF.

6.5 Summary

This section presented the implementation of the EK-SVSF and the EKF for estimating the states and the parameters of a BLDC motor. The *Kalman Filter* provides optimal estimates in linear known systems with Gaussian noise, but it suffers from a major drawback which is the sensitivity to modeling uncertainties. The *Smooth Variable Structure Filter* is a robust state estimator with a secondary indicator for modeling uncertainties. The EK-SVSF is a combination of the EKF

and the SVSF which has the performance of the EKF and the robustness of the SVSF.

In order to physically simulate the stator winding faults, resistors were added to the external winding circuits. In an effort to detect those faults, the winding resistance of the three phases of the motor were monitored simultaneously using EK-SVSF and the EKF. The results of the EK-SVSF were compared to that of the EKF. Experimental results demonstrated that both of the EK-SVSF and the EKF produced accurate estimates when the model of the motor was known. In the presence of modeling errors, however, the EKF deviated from the true state trajectories, while the EK-SVSF still gave accurate estimates with a low degree of chattering. Moreover, the VBL width of the EK-SVSF was found to be a secondary indicator for the changes in the system and the modeling errors.

Chapter 7 Concluding Remarks

7.1 Summary of Research

Unexpected motor failures in rotating equipment can result in unplanned production downtime, costly replacement of parts and safety concerns. Thus, fast and efficient fault detection and diagnosis of electric motors are necessary in order to maintain a high degree of reliability and operational safety. It has been reported that bearing faults and stator winding faults cause the majority of motor failures. In this research, these faults were physically simulated on a Permanent Magnet Brushless DC Motor. Signal-based and model-based fault detection and diagnosis techniques were proposed and used successfully to detect the above mentioned faults.

When a bearing contains a fault, the resulting vibration signal exhibits characteristic features that can be utilized to detect the fault. However, the vibration signal from a bearing with an incipient fault is usually masked by machine noise, making it difficult to detect the fault signature. In this research, a signal processing method that incorporated the Dual-Tree Complex Wavelet Transform with the Bivariate shrinkage was applied for signal denoising and feature extraction from the measured vibration signal. Envelope analysis was then used to extract modulated impulses associated with faults. Different bearing conditions, including inner race fault, outer race fault and multiple faults, were

physically simulated and were all successfully detected using the proposed method. The effectiveness of the approach was further demonstrated by using the Extra Urban Driving Cycle, where the speed of the motor was varied according to a pre-defined driving profile. Both numerical simulations and experimental results showed that the DTCWT-based fault diagnosis approach was very effective for bearing fault diagnosis in electric motors, without any necessary optimization to enhance its performance.

The *Kalman Filter* provides optimal estimates in linear known systems with white noise. However, its performance degrades in the presence of modeling uncertainties. The *Smooth Variable Structure Filter* is an estimation strategy that is robust to modeling uncertainties. The EK-SVSF is a combination of the EKF and the SVSF which has the performance of the EKF and the robustness of the SVSF. In this research, stator winding faults were physically simulated by adding resistors to the external winding circuits. In an effort to detect those faults, the winding resistance of the three phases of the motor were monitored simultaneously using the EKF and the EK-SVSF estimation techniques. The EK-SVSF was implemented to estimate the winding resistance, and the experimental results were compared to that of the EKF. It was demonstrated that both of the EK-SVSF and the EKF produced accurate estimates at normal condition and faulty condition when the model of the motor was known. In the presence of the modeling errors, however, the EKF's performance significantly degraded, while the EK-SVSF maintained its accuracy. Moreover, the VBL width of the EK-SVSF

was found to be a secondary indicator for modeling uncertainties. In summary, the EK-SVSF was shown to be a valuable and effective tool for the fault detection and diagnosis of BLDC motors.

7.2 Recommendations and Future Work

In this research, bearing faults representing the mechanical elements of the motor and stator winding faults from the electrical elements of the motor were studied. For mechanical faults, further studies should involve applying the proposed methods on fault diagnosis of all components of the motor. In addition, the influence of the external load on fault diagnosis should be investigated. In terms of parameter estimation of the motor, further studies should involve the implementation of the EK-SVSF on other types of electric motors, such as induction and switched reluctance motors.

Appendix

1. Experimental Setup

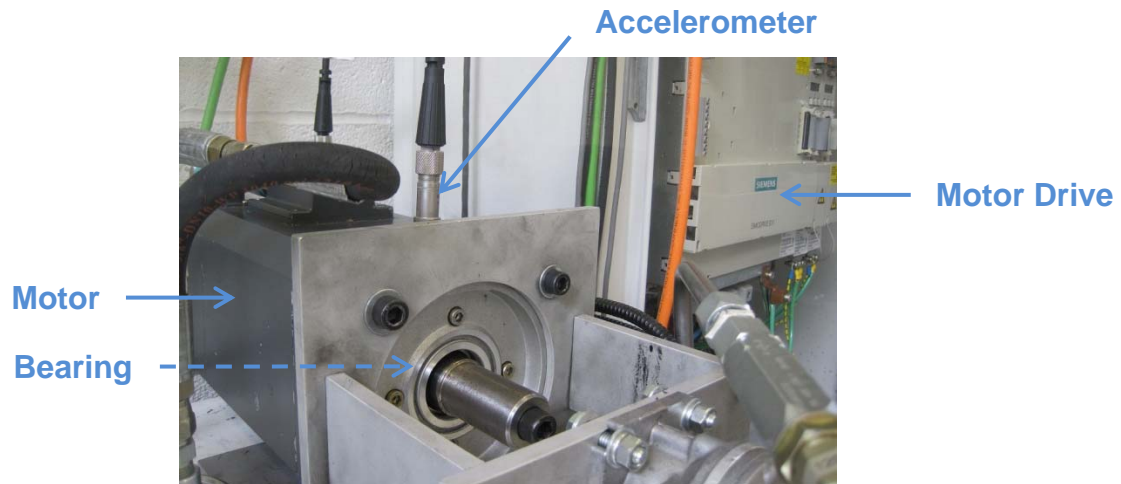


Figure 90 The Permanent Magnet Brushless DC Motor

The Permanent Magnet Brushless DC Motor used in this research is shown in Figure 90, with specifications listed in Table 21.

Table 21 Motor construction parameters

Motor Parameter	Symbol	Value
Rated Speed	ω_r	3000 rpm
Number of poles	P	8
Moment of Inertia	J	$4.8 \times 10^{-3} \text{ kgm}^2$
Torque Constant	K_T	1.52 Nm/A
Voltage Constant	K_e	0.77 V/(rad/s)
Winding Resistance	R	0.5 Ohm
Field Inductance	L_s	$4.8 \times 10^{-3} \text{ H}$

The motor was controlled by Siemens's *SimoDrive 611* system, as shown in Figure 91.



Figure 91 Architecture of fault diagnosis scheme

A built-in absolute encoder was used for rotor position and speed measurement, with a resolution of 2048 lines per revolution. Bearing faults were simulated by replacing the bearing in front of the motor with faulty ones of the same type. An accelerometer (AC240-1D) was mounted on the casing of the motor for vibration measurement, as shown in Figure 90. A data acquisition board (NI PCI-6229) was used along with a built-in anti-aliasing filter for data collection.

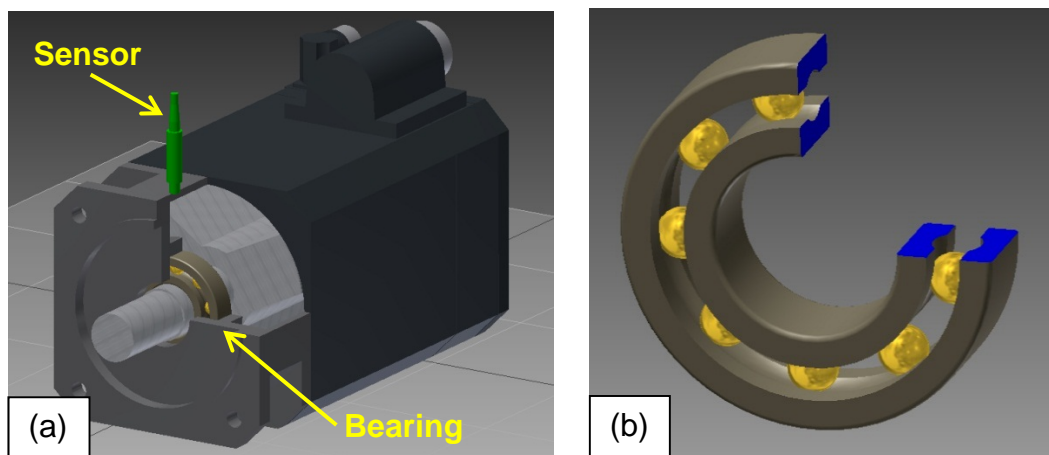


Figure 92 (a) Inventor model of the test motor; (b) Inventor model of the test bearing

The ball bearings used for fault simulation were of the type NACHI-6207NSE.

The dimensions of the test bearing are provided in Table 22, and are marked in Figure 93.

Table 22 Bearing Parameters

Bearing Parameter	Symbol	Value
Model Number	N. O.	6207NSE
Outer Diameter	D	72 [mm]
Inner Diameter	d	35 [mm]
Width	B	17 [mm]
Number of Rolling Balls	N_b	11
Contact Angle	θ	0 [degree]

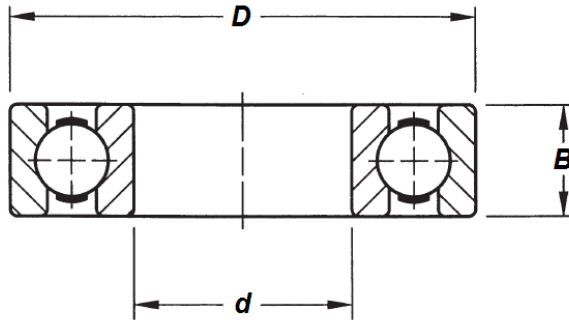


Figure 93 Dimensions of a ball bearing

Four bearing health conditions were considered: normal condition, outer race fault, inner race fault and the presence of both inner and outer race fault. The bearing faults were physically simulated by creating small dents on the inner or outer races with electro-chemical etching method.

The measurement of vibration was recorded at a range of operating conditions and speeds. A Piezoelectric accelerometer was chosen for vibration

measurement due to its small size, durability, low cost, wide frequency range and linearity. Its specifications are listed in Table 23. Vibration signals were recorded during normal motor operation using the accelerometer mounted on the motor casing near a faulty bearing. The mounting of the accelerometer is important as the high frequency response is directly affected by the mounting technique. The greater the contacting surface, the richer is the high frequency content of the measured signal. In order to utilize the entire frequency range and maximizing the information content in the measurement, the sensor was mounted by screwing it into the casing of the motor, as shown in Figure 94.

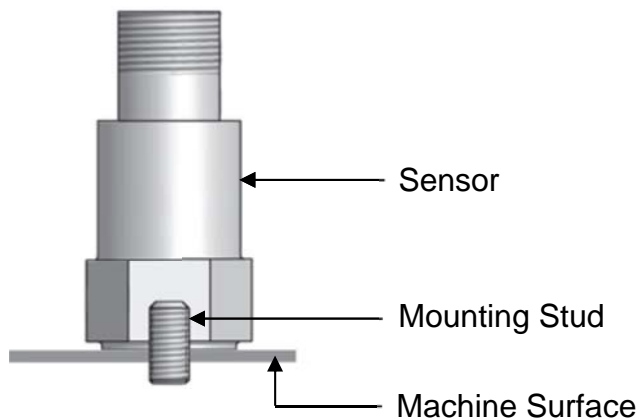


Figure 94 Mounting technique [127]

Table 23 Accelerometer specification

Performance Specification	Values
Sensitivity (+5%)	100 [mV/g]
Frequency Response (+/-3dB)	0.6-25,000 [Hz]
Dynamic Range	+/-50 [g]

Settling Time (20°C)	< 2.5 [sec]
Power Requirement	18-30 [VDC], 2-10 [mA]
Bias Output Voltage	7-14 [VDC]
Temperature Range	-50 to 121 [°C]
Sensing Element	PZT Ceramic
Sensing Structure	Shear Mode
Resonant Frequency	34000 Hz

Motor vibration can be affected by operating conditions influenced by their rotational speed, load and temperature. These factors were considered when designing the experiments. During the tests conducted in this research, the motor was running at two pre-defined speeds with no load. A continuous driving cycle was used for validating and evaluating the effectiveness of the fault diagnosis scheme. The test motor was air-cooled. In order to alleviate the influence of temperature variation, a “warm-up” of 10 minutes was performed prior to the beginning of each test, with the motor running at a constant speed of 3000 RPM. Nonetheless, the temperature was later found to have little influence on the vibration data.

The data acquisition (DAQ) device used in this study was the *National Instruments* PCI-6229 (16-Bit, 833 kS/s, 32 Analog Inputs), with detailed specifications summarized in Table 24. The analog voltage output from the sensor was discretized by a 16-bit analog-to-digital (ADC) function. The 16-bit

ADC card of this system can support maximum sampling frequency of 833 kHz per channel with a resolution of 0.3 mV.

Table 24 Specifications of data acquisition card

Performance Specification	Values
Number of Analog Inputs (AI)	32
Analog Input Resolution	16 [bits]
Number of Analog Outputs (AO)	4
AO Resolution	16 [bits]
Max AO Rate	833 [kS/s]
AO Range	+/-10 [V]
Digital I/O	48
Correlated (clocked) DIO	32 [Hz] to 1 [MHz]
Maximum Sample Rate (AI)	250 [kS/s]
Update Rate (AO)	833 [kS/s]
Maximum Voltage Range Accuracy (AI)	3100 [μ V]

Sampling rate is an important consideration in data acquisition systems. The sampling rate should be set high enough to capture the maximum frequency component of interest contained in the signal. Nyquist frequency is half the sampling frequency of a discrete signal processing system and is the highest frequency that can be extracted from a discretized signal. In this research, the frequency range of interest was 0 - 4 kHz, and the sampling rate chosen was 10

kHz. The data acquisition time was set to 10 seconds to ensure enough samples were captured for analysis. This acquisition length yielded 100,000 samples per test.

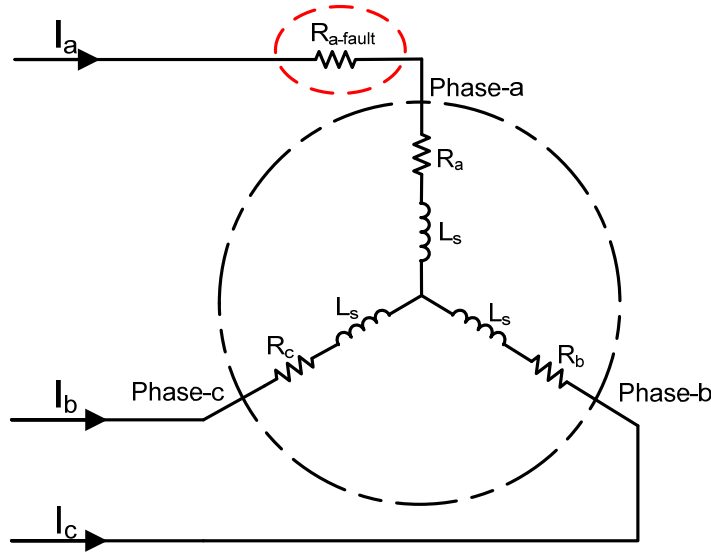


Figure 95 Simplified stator circuit model with faulty resistance in one phase

Winding resistance fault was simulated by adding an external resistor of 0.5 Ohm in series to one of the windings in series. Figure 95 shows the simplified circuit diagram of the stator winding with an added resistor in one of the three phases. In order to reduce aliasing noise, measurements were pre-filtered by a built-in anti-aliasing filter with a cut-off frequency of 500 Hz. Current and voltage measurements were acquired by using a Yokogawa WT1800 power analyzer. This power analyzer was capable of simultaneously measuring the currents and voltages of all of the three phases of the motor with a bandwidth of 5 MHz and an accuracy of $\pm 0.1\%$.

2. The Kalman Filter without Artificial Measurements

As a comparison to the performance of Kalman Filter implemented with artificial measurements in Chapter 6, no artificial measurements were used by the Kalman Filter in this section. Accordingly, the measurement matrix C for KF becomes,

$$C = \begin{bmatrix} 1 & 0 & 0 & 0 & 0 & 0 \\ 0 & 1 & 0 & 0 & 0 & 0 \\ 0 & 0 & 1 & 0 & 0 & 0 \end{bmatrix}$$

Other than C , all filter parameters, such as Q and R , were kept the same as those used in Section 6.2 (Winding Resistance Fault). The estimation results are provided as follows.

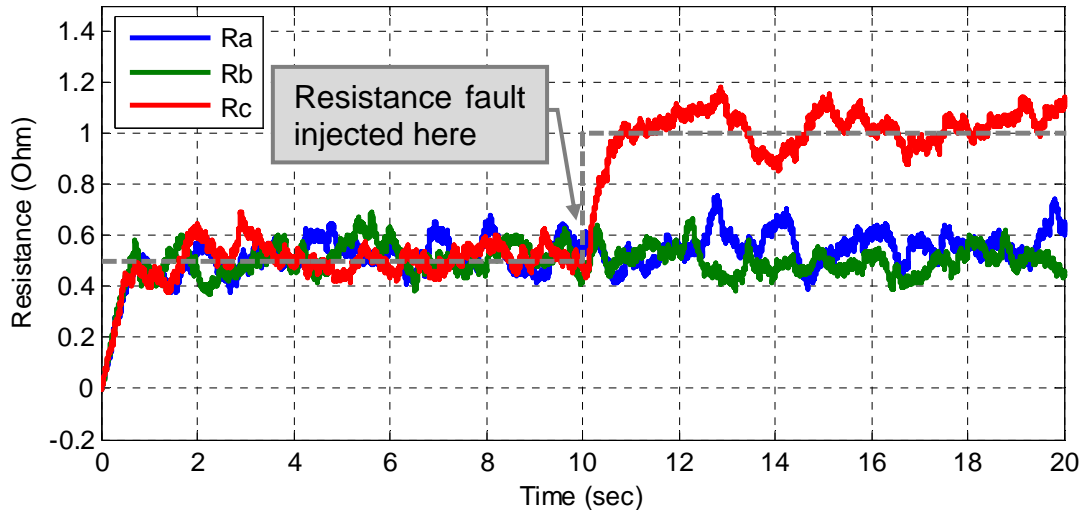


Figure 96 Estimation of phase resistance using Extended Kalman Filter (EKF)

Apparently, the estimates of phase resistance shown in Figure 96 have much more fluctuation than those shown in Figure 82. In terms of the root mean

squared error, the RMSE of all three phases provided in Table 25 for this case are also much larger than those in Table 18.

Table 25 Root Mean Square Error of estimated parameters (Winding Resistance Fault)

Filter	R_a	R_b	R_c
EKF	8.984×10^{-2}	7.296×10^{-2}	8.964×10^{-2}

Another example is provided below as a comparison to the case of modeling uncertainties discussed in Section 6.3.

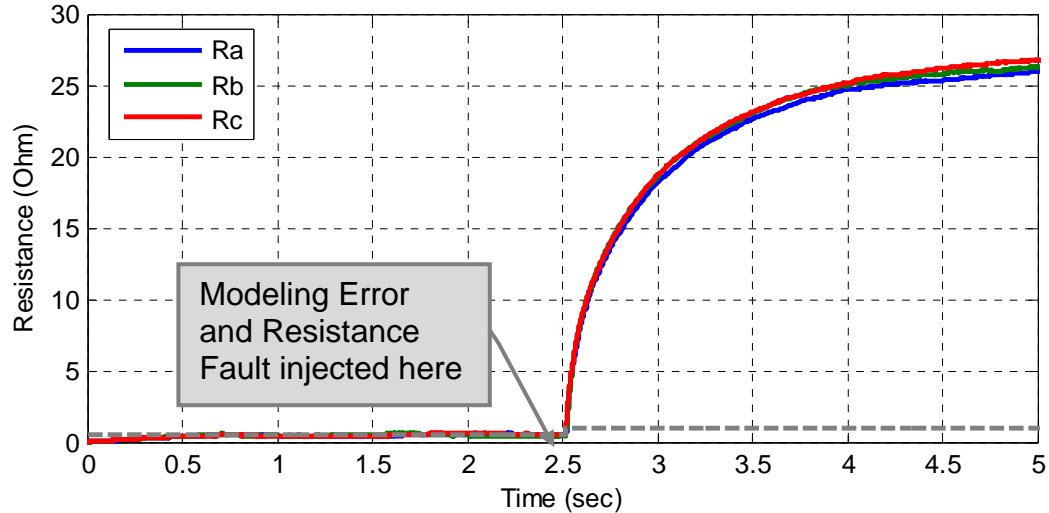


Figure 97 Estimation of phase resistance using Extended Kalman Filter (EKF)

As shown in Figure 97, after the injection of the modeling error at halfway, the estimates of the Kalman Filter diverge from the true state trajectories. This is similar to the results shown in Figure 84, which is due to the sensitivity of KF to modeling uncertainties. The estimation error shown in Figure 97 is, however,

much larger than that of Figure 84. Moreover, the RMSE given in Table 26 are also more than 10 times larger than those of Table 19.

Table 26 Root Mean Square Error of estimated parameters (Modeling Uncertainties)

Filter	R_a	R_b	R_c
EKF	15.42	15.70	15.50

As these two examples indicate, compared with the standard Kalman Filter without Luenberger's approach, the Kalman Filter implemented with artificial measurements in Chapter 6 have smaller estimation errors.

3. Matlab Code

Matlab Code 1: DTCWT_Bearing_Diagnosis.m

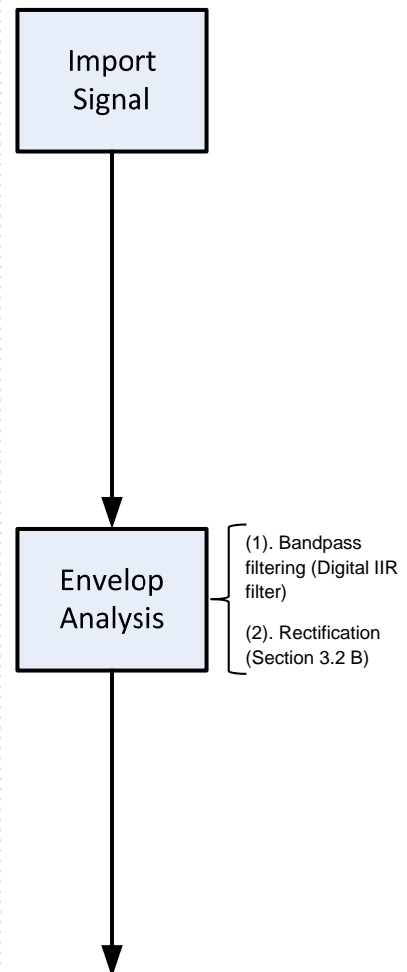
Comments: This is the main program for the bearing diagnosis application.

```
% *****  
% Bearing Faulty Diagnosis based on DTCWT Denoising  
% *****  
clear;clc;close all;
```

```
% ***** Import Signal *****  
% Import Signal  
load 'C:\Users\Peter\Dropbox\JHE105\Bearing Test  
Data\2012March17OuterRace.mat';  
% Define faulty bearing signal  
data1 = acc1_RPM2000_faulty;  
% Define healthy bearing signal  
data2 = acc1_RPM2000_faulty;
```

```
% ***** Measurement Parameters *****  
% Sampling Frequency  
Fs = 10000;  
% Motor Speed  
RPM = 1900;  
% Time Vector  
T = 0:1/Fs:(size(data1,1)-1)/Fs;
```

```
% ***** Envelop Analysis *****  
% Digital IIR Filtering  
% Remove signal mean  
data1 = data1 - mean(data1);  
data2 = data2 - mean(data2);  
data1_bandpassed = data1;  
data2_bandpassed = data2;  
% First Stopband Frequency  
Fstop1 = 500;  
% First Passband Frequency  
Fpass1 = 1000;  
% Second Passband Frequency  
Fpass2 = 3000;  
% Second Stopband Frequency  
Fstop2 = 3500;  
% First Stopband Attenuation (dB)  
Astop1 = 30;  
% Passband Ripple (dB)  
Apass = 1;  
% Second Stopband Attenuation (dB)  
Astop2 = 40;  
% Band to match exactly  
match = 'stopband';
```

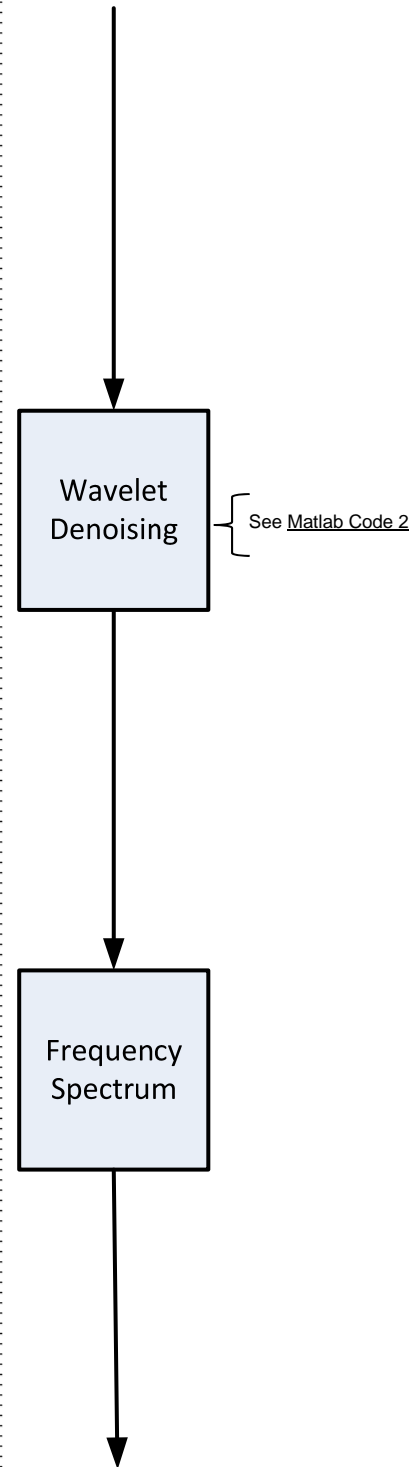


```
% Filter parameters
h = fdesign.bandpass(Fstop1, Fpass1, Fpass2, Fstop2,
Astop1, Apass, Astop2, Fs);
% Designed digital filter
Hd = design(h, 'butter', 'MatchExactly', match);
% Filtered signals
data1_bandpassed =
filtfilt(Hd.sosMatrix,Hd.ScaleValues,data1);
data2_bandpassed =
filtfilt(Hd.sosMatrix,Hd.ScaleValues,data2);
% Rectification
dataF = abs(data1_bandpassed);
dataH = abs(data2_bandpassed);

% ***** DTCWT-based Signal Denoising *****
% Length of signal after extension
ExtedData = 15535;
% Extended signal
dataF_ext = wextend('1','per',dataF,ExtedData);
dataH_ext = wextend('1','per',dataH,ExtedData);
% Filtered signal
dataF_d = denoising_dtdwt(dataF_ext,5,4*50);
dataH_d = denoising_dtdwt(dataH_ext,5,4*50);
% Extract signal from extension
dataF_d = dataF_d(15536:15535+length(data1));
dataH_d = dataH_d(15536:15535+length(data2));

% ***** Frequency Spectrum *****
% Window size
WINDOW = 51200/2;
% Number of overlapping samples
NOVERLAP = 0;
% Normalized frequencies
F = 1024*30;
% Power Spectral Density of original signal
[Power_F,Freq_F] =
pwelch(dataF_ext,WINDOW,NOVERLAP,F,Fs);
[Power_H,Freq_H] =
pwelch(dataH_ext,WINDOW,NOVERLAP,F,Fs);
% Power Spectral Density of DTCWT-filtered signal
[Power_F_d,Freq_F_d] =
pwelch(dataF_d,WINDOW,NOVERLAP,F,Fs);
[Power_H_d,Freq_H_d] =
pwelch(dataH_d,WINDOW,NOVERLAP,F,Fs);
% Power Spectral Density of digital filtered signal
[Power_F_filtfilt,Freq_F_filtfilt] =
pwelch(dataF_filtfilt,WINDOW,NOVERLAP,F,Fs);

% ***** Output Display *****
% Ball Passing Frequency of Outer race and Inner Race
BPFO_OuterRace = [0.0594*[1:5]*RPM;
round(Fs./((0.0594*[1:5]*RPM)))]
BPFO_InnerRadius = [0.0906*[1:5]*RPM;
round(Fs./((0.0906*[1:5]*RPM)))]
% Kurtosis
```



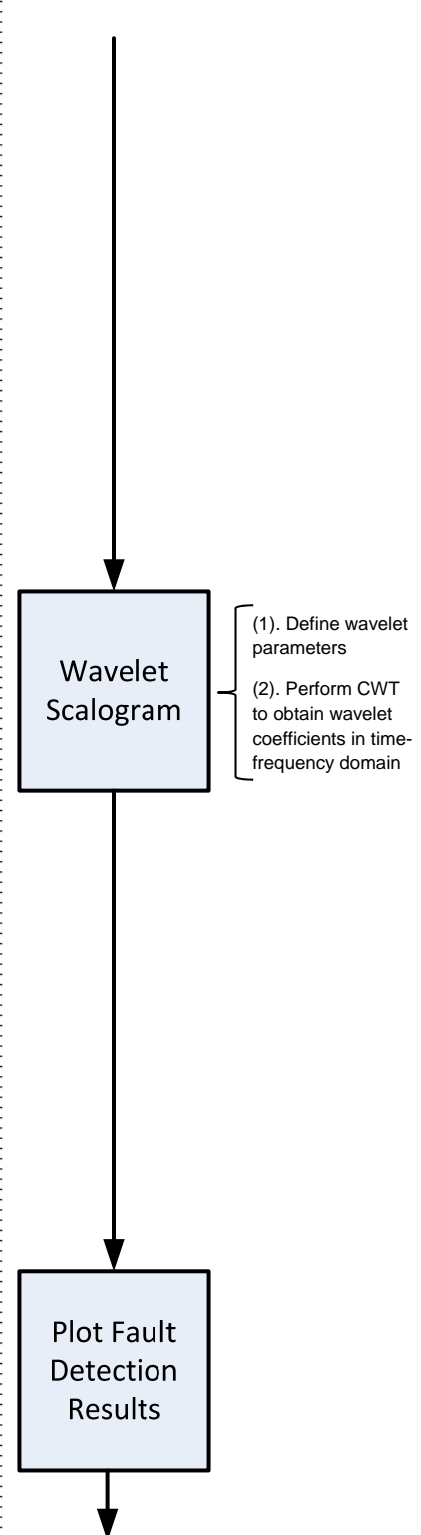

```

Kurtosis = [kurtosis(data1(1000:end-1000));
kurtosis(data2(1000:end-
1000));kurtosis(dataF_d(1000:end-1000));
kurtosis(dataF_filtfilt(1000:end-1000));
kurtosis(dataH_d(1000:end-1000))];
% Display Kurtosis
Kurtosis = [['Raw faulty          ','Raw healthy
','Denoised faulty          ','IIR faulty          ','Denoised
healthy          '],num2str(Kurtosis)]

% ***** Wavelet Scalogram *****
% Assign signal
data_scalog = dataF_d(00001:100001);
T_scalog = T(00001:100001);
% Frequency Axis Limit
FreqLimit =
[BPFO_OuterRace(1,1)*0.53,BPFO_InnerRace(1,1)*1.05];
% Define wavelet function, analytic morlet wavelet,
length = 80
WAV = {'morl',80};
% Scale-to-Frequency factor
MorletFourierFactor = 4*pi/(WAV{2}+sqrt( 2+WAV{2}^2));
% Frequency resolution
Resolution = 4;
% Wavelet Scales
Scales =
round((1./FreqLimit(2))/MorletFourierFactor*Fs):Resoluti
on:round((1./FreqLimit(1))/MorletFourierFactor*Fs)/Fs;
% Frequency ticks for the plot
Freq = 1./(Scales*MorletFourierFactor);
% Freq = Freq/BPFO(1,1);
% BPFs' scale
BPFO_scale =
round((round((1./BPFO_OuterRace(1,1:3))/MorletFourierFac
tor*Fs)/Fs-Scales(1))/(Scales(2)-Scales(1)));
BPFI_scale =
round((round((1./BPFO_InnerRace(1,1:3))/MorletFourierFac
tor*Fs)/Fs-Scales(1))/(Scales(2)-Scales(1)));
% Perform CWT
cwtSIG =
cwtft({data_scalog,1/Fs},'scales',Scales,'wavelet',WAV);

% ***** Plots *****
% Frequency Spectrum
% Freq_F = Freq_F/BPFO(1,1);
figure;
set(gcf,'units','normalized','outerposition',[0 0 0.5
0.5]);
plot(Freq_F,log(Power_F),'-','Color',[1 0.6
0.78],'linewidth',1);
hold all;
plot(Freq_F,log(Power_F_d),'r','linewidth',1);
hold all;
plot(Freq_F,log(Power_F_filtfilt),'g','linewidth',1);
legend('Faulty - raw','Faulty - dtdwt-denoised','Faulty
- zero-phase IIR')

```



```
xlabel('Normalized by Order of (BPFO) Harmonics')
ylabel('Power/frequency (dB/Hz)')
grid on;
title('pwelch spectrum')

% Signal in waveform
figure;
set(gcf,'units','normalized','outerposition',[0 0 0.5
1]);
f1(1) = subplot(211);
plot(T,(dataF),'m','linewidth',1);
hold all;
plot(T,(dataH),'b','linewidth',1);
hold all;
plot(T,(dataH_d),'c','linewidth',2);
legend('faulty - raw','healthy - raw','healthy -
denoised')
xlabel('Time (sec)')
ylabel('Accelerometer Output (V)')
title('measurement')
f1(2) = subplot(212);
plot(T,(dataF),'k','linewidth',1);
hold all;
plot(T,(dataF_d),'r--','linewidth',2);
hold all;
plot(T,(dataF_filtfilt),'g--','linewidth',2);
legend('faulty - raw','faulty - denoised','faulty -
zero-phase IIR')
xlabel('Time (sec)')
ylabel('Accelerometer Output (V)')
title('measurement')
linkaxes([f1(1) f1(2)],'xy');

% Wavelet Scalogram
figure;
set(gcf,'units','normalized','outerposition',[0 0 0.5
0.5]);
SC = wscalogram2('image',normc(abs(cwtsig.cfs)),
'scales',Freq,'ydata',data_scalog,'xdata',T_scalog);
colormap('jet'); % 'hot'
set(gca,'YDir','reverse');
C = caxis;
caxis([0.0e-5, 1.7e-5]);
shading flat;
zoom on;
xlabel('Time (sec)');
ylabel(['Frequency (Hz)']);
for i = 1:1
    line([0 1e5],[BPFO_scale_OuterRace(i)
BPFO_scale_OuterRace(i)],[0 0],'Color',[0 0
0],'Marker','.', 'LineStyle',':')
    line([0 1e5],[BPFO_scale_InnerRace(i)
BPFO_scale_InnerRace(i)],[0 0],'Color',[0 0
0],'Marker','.', 'LineStyle',':')
end
```

Matlab Code 2: denoising_dtdwt.m

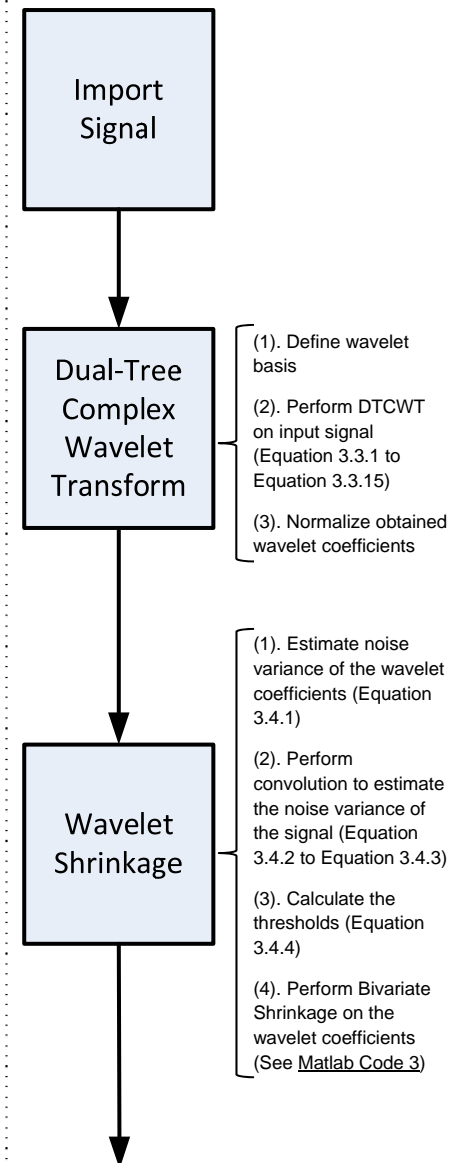
Comments: This function was obtained from a wavelet transform library [94]. Some modifications were applied.

```
% *****
% Dual-Tree Complex Wavelet Transform Denoising
% *****
function y = denoising_dtdwt(x,J,WindowSize)

% ***** Input Signal *****
% Set WindowSize
windowfilt = ones(1,WindowSize)/WindowSize;
% Imaginary number
I=sqrt(-1);
% symmetric extension
L = length(x); % length of the original signal.
N = L+2^J;      % length after extension.
x = symextend(x,2^(J-1));

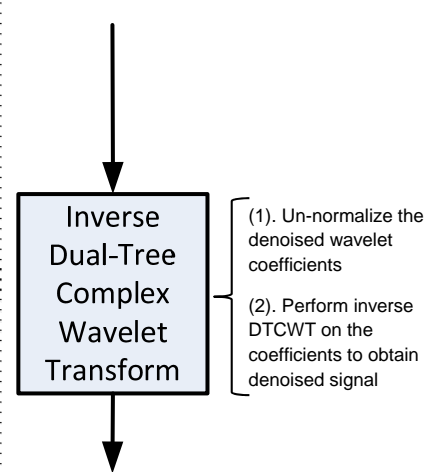
% ***** Dual-Tree Complex Wavelet Transform *****
% Filters for first stage
[Faf, Fsf] = FSfarras;
% Filters after following stage
[af, sf] = dualfilt1;
% DTCWT coefficients
W = dualtree(x, J, Faf, af);
% Normalization matrix
nor = normaliz_coefcalc_dual_tree2(x,J);
% Normalized DTCWT coefficients
W = normcoef(W,J,nor);

% ***** Wavelet Shrinkage (Denoising) *****
% Estimated noise variance
temp = W{1}{1}{1}{1};
Nsig = median(abs(temp(:)))/0.6745;
for scale = 1:J-1
    % Real part of wavelet coefficients
    Y_coef_real = W{scale}{1};
    % imaginary part of wavelet coefficients
    Y_coef_imag = W{scale}{2};
    % Real part of parent coefficients
    Y_parent_real = W{scale+1}{1};
    % imaginary part of parent coefficients
    Y_parent_imag = W{scale+1}{2};
    % Variance estimation
    Wsig = conv((Y_coef_real).^2, windowfilt, 'same');
    Ssig = sqrt(max(Wsig-Nsig(kk).^2,eps));
    % Threshold estimation
    T = abs(1-Nsig(kk)^2./Ssig^2);
    % Magnitude of coefficients
    Y_coef = Y_coef_real+I*Y_coef_imag;
    % Magnitude of parent coefficients
    Y_parent = expand(Y_parent_real) +
    I*expand(Y_parent_imag);
```



```
% Bivariate shrinkage rule
Y_coef_shrked = bishrink(Y_coef,Y_parent,T);
% Denoised coefficients
W{scale}{1} = real(Y_coef_shrked);
W{scale}{2} = imag(Y_coef_shrked);
end

% ***** Inverse DTCWT Transform *****
% Normalization
W = unnormcoef(W,J,nor);
% Reconstructed signal via inverse DTCWT
y = idualtree(W, J, Fsf, sf);
% Extract denoised signal
y_index = 2^(J-1)+1:2^(J-1)+L;
y = y(y_index);
```



Matlab Code 3: bishrink.m

Comments: This function was obtained from a wavelet transform library [94].

```
% *****  
% Bivariate Shrinkage Function  
% *****  
  
function [w1] = bishrink(y1,y2,T)  
% Usage :  
%       [w1] = bishrink(y1,y2,T)  
% INPUT :  
%       y1 - a noisy coefficient value  
%       y2 - the corresponding parent value  
%       T - threshold value  
% OUTPUT :  
%       w1 - the denoised coefficient  
  
R = sqrt(abs(y1).^2 + abs(y2).^2);  
R = R - T;  
R = R .* (R > 0);  
w1 = y1 .* R./(R+T);
```

Matlab Code 4: EKSVSF_Estimation.m

Comments: This is the main program for the bearing diagnosis application.

```
% *****  
% BLDC Motor Estimation (EKF and EK-SVSF)  
% *****  
clear;clc;close all;  
  
% ***** Import Measurements *****  
% Motor Speed [RPM]  
Speed = 1000;  
% Sampling Frequency  
Fs = 1600*1000/50;  
% Sampling Period  
Ts = 1/Fs;  
% Import Measurements  
DATA = YokoDataImport('..\Faulty1_0.50hmPhaseW_1000RPM_50ms\');  
% Voltage Measurements  
Ua = DATA(:,1)';Ub = DATA(:,3)';Uc = DATA(:,5)';  
% Current Measurements  
ia = DATA(:,2)';ib = DATA(:,4)';ic = DATA(:,6)';  
% Rota Angle  
Theta = [DATA(:,7)';DATA(:,8)';DATA(:,9)'];  
% Artificial Measurements (Voltage)  
UaMN = DATA(:,10)';UbMN = DATA(:,12)'; UcMN = DATA(:,14)';  
% Artificial Measurements (Current)  
iaMN = DATA(:,11)'; ibMN = DATA(:,13)'; icMN = DATA(:,15)';  
% Speed Vector [rad/s]  
W = Speed/60*2*pi*ones(1,size(DATA,1));  
% Time Vector  
T = (0:1:size(DATA,1)-1)/Fs;  
  
% ***** Motor Parameters *****  
% Voltage constant [V/rad]  
V = 80.63/1000*(60/2/pi);  
% Winding Resistance  
Rs = 0.5;  
% Winding Inductance  
L = 0.0048;  
  
% ***** Estimation Parameters *****  
% Fault Factor  
FAULT = 0.9;  
% EK-SVSF Switch  
SVSFon = 1;  
% Measurement Covariance  
R = [[1 1 1]*1e-3, [1 1 1]*2e-1]';  
% Process Covariance  
Q = [[1 1 1]*1e-5, [1 1 1]*5e-8]';  
% Boundary Layer Width  
Psi = [[1,1,1]*2, [1,1,1]*2]';  
% Convergence Rate
```

```

Gamma = [0.2; 0.2; 0.2; 0.2; 0.2; 0.2];

% ***** Artificial Measurements *****
diff_ia = [0,ia(2:end)-ia(1:end-1)]*Fs * L;
diff_ib = [0,ib(2:end)-ib(1:end-1)]*Fs * L;
diff_ic = [0,ic(2:end)-ic(1:end-1)]*Fs * L;
% Artificial Measurements of Resistance
ra=(UaMN - diff_ia - V2*Speed)./iaMN;
rb=(UbMN - diff_ib - V2*Speed)./ibMN;
rc=(UcMN - diff_ic - V2*Speed)./icMN;
% Digital Filter
% Passband Frequency
FreqPass = 1.0e-5;
% Stopband Frequency
FreqStop = 3.0e-5;
% Passband Ripple
APass = 8;
% Stopband Attenuation
AStop = 23;
% Designed digital filter
Hd = design(fdesign.lowpass('Fp,Fst,Ap,Ast' , FreqPass,
FreqStop, APass, AStop), 'cheby2');
% Signal extension
ra_temp = [ra(end:-1:1),ra,ra(end:-1:1)];
rb_temp = [rb(end:-1:1),rb,rb(end:-1:1)];
rc_temp = [rc(end:-1:1),rc,rc(end:-1:1)];
% Filtered artificial measurements
ra_f = filtfilt(Hd.sosMatrix,Hd.ScaleValues,ra_temp-
mean(ra_temp)) + mean(ra_temp);
rb_f = filtfilt(Hd.sosMatrix,Hd.ScaleValues,rb_temp-
mean(rb_temp)) + mean(rb_temp);
rc_f = filtfilt(Hd.sosMatrix,Hd.ScaleValues,rc_temp-
mean(rc_temp)) + mean(rc_temp);
% Extracted signal
ra_f = ra_f(1+length(ra):2*length(ra));
rb_f = rb_f(1+length(rb):2*length(rb));
rc_f = rc_f(1+length(rc):2*length(rc));

% ***** Estimation Initialization *****
R = diag(R);
Q = diag(Q);
X_priori = zeros(6,length(T));
X_post = zeros(6,length(T));
err_priori = zeros(6,length(T));
err_post = zeros(6,length(T));
SwitchOn = zeros(1,length(T));
P_priori = cell(1,length(T));
P_post = cell(1,length(T));
P_post2 = cell(1,length(T));
P_post{1} = Q.*diag([10,10,10,3e3,3e3,3e3]);
K_svsf = cell(1,length(T));
K_kalman = cell(1,length(T));
K_KSVSF = cell(1,length(T));
psi = cell(1,length(T));
K_svsf2 = zeros(6,1);
Ia = zeros(1,length(T));

```

```

Ib = zeros(1,length(T));
Ic = zeros(1,length(T));
Ra = 0.0*Rs*ones(1,length(T));
Rb = 0.0*Rs*ones(1,length(T));
Rc = 0.0*Rs*ones(1,length(T));
dA = zeros(6,6);
SwitchOn = 0;
Z = [ia;ib;ic;ra_f;rb_f;rc_f];

% ***** Estimation Loop *****
for k = 1:length(T)-1

    % Model fault injected
    if k == fix(length(DATA)/3) & FAULT,
        V = FAULT*V;
    end
    % Model fault removed
    if k == fix(length(DATA)/3*2) & FAULT,
        V = 1/FAULT*V;
    end

    % A prior estimates
    X_priori(1,k+1) = Ia(k) + (Ts/L)*( Ua(k) - Ra(k)*Ia(k) -
V*W(k)*sin(Theta(1,k)) );
    X_priori(2,k+1) = Ib(k) + (Ts/L)*( Ub(k) - Rb(k)*Ib(k) -
V*W(k)*sin(Theta(2,k)) );
    X_priori(3,k+1) = Ic(k) + (Ts/L)*( Uc(k) - Rc(k)*Ic(k) -
V*W(k)*sin(Theta(3,k)) );
    X_priori(4,k+1) = Ra(k);
    X_priori(5,k+1) = Rb(k);
    X_priori(6,k+1) = Rc(k);

    % Linearized system matrix
    dA(1,:) = [1-(Ts/3/L)*3*Ra(k), 0, 0, (Ts/3/L)*(-3*Ia(k)), 0,
0];
    dA(2,:) = [0, 1-(Ts/3/L)*3*Rb(k), 0, 0, (Ts/3/L)*(-3*Ib(k)),
0];
    dA(3,:) = [0, 0, 1-(Ts/3/L)*3*Rc(k), 0, 0, (Ts/3/L)*(-
3*Ic(k))];
    dA(4,:) = [0, 0, 0, 1, 0, 0];
    dA(5,:) = [0, 0, 0, 0, 1, 0];
    dA(6,:) = [0, 0, 0, 0, 0, 1];

    % Measurement matrix
    H = [1, 0, 0, 0, 0, 0;
0, 1, 0, 0, 0, 0;
0, 0, 1, 0, 0, 0;
0, 0, 0, 1, 0, 0;
0, 0, 0, 0, 1, 0;
0, 0, 0, 0, 0, 1];

    % Linearized measurement matrix
    dH = H;

    % Update estimation error covariance
    P_priori{k+1} = dA * P_post{k} * dA' + Q;

```



```

% A prior estimate error
err_priori(:,k+1) = Z(:,k+1) - X_priori(:,k+1);

% EKF Gain
K_kalman{k+1} = P_priori{k+1} * (dH') * inv(dH *
P_priori{k+1} * dH' + R);
err_post_Kalman(:,k+1) = ( eye(6) - K_kalman{k+1} ) *
err_priori(:,k+1);

% A posteriori innovation convariance
S = dH*P_priori{k+1}*dH' + R;
% Combined error vector
A = abs(err_priori(:,k+1)) + Gamma.*abs(err_post(:,k));
% Varying Boundary Layer
psi{k+1} = inv(inv(diag(A))*dH*P_priori{k+1}*dH'/S);
% Saturation function
for kk=1:6
    temp = sign(abs(err_priori(kk,k+1))-Psi(kk))+1;
    if temp
        Sat(kk,k+1) = sign(err_priori(kk,k+1));
    else
        Sat(kk,k+1) = (err_priori(kk,k+1) ./ Psi(kk));
    end
end

% SVSF gain
K_svsf{k+1} = dH * diag((abs(err_priori(:,k+1)) + Gamma .*
abs(err_post(:,k))) .* Sat(:,k+1)) *
inv(diag(err_priori(:,k+1)));

% EKF/EK-SVSF switch
for ii=1:3,
    psi_Indicator(ii) = sign(abs(psi{k+1}(ii,ii)) -
Psi(ii))+1;
end
SwitchOn(k+1) =
(psi_Indicator(1)||psi_Indicator(2)||psi_Indicator(3)) & SVSFon;
if SwitchOn(k+1)
    K_KSVSF{k+1} = K_svsf{k+1};
else
    K_KSVSF{k+1} = K_kalman{k+1};
end

% A Posteriori estimation
X_post(:,k+1) = X_priori(:,k+1) + K_KSVSF{k+1} *
err_priori(:,k+1);

% A posteriori error convariance
P_post{k+1} = ( eye(6) - K_KSVSF{k+1}*dH ) * P_priori{k+1} *
( eye(6) - K_KSVSF{k+1}*dH )' + K_KSVSF{k+1} * R *
(K_KSVSF{k+1})';
P_post2(:,k) = diag(P_post{k});

% A posteriori estimate error%
err_post(:,k+1) = Z(:,k+1) - X_post(:,k+1);

Ia(k+1) = X_post(1,k+1);
Ib(k+1) = X_post(2,k+1);

```

```

Ic(k+1) = X_post(3,k+1);
Ra(k+1) = X_post(4,k+1);
Rb(k+1) = X_post(5,k+1);
Rc(k+1) = X_post(6,k+1);
end

% ***** plot *****
% Covariance
figure;
set(gcf,'units','normalized','outerposition',[0.00 0.00 0.5 1]);
f2(1) = subplot(211);
plot(T,P_post2([1:3],:),'linewidth',2);
legend('Cov-Ia','Cov-Ib','Cov-Ic');
ylabel('Covariance');
xlabel('Time (sec)');
temp=axis;temp(2)=floor(T(end));axis(temp);
f2(2) = subplot(212);
plot(T,P_post2([4:6],:),'linewidth',2);
legend('Cov-Ra','Cov-Rb','Cov-Rc');
ylabel('Covariance');
xlabel('Time (sec)');
temp=axis;temp(2)=floor(T(end));axis(temp);
linkaxes(f2,'x');

% Ua Ub Uc, Ia Ib Ic
figure;
set(gcf,'units','normalized','outerposition',[0 0 0.5 1]);
f2(1) = subplot(211);
plot(T,[Ua;Ub;Uc]);
legend('Ua','Ub','Uc');
ylabel('Phase Voltage (V)');
xlabel('Time (sec)');
f2(2) = subplot(212);
plot(T,X_post(1,:));hold all;
plot(T,X_post(2,:));hold all;
plot(T,X_post(3,:));
legend('Ia','Ib','Ic');
ylabel('Line Current (V)');
xlabel('Time (sec)');
linkaxes(f2,'x');
temp=axis;temp(2)=floor(T(end));axis(temp);

% Psi_Ia, Psi_Ib, Psi_Ic
figure;
set(gcf,'units','normalized','outerposition',[0.00 0.00 0.5 1]);
f(1) = subplot(211);
for i = 2:length(psi), psi_plot(:,i) = diag(psi{i}); end
plot(T,psi_plot([1:3],:));hold all;
plot(T,Psi(1)*ones(1,length(T)),'k--','linewidth',2);
legend('Psi-Ia','Psi-Ib','Psi-Ic');
xlabel('Time (sec)');
ylabel('Value');
temp=axis;temp(2)=floor(T(end));temp(4) = 3.5;axis(temp);
f(2) = subplot(212);
plot(T,psi_plot([4:6],:));hold all;
plot(T,Psi(4)*ones(1,length(T)),'k--','linewidth',2);
legend('psi ra','psi rb','psi rc')

```

```
xlabel('Time (sec)');
ylabel('Value');
linkaxes(f,'x');
temp=axis;temp(2)=floor(T(end));temp(4) = temp(4);axis(temp);
set(gcf,'units','normalized','outerposition',[0.00 0 0.5 1]);

% Ra, Rb, Rc
figure;
set(gcf,'units','normalized','outerposition',[0.00 0.00 0.5
0.5]);
plot(T,X_post(4,:), 'linewidth',2);hold all;
plot(T,X_post(5,:), 'linewidth',2);hold all;
plot(T,X_post(6,:), 'linewidth',2);hold all;
legend('Ra','Rb','Rc');
xlabel('Time (sec)');
ylabel('Resistance (Ohm)');
grid on;
temp=axis;temp(2)=floor(T(end));temp(4) = 1;axis(temp);

% Root Mean Square Error
RMSE_A = sqrt(mean((X_post(4,1:end)-Nominal1(1,1:end)).^2));
RMSE_B = sqrt(mean((X_post(5,1:end)-Nominal1(1,1:end)).^2));
RMSE_C = sqrt(mean((X_post(6,1:end)-Nominal1(1,1:end)).^2));
display(['RMSE - Ra: ',num2str([RMSE_A])]);
display(['RMSE - Rb: ',num2str([RMSE_B])]);
display(['RMSE - Rc: ',num2str([RMSE_C])]);
```

Bibliography

- [1] R. Krishnan, *Electric motor drives: modeling, analysis, and control*: Prentice Hall, 2001.
- [2] Microchip Technology Inc, "AN885 - Brushless DC (BLDC) Motor Fundamentals," 2003.
- [3] M. Ehsani, Y. Gao, and A. Emadi, *Modern Electric, Hybrid Electric, and Fuel Cell Vehicles: Fundamentals, Theory, and Design, Second Edition*: Taylor & Francis, 2009.
- [4] Koyo, "Ball bearing failures, causes and countermeasures."
- [5] R. B. Randall and J. Antoni, "Rolling element bearing diagnostics-A tutorial," *Mechanical Systems and Signal Processing*, vol. 25, pp. 485-520, Feb 2011.
- [6] N. B. Corporation, "An Introduction to Ball Bearings," 1994.
- [7] A. B. Limited. What is a Bearing.
- [8] S. Abbasion, A. Rafsanjani, A. Farshidianfar, and N. Irani, "Rolling element bearings multi-fault classification based on the wavelet denoising and support vector machine," *Mechanical Systems and Signal Processing*, vol. 21, pp. 2933-2945, Oct 2007.
- [9] A. Rafsanjani, S. Abbasion, A. Farshidianfar, and H. Moeenfar, "Nonlinear dynamic modeling of surface defects in rolling element bearing systems," *Journal of Sound and Vibration*, vol. 319, pp. 1150-1174, Jan 23 2009.
- [10] E. B. Company, "Bearing Failure Analysis," ed.
- [11] S. Lacey, "The Role of Vibration Monitoring in Predictive Maintenance," *Engineering Manager Schaeffler (UK) Limited*, 2010.
- [12] M. Walker, *The Diagnosing of Trouble in Electrical Machines*. London, U.K.: Library Press, 1924.
- [13] P. J. Zhang, Y. Du, T. G. Habetler, and B. Lu, "A Survey of Condition Monitoring and Protection Methods for Medium-Voltage Induction Motors,"

- Ieee Transactions on Industry Applications*, vol. 47, pp. 34-46, Jan-Feb 2011.
- [14] Z. K. Peng and F. L. Chu, "Application of the wavelet transform in machine condition monitoring and fault diagnostics: a review with bibliography," *Mechanical Systems and Signal Processing*, vol. 18, pp. 199-221, Mar 2004.
- [15] A. Gandhi, T. Corrigan, and L. Parsa, "Recent Advances in Modeling and Online Detection of Stator Interturn Faults in Electrical Motors," *Ieee Transactions on Industrial Electronics*, vol. 58, pp. 1564-1575, May 2011.
- [16] S. Nandi, H. A. Toliyat, and X. D. Li, "Condition monitoring and fault diagnosis of electrical motors - A review," *Ieee Transactions on Energy Conversion*, vol. 20, pp. 719-729, Dec 2005.
- [17] A. H. Bonnett and C. Yung, "Increased efficiency versus increased reliability - A comparison of pre-EPA, EPA, and premium-efficient motors," *Ieee Industry Applications Magazine*, vol. 14, pp. 29-36, Jan-Feb 2008.
- [18] J. A. Antonino-Daviu, M. Riera-Guasp, J. R. Folch, and M. P. M. Palomares, "Validation of a new method for the diagnosis of rotor bar failures via wavelet transform in industrial induction machines," *Ieee Transactions on Industry Applications*, vol. 42, pp. 990-996, Jul-Aug 2006.
- [19] B. Ayhan, M. Y. Chow, and M. H. Song, "Multiple discriminant analysis and neural-network-based monolith and partition fault-detection schemes for broken rotor bar in induction motors," *Ieee Transactions on Industrial Electronics*, vol. 53, pp. 1298-1308, Aug 2006.
- [20] A. Ordaz-Moreno, R. D. Romero-Troncoso, J. A. Vite-Frias, J. R. Rivera-Gillen, and A. Garcia-Perez, "Automatic online diagnosis algorithm for broken-bar detection on induction motors based on discrete wavelet transform for FPGA implementation," *Ieee Transactions on Industrial Electronics*, vol. 55, pp. 2193-2202, May 2008.
- [21] S. Bachir, S. Tnani, J. C. Trigeassou, and G. Champenois, "Diagnosis by parameter estimation of stator and rotor faults occurring in induction machines," *Ieee Transactions on Industrial Electronics*, vol. 53, pp. 963-973, Jun 2006.
- [22] M. Riera-Guasp, J. A. Antonino-Daviu, J. Roger-Folch, and M. P. M. Palomares, "The use of the wavelet approximation signal as a tool for the

- diagnosis of rotor bar failures," *Ieee Transactions on Industry Applications*, vol. 44, pp. 716-726, May-Jun 2008.
- [23] G. Didier, E. Ternisien, O. Caspary, and H. Razik, "Fault detection of broken rotor bars in induction motor using a global fault index," *Ieee Transactions on Industry Applications*, vol. 42, pp. 79-88, Jan-Feb 2006.
- [24] T. T. O.G. Gustaffson, "Detection of damage of assembled rolling bearings," *ASME Transaction* 5, pp. 197-209, 1962.
- [25] T. A. Harris and M. N. Kotzalas, *Advanced Concepts of Bearing Technology*. Taylor & Francis, 2006.
- [26] H. Qiu, J. Lee, J. Lin, and G. Yu, "Wavelet filter-based weak signature detection method and its application on rolling element bearing prognostics," *Journal of Sound and Vibration*, vol. 289, pp. 1066-1090, Feb 2006.
- [27] Z. K. Peng, P. W. Tse, and F. L. Chu, "A comparison study of improved Hilbert-Huang transform and wavelet transform: Application to fault diagnosis for rolling bearing," *Mechanical Systems and Signal Processing*, vol. 19, pp. 974-988, Sep 2005.
- [28] Y. T. Su and Y. T. Sheen, "ON THE DETECTABILITY OF ROLLER BEARING DAMAGE BY FREQUENCY-ANALYSIS," *Proceedings of the Institution of Mechanical Engineers Part C-Journal of Mechanical Engineering Science*, vol. 207, pp. 23-32, 1993.
- [29] V. Purushotham, S. Narayanan, and S. A. N. Prasad, "Multi-fault diagnosis of rolling bearing elements using wavelet analysis and hidden Markov model based fault recognition," *Ndt & E International*, vol. 38, pp. 654-664, Dec 2005.
- [30] Y. Pan, J. Chen, and L. Guo, "Robust bearing performance degradation assessment method based on improved wavelet packet-support vector data description," *Mechanical Systems and Signal Processing*, vol. 23, pp. 669-681, Apr 2009.
- [31] N. Sawalhi, R. B. Randall, and H. Endo, "The enhancement of fault detection and diagnosis in rolling element bearings using minimum entropy deconvolution combined with spectral kurtosis," *Mechanical Systems and Signal Processing*, vol. 21, pp. 2616-2633, Aug 2007.

- [32] R. Q. Yan and R. X. Gao, "Approximate Entropy as a diagnostic tool for machine health monitoring," *Mechanical Systems and Signal Processing*, vol. 21, pp. 824-839, Feb 2007.
- [33] Y. Yang, D. J. Yu, and J. S. Cheng, "A fault diagnosis approach for roller bearing based on IMF envelope spectrum and SVM," *Measurement*, vol. 40, pp. 943-950, Nov-Dec 2007.
- [34] I. S. Bozchalooi and M. Liang, "A joint resonance frequency estimation and in-band noise reduction method for enhancing the detectability of bearing fault signals," *Mechanical Systems and Signal Processing*, vol. 22, pp. 915-933, May 2008.
- [35] S. V. Vaseghi, *Advanced Digital Signal Processing and Noise Reduction, 4th Edition*: Wiley, 2009.
- [36] R. Q. Yan and R. X. Gao, "Multi-scale enveloping spectrogram for vibration analysis in bearing defect diagnosis," *Tribology International*, vol. 42, pp. 293-302, Feb 2009.
- [37] I. A. A. N.G. NIKOLAOU, "DEMODULATION OF VIBRATION SIGNALS GENERATED BY DEFECTS IN ROLLING ELEMENT BEARINGS USING COMPLEX SHIFTED MORLET WAVELETS," *Mechanical Systems and Signal Processing*, vol. 16, pp. 677-694, 2002.
- [38] M. F. Alexandre Azzalini, Kai Schneider, "Nonlinear wavelet thresholding - A recursive method to determine the optimal denoising threshold," 2005.
- [39] S. Mallat, *A Wavelet Tour of Signal Processing, Third Edition: The Sparse Way*: Academic Press, 2008.
- [40] Z. Li, Z. J. He, Y. Y. Zi, and Y. X. Wang, "Customized wavelet denoising using intra- and inter-scale dependency for bearing fault detection," *Journal of Sound and Vibration*, vol. 313, pp. 342-359, Jun 2008.
- [41] L. Sendur and I. W. Selesnick, "Bivariate shrinkage with local variance estimation," *Signal Processing Letters, IEEE*, vol. 9, pp. 438-441, 2002.
- [42] H. B. Hong and M. Liang, "K-hybrid: A kurtosis-based hybrid thresholding method for mechanical signal denoising," *Journal of Vibration and Acoustics-Transactions of the Asme*, vol. 129, pp. 458-470, Aug 2007.

- [43] A. Djebala, N. Ouelaa, and N. Hamzaoui, "Detection of rolling bearing defects using discrete wavelet analysis," *Meccanica*, vol. 43, pp. 339-348, Jun 2008.
- [44] Y. X. Wang, Z. J. He, and Y. Y. Zi, "Enhancement of signal denoising and multiple fault signatures detecting in rotating machinery using dual-tree complex wavelet transform," *Mechanical Systems and Signal Processing*, vol. 24, pp. 119-137, Jan 2010.
- [45] I. W. Selesnick, R. G. Baraniuk, and N. G. Kingsbury, "The dual-tree complex wavelet transform," *Ieee Signal Processing Magazine*, vol. 22, pp. 123-151, Nov 2005.
- [46] A. Barri, A. Doms, and P. Schelkens, "The near shift-invariance of the dual-tree complex wavelet transform revisited," *Journal of Mathematical Analysis and Applications*, vol. 389, pp. 1303-1314, May 2012.
- [47] W. Zhou, B. Lu, T. G. Habetler, and R. G. Harley, "Incipient Bearing Fault Detection via Motor Stator Current Noise Cancellation Using Wiener Filter," *Ieee Transactions on Industry Applications*, vol. 45, pp. 1309-1317, Jul-Aug 2009.
- [48] J. R. Bowler, T. P. Theodoulidis, H. Xie, and Y. Ji, "Evaluation of Eddy-Current Probe Signals Due to Cracks in Fastener Holes," *Ieee Transactions on Magnetics*, vol. 48, pp. 1159-1170, Mar 2012.
- [49] F. Immovilli, M. Cocconcelli, A. Bellini, and R. Rubini, "Detection of Generalized-Roughness Bearing Fault by Spectral-Kurtosis Energy of Vibration or Current Signals," *Ieee Transactions on Industrial Electronics*, vol. 56, pp. 4710-4717, Nov 2009.
- [50] A. Bellini, F. Filippetti, C. Tassoni, and G. A. Capolino, "Advances in Diagnostic Techniques for Induction Machines," *Ieee Transactions on Industrial Electronics*, vol. 55, pp. 4109-4126, Dec 2008.
- [51] W. Zhou, T. G. Habetler, and R. G. Harley, "Bearing Fault Detection Via Stator Current Noise Cancellation and Statistical Control," *Ieee Transactions on Industrial Electronics*, vol. 55, pp. 4260-4269, Dec 2008.
- [52] L. Frosini and E. Bassi, "Stator Current and Motor Efficiency as Indicators for Different Types of Bearing Faults in Induction Motors," *Ieee Transactions on Industrial Electronics*, vol. 57, pp. 244-251, Jan 2010.

- [53] L. Eren and M. J. Devaney, "Bearing damage detection via wavelet packet decomposition of the stator current," *Ieee Transactions on Instrumentation and Measurement*, vol. 53, pp. 431-436, Apr 2004.
- [54] J. H. Jung, J. J. Lee, and B. H. Kwon, "Online diagnosis of induction motors using MCSA," *Ieee Transactions on Industrial Electronics*, vol. 53, pp. 1842-1852, Dec 2006.
- [55] C. Kral, T. G. Habetler, and R. G. Harley, "Detection of mechanical imbalances of induction machines without spectral analysis of time-domain signals," *Ieee Transactions on Industry Applications*, vol. 40, pp. 1101-1106, Jul-Aug 2004.
- [56] Y. Y. He, X. M. Zhang, and M. I. Friswell, "Defect Diagnosis for Rolling Element Bearings Using Acoustic Emission," *Journal of Vibration and Acoustics-Transactions of the Asme*, vol. 131, Dec 2009.
- [57] M. Elforjani and D. Mba, "Accelerated natural fault diagnosis in slow speed bearings with Acoustic Emission," *Engineering Fracture Mechanics*, vol. 77, pp. 112-127, Jan 2010.
- [58] B. Eftekharnnejad, M. R. Carrasco, B. Charnley, and D. Mba, "The application of spectral kurtosis on Acoustic Emission and vibrations from a defective bearing," *Mechanical Systems and Signal Processing*, vol. 25, pp. 266-284, Jan 2011.
- [59] A. Rezaei, A. Dadouche, V. Wickramasinghe, and W. Dmochowski, "A Comparison Study Between Acoustic Sensors for Bearing Fault Detection Under Different Speed and Load Using a Variety of Signal Processing Techniques," *Tribology Transactions*, vol. 54, pp. 179-186, 2011.
- [60] A. M. Al-Ghamd and D. Mba, "A comparative experimental study on the use of acoustic emission and vibration analysis for bearing defect identification and estimation of defect size," *Mechanical Systems and Signal Processing*, vol. 20, pp. 1537-1571, Oct 2006.
- [61] R. M. Tallam, T. G. Habetler, and R. G. Harley, "Experimental testing of a neural-network-based turn-fault detection scheme for induction machines under accelerated insulation failure conditions," *Ieee International Symposium on Diagnostics for Electric Machines, Power Electronics and Drives, Proceedings*, pp. 58-62, 2003.
- [62] L. Romeral, J. C. Urresty, J. R. R. Ruiz, and A. G. Espinosa, "Modeling of Surface-Mounted Permanent Magnet Synchronous Motors With Stator

- Winding Interturn Faults," *Ieee Transactions on Industrial Electronics*, vol. 58, pp. 1576-1585, May 2011.
- [63] K. H. Kim, D. U. Choi, B. G. Gu, and I. S. Jung, "Fault model and performance evaluation of an inverter-fed permanent magnet synchronous motor under winding shorted turn and inverter switch open," *Iet Electric Power Applications*, vol. 4, pp. 214-225, Apr 2010.
- [64] T. Boileau, B. N. Mobarakeh, and F. M. Tabar, "On-line Identification of PMSM Parameters: Model-Reference vs EKF," *2008 Ieee Industry Applications Society Annual Meeting, Vols 1-5*, pp. 1410-1417, 2008.
- [65] S. Bolognani, M. Zigliotto, and K. Unterkofer, "On-line parameter commissioning in sensorless PMSM drives," in *Industrial Electronics, 1997. ISIE '97., Proceedings of the IEEE International Symposium on*, 1997, pp. 480-484 vol.2.
- [66] S. Bolognani, L. Tubiana, and M. Zigliotto, "Extended Kalman filter tuning in sensorless PMSM drives," *Ieee Transactions on Industry Applications*, vol. 39, pp. 1741-1747, Nov-Dec 2003.
- [67] L. Liu and D. A. Cartes, "On-line identification and robust fault diagnosis for nonlinear PMSM drives," *ACC: Proceedings of the 2005 American Control Conference, Vols 1-7*, pp. 2023-2027, 2005.
- [68] M. Khov, J. Regnier, and J. Faucher, "Monitoring of Turn Short-Circuit Faults in Stator of PMSM in Closed Loop by On-line Parameter Estimation," *2009 Ieee International Symposium on Diagnostics for Electric Machines, Power Electronics and Drives*, pp. 60-65, 2009.
- [69] O. Moseler and R. Isermann, "Application of model-based fault detection to a brushless DC motor," *Ieee Transactions on Industrial Electronics*, vol. 47, pp. 1015-1020, Oct 2000.
- [70] J. Cusido, L. Romeral, J. A. Ortega, J. A. Rosero, and A. G. Espinosa, "Fault detection in induction machines using power spectral density in wavelet decomposition," *Ieee Transactions on Industrial Electronics*, vol. 55, pp. 633-643, Feb 2008.
- [71] P. Neti and S. Nandi, "Stator Interturn Fault Detection of Synchronous Machines Using Field Current and Rotor Search-Coil Voltage Signature Analysis," *Ieee Transactions on Industry Applications*, vol. 45, pp. 911-920, May-Jun 2009.

- [72] C. Bianchini, E. Fornasiero, T. N. Matzen, N. Bianchi, and A. Bellini, "Fault detection of a five-phase Permanent-Magnet machine," in *Industrial Electronics, 2008. IECON 2008. 34th Annual Conference of IEEE*, 2008, pp. 1200-1205.
- [73] M. Seera, C. P. Lim, D. Ishak, and H. Singh, "Fault Detection and Diagnosis of Induction Motors Using Motor Current Signature Analysis and a Hybrid FMM-CART Model," *Ieee Transactions on Neural Networks and Learning Systems*, vol. 23, pp. 97-108, Jan 2012.
- [74] J. Cusido, L. Romeral, J. A. Ortega, A. Garcia, and J. Riba, "Signal Injection as a Fault Detection Technique," *Sensors*, vol. 11, pp. 3356-3380, Mar 2011.
- [75] Q. Wu and S. Nandi, "Fast Single-turn Sensitive Stator Inter-turn Fault Detection of Induction Machines Based on Positive and Negative Sequence Third Harmonic Components of Line Currents," *2008 Ieee Industry Applications Society Annual Meeting, Vols 1-5*, pp. 899-906, 2008.
- [76] S. M. A. Cruz and A. J. M. Cardoso, "Multiple reference frames theory: A new method for the diagnosis of stator faults in three-phase induction motors," *Ieee Transactions on Energy Conversion*, vol. 20, pp. 611-619, Sep 2005.
- [77] S. Cheng, P. Zhang, and T. G. Habetler, "An Impedance Identification Approach to Sensitive Detection and Location of Stator Turn-to-Turn Faults in a Closed-Loop Multiple-Motor Drive," *Industrial Electronics, IEEE Transactions on*, vol. 58, pp. 1545-1554, 2011.
- [78] F. Briz, M. W. Degner, A. Zamarron, and J. M. Guerrero, "On-line stator winding fault diagnosis in inverter-fed AC machines using high frequency signal injection," *Conference Record of the 2002 Ieee Industry Applications Conference, Vols 1-4*, pp. 2094-2101, 2002.
- [79] F. Briz, M. W. Degner, P. Garcia, and A. B. Diez, "High-Frequency Carrier-Signal Voltage Selection for Stator Winding Fault Diagnosis in Inverter-Fed AC Machines," *Ieee Transactions on Industrial Electronics*, vol. 55, pp. 4181-4190, Dec 2008.
- [80] A. Zamarron and M. A. Arjona, "Detection of stator-winding turn-to-turn faults in induction motors, based on virtual instrumentation," *International Journal of Electrical Engineering Education*, vol. 47, pp. 63-72, Jan 2010.

- [81] J. Arellano-Padilla, M. Sumner, and C. Gerada, "Winding condition monitoring scheme for a permanent magnet machine using high-frequency injection," *Iet Electric Power Applications*, vol. 5, pp. 89-99, Jan 2011.
- [82] J. Arellano-Padilla, M. Sumner, and C. Gerada, "On-Line Detection of Stator Winding Short-Circuit Faults in a PM Machine using HF Signal Injection," *Icem: 2008 International Conference on Electrical Machines, Vols 1- 4*, pp. 1526-1533, 2009.
- [83] F. Briz, M. W. Degner, J. M. Guerrero, and P. Garcia, "Stator Windings Fault Diagnostics of Induction Machines Operated From Inverters and Soft-Starters Using High-Frequency Negative-Sequence Currents," *Ieee Transactions on Industry Applications*, vol. 45, pp. 1637-1646, Sep-Oct 2009.
- [84] A. M. da Silva, R. J. Povinelli, and N. A. O. Demerdash, "Induction machine broken bar and stator short-circuit fault diagnostics based on three-phase stator current envelopes," *Ieee Transactions on Industrial Electronics*, vol. 55, pp. 1310-1318, Mar 2008.
- [85] R. M. Tallam, T. G. Habetler, and R. G. Harley, "Stator winding turn-fault detection for closed-loop induction motor drives," *Conference Record of the 2002 Ieee Industry Applications Conference, Vols 1-4*, pp. 1553-1557, 2002.
- [86] S. L. Ho and K. M. Lau, "Detection of faults in induction motors using artificial neural networks," in *Electrical Machines and Drives, 1995. Seventh International Conference on (Conf. Publ. No. 412)*, 1995, pp. 176-181.
- [87] R. M. Tallam, T. G. Habetler, and R. G. Harley, "Stator winding turn-fault detection for closed-loop induction motor drives," in *Industry Applications Conference, 2002. 37th IAS Annual Meeting. Conference Record of the, 2002*, pp. 1553-1557 vol.3.
- [88] R. M. Tallam, T. G. Habetler, and R. G. Harley, "Continual on-line training of neural networks with applications to electric machine fault diagnostics," *Pesc 2001: 32nd Annual Power Electronics Specialists Conference, Vols 1-4, Conference Proceedings*, pp. 2224-2228, 2001.
- [89] S. T. Wu and T. W. S. Chow, "Induction machine fault detection using SOM-based RBF neural networks," *Ieee Transactions on Industrial Electronics*, vol. 51, pp. 183-194, Feb 2004.

- [90] S. Premrudeepreechacharn, T. Utthiyoung, K. Kruepengkul, and P. Puongkaew, "Induction motor fault detection and diagnosis using supervised and unsupervised neural networks," *IEEE Icit' 02: 2002 IEEE International Conference on Industrial Technology, Vols I and II, Proceedings*, pp. 93-96, 2002.
- [91] J. F. Martins, V. F. Pires, and A. J. Pires, "Unsupervised Neural-Network-Based Algorithm for an On-Line Diagnosis of Three-Phase Induction Motor Stator Fault," *Industrial Electronics, IEEE Transactions on*, vol. 54, pp. 259-264, 2007.
- [92] D. Ho and R. B. Randall, "Optimisation of bearing diagnostic techniques using simulated and actual bearing fault signals," *Mechanical Systems and Signal Processing*, vol. 14, pp. 763-788, Sep 2000.
- [93] N. Kingsbury, "Complex wavelets for shift invariant analysis and filtering of signals," *Applied and Computational Harmonic Analysis*, vol. 10, pp. 234-253, May 2001.
- [94] S. C. K. Li. <http://eeweb.poly.edu/iselesni/WaveletSoftware/allcode.zip>.
- [95] S. G. Mallat, "A theory for multiresolution signal decomposition: the wavelet representation," *Pattern Analysis and Machine Intelligence, IEEE Transactions on*, vol. 11, pp. 674-693, 1989.
- [96] D. L. Donoho, "De-noising by soft-thresholding," *Information Theory, IEEE Transactions on*, vol. 41, pp. 613-627, 1995.
- [97] A. G. C. K. I. F. G. Bebis. (Summer 2002). *Undecimated Wavelet Transform for Image Denoising*.
- [98] D. B. Percival and A. T. Walden, *Wavelet Methods for Time Series Analysis*. New York: Cambridge University Press, 2000.
- [99] D. L. Donoho and I. M. Johnstone, "Ideal Spatial Adaptation by Wavelet Shrinkage," *Biometrika*, vol. 81, pp. 425-455, Sep 1994.
- [100] U. S. E. P. Agency. *Dynamometer Drive Schedules - Testing and Measuring Emissions* Available:
<http://www.epa.gov/nvfel/testing/dynamometer.htm>
- [101] S. Habibi, "The Smooth Variable Structure Filter," 2007.

- [102] R. E. Kalman, "A New Approach to Linear Filtering and Prediction Problems," *Transactions of the ASME – Journal of Basic Engineering*, pp. 35-45, 1960.
- [103] B.-S. Chen and W.-S. Hou, "Deconvolution filter design for fractal signal transmission systems: a multiscale Kalman filter bank approach," *Signal Processing, IEEE Transactions on* pp. 1359 - 1364 May 1997
- [104] A. Tangborn and S. Q. Zhang, "Wavelet transform adapted to an approximate Kalman filter system," *Applied Numerical Mathematics*, vol. 33, pp. 307-316, May 2000.
- [105] T. Zheng, A. A. Girgis, and E. B. Makram, "A hybrid wavelet-Kalman filter method for load forecasting," *Electric Power Systems Research*, vol. 54, pp. 11-17, April 2000.
- [106] K. C. Chou, A. S. Willsky, and R. Nikoukhah, "Multiscale systems, Kalman filters, and Riccati equations," *Automatic Control, IEEE Transactions* vol. 39, pp. 479 - 492 Mar 1994.
- [107] L. Hong, G. Cheng, and C. K. Chui, "A filter-bank-based Kalman filtering technique for wavelet estimation and decomposition of random signals," *Circuits and Systems II: Analog and Digital Signal Processing, IEEE Transactions on*, vol. 45, pp. 237 - 241, Feb 1998.
- [108] R. Cristi and M. Tummala, "Multirate, multiresolution, recursive Kalman filter," *Signal Processing*, vol. 80, pp. 1945–1958, 2000.
- [109] T. Zheng, A. A. Girgis, and E. B. Makram, "A hybrid wavelet-Kalman filter method for load forecasting," *Electric Power Systems Research*, vol. 54, pp. 11-17, April 2000.
- [110] L. Hong, G. Cheng, and C. Chui, "A filter-bank-based Kalman filtering technique for wavelet estimation and decomposition of random signals," *Circuits and Systems II: Analog and Digital Signal Processing, IEEE Transactions on*, vol. 45, pp. 237 - 241, Feb. 1998.
- [111] C.-M. Chou and R.-Y. Wang, "Application of Wavelet-based Multi-model Kalman Filters to Real-time Flood Forecasting," *Hydrol. Process*, vol. 18, pp. 987-1008, 2004.
- [112] C. K. Chui and G. Chen, *Kalman Filtering: With Real-Time Applications*. New York: Springer, 1999.

- [113] B.-S. Chen and W.-S. Hou, "Deconvolution filter design for fractal signal transmission systems: a multiscale Kalman filter bank approach," *IEEE Transactions on Signal Processing*, pp. 1359 - 1364, May 1997.
- [114] K. C. Chou, A. S. Willsky, and R. Nikoukhah, "Multiscale systems, Kalman filters, and Riccati equations," *Automatic Control, IEEE Transactions*, vol. 39, pp. 479 - 492, March 1994.
- [115] A. Tangborn and S. Q. Zhang, "Wavelet transform adapted to an approximate Kalman filter system," *Applied Numerical Mathematics*, vol. 33, pp. 307-316, May 2000.
- [116] G. W. G. Bishop, "An Introduction to the Kalman Filter," 2006.
- [117] S. A. GADSDEN, "SMOOTH VARIABLE STRUCTURE FILTERING: THEORY AND APPLICATIONS," McMaster University, Open Access Dissertations and Theses, 2011.
- [118] M. S. Grewal and A. P. Andrews, *Kalman Filtering: Theory and Practice Using MATLAB*: Wiley, 2011.
- [119] V. Utkin, "Variable structure systems with sliding modes," *Automatic Control, IEEE Transactions on*, vol. 22, pp. 212-222, 1977.
- [120] V. L. Utkin, *Sliding Modes and Their Application in Variable Structure Systems*: Imported Publications, Incorporated, 1978.
- [121] S. A. G. S. R. Habibi, "A New Robust Filtering Strategy for Linear Systems," *Journal of Dynamic Systems, Measurement and Control, Transactions of the ASME*, 2012.
- [122] M. S. Z. Abidin and R. Yusof, "Application of a model-based fault detection and diagnosis using parameter estimation and fuzzy inference to a DC-servomotor," *Proceedings of the 2002 IEEE International Symposium on Intelligent Control*, pp. 783-788, 2002.
- [123] O. Moseler and R. Isermann, "Model-based fault detection for a brushless DC motor using parameter estimation," *Ilecon '98 - Proceedings of the 24th Annual Conference of the IEEE Industrial Electronics Society, Vols 1-4*, pp. 1956-1960, 1998.
- [124] R. Isermann, "Model-based fault-detection and diagnosis - status and applications," *Annual Reviews in Control*, vol. 29, pp. 71-85, 2005.

- [125] D. G. Luenberger, *Introduction to dynamic systems: theory, models, and applications*: Wiley, 1979.
- [126] M. A. AL-SHABI, "The General Toeplitz/Observability Smooth Variable Structure Filter," Degree of Doctor of Philosophy, Department of Mechanical Engineering, McMaster University, 2011.
- [127] C. T. C. Inc., "Mounting Techniques - Section 5 Technical Info."